MECHANICAL PROPERTIES AND DURABILITY
OF NATURAL RUBBER COMPOUNDS AND COMPOSITES

Joseph Thomas South

Dissertation submitted to the Faculty of the
Virginia Polytechnic Institute and State University
in partial fulfillment of the requirements for the degree of

Doctor of Philosophy

in

Materials Engineering Science

Kenneth L. Reifsnider, Chair
Scott W. Case
John J. Lesko
Herve Marand
Brian J. Love

December 14, 2001
Blacksburg, Virginia

Keywords: Natural Rubber, Cord-Rubber Composite, Rubber Reversion, Crosslink

MECHANICAL PROPERTIES AND DURABILITY

OF NATURAL RUBBER COMPOUNDS AND COMPOSITES

Joseph Thomas South

(ABSTRACT)

The focus of this research was to investigate the effect of thermal degradation upon the mechanical properties of natural rubber compounds and apply those effects to the life prediction of off axis 2-ply cord rubber laminates. The work examined both the quasi-static and dynamic mechanical properties of two natural rubber vulcanizates, which had been subjected to isothermal anaerobic aging. Thermal aging was performed on two different natural rubber vulcanizates. The thermal aging was conducted between the temperatures of 80 and 120°C for times ranging from 3 to 24 days. The effect of thermal degradation was measured from the changes in the chemical composition of the vulcanizates as functions of time at temperature. A master curve relationship between the changes in the chemical composition of the vulcanizates due to thermal degradation and their static and dynamic mechanical properties has been developed. This relationship allowed for the prediction of the vulcanizate mechanical properties after thermal aging. It was found that the mechanical properties correlated with the percentage of poly and monosulfidic crosslinks, where in general higher levels of polysulfidic crosslink gave rise to the highest mechanical properties.

Crack propagation in an aged and unaged natural rubber vulcanizate was measured using a double cantilever beam, DCB. This type of testing arrangement exhibits a plane strain condition and resulted in crack growth rates two orders of magnitude faster than traditional plane stress testing geometries. To validate the DCB specimens, an investigation into the potential cavitation inside the rubber of the DCB specimens was performed. It was found that no cavitation occurred due to the high speed of the fracture. DCB samples were thermally aged to determine the effect of thermal aging upon the crack growth rate. It was found that crack growth rates increase with thermal aging.

Life prediction of the aged 2-ply laminates was performed using a finite element analysis. In order to verify the finite element models used in the life prediction, the fatigue failure and crack growth characteristics of off axis 2-ply cord-rubber laminates were examined with a delamination analysis. This analysis allowed for the determination of the modulus of off axis 2-ply laminates in the presence of damage as well as the calculation of the crack growth rates of the laminate. The failure of unaged and thermally aged 2-ply laminates was evaluated and compared to the crack growth rates of thermally aged DCB specimens. The trend due to thermal aging between the two types of testing specimens was consistent.

The finite element analysis was sectioned into two approaches: crack initiation and crack propagation. The former utilized a residual strength approach, while the latter applied a fracture mechanics approach. The predicted stress versus cycles, S-N, curves were not in complete agreement with the experimental data. The error between the predicted and the experimental is discussed and future work to correct that error is suggested. While there was not complete agreement between the predicted and the experimental data, this dissertation outlines a comprehensive approach to track the effects of thermal degradation and apply those effects to a real world application.

THE ROAD NOT TAKEN

Two roads diverged in a yellow wood,
And sorry I could not travel both
And be one traveler, long I stood
And looked down one as far as I could
To where it bent in the undergrowth;

Then took the other, as just as fair,
And having perhaps the better claim,
Because it was grassy and wanted wear;
Though as for that the passing there
Had worn them really about the same,

And both that morning equally lay
In leaves no step had trodden black.
Oh, I kept the first for another day!
Yet knowing how way leads on to way,
I doubted if I should ever come back.

I shall be telling this with a sigh
Somewhere ages and ages hence:
Two roads diverged in a wood, and I-
I took the one less traveled by,
And that has made all the difference.

Robert Frost, *Mountain Interval,* 1916

ACKNOWLEDGMENTS

The author would like to thank the following people who have been instrumental in the progression of this dissertation:

TABLE OF CONTENTS

LIST OF TABLES

LIST OF FIGURES

1. LITERATURE REVIEW

Natural rubber is a heavily researched material. Aspects of natural rubber that have been researched include the: fatigue of rubber, crack growth analysis and fracture, rubber filler interactions, rubber crystallization, aging of rubber, rubber reversion, molecular orientation of rubber and cord rubber composites. The review of the investigations performed by other researchers provides a foundation for this dissertation. This literature review will attempt to cover nearly all aspects of the research that has been conducted on natural rubber as well as other rubbery materials. An emphasis will be placed on the concepts of energy, temperature, crack growth and aging.

1.1   Fatigue of Rubber

Research into the fatigue of rubber has focused on the mechanics of fatigue failure as well as on the development of relations to predict failure [1-11]. The work of Rivlin et al.[1] was the most influential in changing how the fatigue failure of rubber was conceptualized. Rivlin et al.[1] developed a criterion for the tearing of a rubber vulcanizate that was independent of the form of the test piece. This form was based upon the Griffith failure theory that describes the slow propagation of a crack as the conversion of elastic energy stored in the bulk to surface free energy. Griffith postulated that at constant overall deformation, the changes in the elastically stored energy due to an increase in crack length were balanced by the energy used in the creation of new surfaces. However, Rivlin et al.[1] postulated that under the same conditions the changes in the elastically stored energy were balanced by changes in the internal energy. This energy was then the work expended irreversibly per centimeter increase in crack length and per centimeter thickness of the test-piece. This criterion of Rivlin et al. was deemed the tearing energy criteria and it was shown that this characteristic energy could be found experimentally for a particular vulcanizate and used to predict the force required to tear test pieces of that vulcanizate.

Greensmith[2] has validated the tearing energy criterion in the case where a cut or crack is present in a rubber specimen strained in simple extension. The form of the criterion is:

$$T = -\left(\frac{1}{t}\right)\left(\frac{\partial U}{\partial c}\right)_l \qquad\qquad [1.1]$$

where: T is the characteristic tearing energy

t is the thickness of the test specimen

l is the deformed length

c is the crack length

U is the elastically energy density from the imposed deformation

Gent et al. [3] applied the tearing energy criterion to describe the relationship between crack growth and fatigue. Gent et al.[3] found that the fatigue crack growth of natural rubber vulcanizates under repeated loading for different test geometries was consistent when interpreted in terms of the tearing energy. The crack growth per cycle was proportional to the square of the maximum tearing energy attained during that cycle. Using that relation, the fatigue life of a specimen containing a small crack was estimated from elasticity theory as a function of initial crack size and the maximum applied strain. A strain dependence was also established for die stamped specimens that contained no intentionally induced flaws. In order to determine that the tearing energy was not material dependent, Lake et al.[4] extended the use of the tearing energy criterion to non-crystallizing rubbers such as styrene butadiene rubber.

The mechanical fatigue life for natural rubber has been investigated by Lake et al.[5,6]. In their research they found that there exists a critical tearing energy, T_o, for which mechanico-oxidative crack growth can occur. For energies below this threshold, crack growth is attributed solely to chemical attack by ozone. At energies above T_o, the crack growth per cycle rapidly increases and attains a value of a few angstroms per cycle. This crack growth rate puts the crack growth achieved per cycle on the same scale as the molecular chains. In a fatigue test, T_o is a critical strain value below which the number of cycles to failure increases rapidly. This critical strain constitutes a mechanical fatigue limit for rubber.

19

Testing conditions such as strain rate, testing temperature, applied strain level and oxidation effects have been studied in conjunction with fatigue crack propagation [7,8]. Young[8] demonstrated that as tearing energies increase there can be a sharp transition from moderate steady-state crack growth rates to a catastrophic crack growth region. This is analogous to the three regions of fatigue crack growth, but the change in the tearing energy, ΔT, is used rather than the change in the strain energy release rate, ΔG. Increasing temperatures generally increases the slope of the fatigue crack growth but this increase in the slope can vary greatly between different elastomers e.g. natural rubber (NR), styrene butadiene rubber (SBR) and butadiene rubber (BR). Both NR and BR showed little strain rate dependency in the range of 1 to 20 $\sec^{-1}$. Oxidation and ozonation greatly affected the fatigue crack propagation, where an addition of 0.5 parts per million ozone to an air atmosphere increased the crack propagation rate by 40 to 80% compared to specimens in an air atmosphere.

Recently Bathias et al.[9] presented work on the fatigue initiation and propagation in natural and synthetic rubbers with respect to the following: the chemical microstructure of the rubber, loading, environment, thickness and complex loadings. Bathias et al. established that fatigue damage depends on three basic factors: chemical composition, environment and mechanical stresses. In their experiments axisymetric hour-glass specimens were loaded in tension and compression. Fatigue behavior was improved for tests with a mean stress in tension, $R \geq 0$, while a minimum stress in compression, $R < 0$, greatly increased the fatigue damage. In their research, Bathias et al. demonstrated that damage due to chemical effects is greater at higher temperatures due to the acceleration of the oxidation reaction. In addition, Bathias et al. showed that the fatigue crack growth of rubbers can be modeled by the application of fracture mechanics. They found that cavitation occurred in the interior of the specimen due to high hydrostatic pressures. This cavitation mechanism occurred under static tension, cyclic tension and static tension torsion loading.

Shen et al.[10] have investigated the compressive cyclic stress-strain behavior of structural foams. The polyurethane foam they investigated is similar to natural rubber as they both demonstrate the Mullins effect. This Mullins effect is the cyclic strain softening of the rubber due to the fracturing of the shortest

polymeric chains in the network upon loading. Shen et al. demonstrated that upon an applied cyclic load to a constant strain level the cyclic softening achieves a steady state value after approximately 100 cycles. Utilizing this information and the modified Ogden's model, Shen et al.[10] were able to express the cyclic stress-strain behavior at any cyclic level.

Innovative approaches to investigate the crack growth of rubbers have been developed[11]. For example, Lefebvre et al.[11] utilized a double cantilever beam specimen to measure the fracture energy of a rubber to metal bond. The tests were performed in seawater and NaOH solution with a cathodic potential applied. While the initial application of this geometry was to measure the adhesion between the rubber and the metal, a modified version of this geometry will be applied to measure the crack growth rate of the rubber. This will be discussed in detail in chapter 6.

The research into the fatigue of elastomers has shown that the fatigue crack growth of rubbers can be modeled by applying fracture mechanics. The technique of the tearing energy has been widely applied and accepted to describe rubber fatigue crack growth. A critical tearing energy has been found to exist below which all crack growth is attributed to oxidation. For energies above this critical tearing energy, crack growth increases eventually obtaining a rate on the scale of one polymer monomer unit per cycle. The fatigue life initiation and propagation in natural and synthetic rubbers are dependent upon the chemical composition, environment and the mechanical stresses applied to the sample.

1.2   Crack Growth Analysis and Fracture

Application of the tearing energy criterion to the crack growth and fracture of NR has been performed[12-22]. Lake et al.[12] have further shown that the rate of crack growth is independent of sample shape and type of deformation when expressed in terms of the elastic energy. Their work was aimed at determining the mechanism of groove cracking in tire treads. Lake et al.[12] applied a method which enabled the elastic energy to be estimated for a tire groove from measurements of the crack opening area upon an applied stress. The method also enabled Lake et al.[12] to determine the strain within the sample. Lindley[14] investigated three methods of determining the tearing energy: from changes in total energy, from crack surface displacements and by comparison with known values for the same crack

growth rates. It was found that all three methods, when applied to plane stress specimens, were satisfactory in determining the energy for crack growth in model rubber components. Particularly, the crack-surface-displacement method, similar to Lake et al.[12], was found to be the most satisfactory.

The crack velocities in natural rubber have been measured by Gent et al[15]. They investigated biaxially stretched sheets of unfilled and carbon black filled natural rubber. The crack velocity was found to increase with the cleavage strain, ε_y, and with the strain, ε_x, parallel to the direction of tearing. Velocities over 100 m sec^{-1} were obtained, one-third the speed of sound. It was found that below a critical value of cleavage strain, ε_y, no crack growth occurred. This limiting behavior is analogous to the critical tearing energy, T_o, of Lake et al[5]. Gent et al.[15] did see a difference in the behavior between the filled and unfilled materials. For the carbon black filled material, cracks grew at a low velocity for a range of strains above the critical strain, and then the velocity rapidly increased. However, for the unfilled material the cracks grew rapidly once the threshold strain was surpassed. The velocities of the high-speed cracks were found to be independent of the available elastic energy for fracture and dependent upon the state of biaxial strain. Thus filler has an effect upon the crack propagation rate in NR; however, these rates are not solely a function of the elastic energy but also the applied deformations.

Rivlin et al.[16] examined the effect of stress relaxation on the resistance of an elastomer to tearing. In their investigation, Rivlin et al.[16] utilized a two-network model for an elastomers in which stress relaxation has already occurred. Rivlin et al.[16] viewed the configuration of an elastomer when deformed as being in two different states. These two states occur because, under a large applied stress, rupture and recombination of crosslinks can take place. Such a large applied stress can be in the region near a crack tip. Thus after relaxation, both of these configurational states are in an unstressed state. One configurational state is based upon the original configuration of the elastomers, while the second state is based upon the applied state of deformation. When the deforming forces are removed the elastomeric network will adopt a configurational state that is different from the initial state and is between the unstressed state of the two component networks.

The approach of Rivlin et al.[16] included the effect of this relaxation on the elastomer, in the context of the tearing energy, applied to the assumption of the kinetic theory of rubber elasticity[23]. The characteristic tearing energy was calculated using the methodology of Lake et al.[12], as the energy required to break a chain segment. Lake et al.[12] assumed an isotropic elastomer in which a chain segment must be fully extended in order to break. While only one chemical bond needed to break to cause failure, all of the chemical bonds must be stretched to nearly the breaking point. Rivlin et al.[16] found that whether or not the chain segments were assumed to be Gaussian or non-Gaussian, a substantial degree of anisotropy in the characteristic tearing energy is predicted depending upon the ratio of the two component networks. The tearing energy was found to be greater parallel to the direction of extension rather than perpendicular when the number of links per chain segment were approximately equal in the two networks. However, if the number of links per chain segment was greater in the network based upon the applied state of deformation the tearing energy was less in the direction parallel to the extension. Both of these effects were greater for the non-Gaussian model.

The concept of the tearing energy has been expanded using the J-integral[17,18,19]. Both the J-integral and the tearing energy methods characterize the fracture properties by assuming that a critical amount of energy is required to advance a crack by unit area. Lee et al.[17] found that the J-integral approach exhibited less scatter than the tearing energy but required a larger crack length versus specimen length ratio to obtain accurate values. Furthermore, the J-integral technique separated the critical energy in the region of the crack tip and the stored elastic energy in the bulk. Lee et al.[17] recommended that the critical crack tip energy release rate for initiation and fracture be considered material properties, which represent the materials resistance to fracture as well as being an appropriate parameter for material evaluation.

Rather than using the single edge crack specimens, which are limited in the range of attainable energies, new approaches to measuring the crack growth in natural rubber are being developed[20,21,22]. Sumner[20] has performed research using a tear analyzer. This machine automatically measures the crack propagation rate in rubber and the mechanical parameters during dynamic testing. Crack analysis of an

unfilled natural rubber using infrared microspectroscopy has been investigated by Neumeister[21]. This technique demonstrated that in a stressed crack the material surrounding the crack tip possesses different characteristics than the bulk. In a razor cut test the crack tip region of an unstressed material was spectroscopically identical to the material in the bulk. Neumeister concluded that application of stress is the cause of the differences between the crack tip and the bulk both in forcing the material to relocate and in stress induced orientation effects.

Gent et al.[22] have investigated the energy release rates obtained from a crack in a tilted block. They found that a thin long block is likely to undergo an internal cavitation prior to achieving sufficient fracture energy to propagate a crack inwards. This cavitation is a result of the hydrostatic tension generated inside the rubber due to the applied load. Gent et al.[22] found that long narrow blocks are more suitable for crack growth measurements because higher values of energy release rate can be achieved without causing cavitation. The motivated for this research was the crack propagation specimen examined in this dissertation, the double cantilever beam. A more detailed discussion of the double cantilever beam will be presented in chapter 6.

The tearing energy can be applied to explain the crack growth and fracture of NR. The energy concept has been enhanced by the use of the J-integral to characterize the fracture properties. An energy approach appears to be the most appropriate method to characterize the failure of NR compounds. However, the energy necessary for fracture will depend on the characteristics of the bulk material as well as local stress concentrations.

1.3   Rubber Filler Interaction

The interaction between the rubber and the filler has been studied to determine the effects on failure of the compounds[24-27]. Neogi et al.[24] have researched the high temperature interaction between rubber and filler by using the strain amplification factor. When carbon black is added as reinforcement, the degrees of freedom of the rubber chains are decreased due to the interaction and adsorption of non-deformable carbon black onto the rubber. Upon an applied load the rubber must bear the total strain; however, the local strain within the rubber phase is greater than the global strain attained by the system.

This difference between the local and the global strains is termed the strain amplification factor. Neogi et al.[24] determined the strain amplification factor at different strain rates and temperatures with N-220, N-375, N-550, N-660 carbon blacks and china clay as filler at 50 parts per hundred parts polymer. For all samples, Neogi et al.[24] found that the strain amplification factor achieved a limiting value at 100°C. This value was greater for fillers possessing a higher surface area, thus producing a greater interaction with the rubber.

Chung et al.[25] investigated the effects of carbon black on the ultimate properties of an elastomer. They examined both the critical tearing energy as well as a critical J-integral. They found that for NR compounds, crystallization could be observed near the crack tip. Crystallization hindered the crack propagation through the thickness of the specimen. The level of carbon black loading moderately affected the T_o of the NR compounds, with the value ranging from 4.1 kN m^{-1} to 6.9 kN m^{-1}. The true modulus of the compound was found to increase with increasing levels of carbon black.

Wang[26] has performed a detailed examination of the effects between rubber-filler and filler-filler on the dynamic properties of vulcanizates. Similar to Chung et al.[25], Wang found that the modulus of the compound increased with an increasing level of carbon black. The increase was consistent for both the loss modulus as well as the storage modulus. Wang[26] ascribed the stiffening due to the filler by the adsorption of polymer molecular chains on the filler surface. This adsorption reduces the mobility of the polymer segments and results in a rubber shell on the filler surface. The reduced mobility and the rubber shell increases the polymer viscosity. This increase in viscosity created a broadening of the spectrum of relaxation times, τ_i, and the modulus accordingly increases.

Lake and Lindley[27] investigated the effect of carbon black on the fatigue life of rubbers. Lake et al.[27] found that the addition of carbon black serves as a source for hystersis in the compound. This added carbon black considerably reduced the temperature dependence of fatigue life of SBR but did not influence the fatigue life of natural rubber. This difference was attributed to the sources of the hystersis within the two rubbers. For natural rubber hystersis occurs mainly from crystallization at high

strain and is relatively unaffected by changes in temperature or frequency, while the hystersis of SBR is due to internal viscosity which is continually varying.

The interaction between the rubber and the filler affects the quasi-static properties of the compounds as well as the fatigue life. Inclusion of carbon black into NR compounds serves to increase the modulus of the compound as well as hinder crack propagation. This reduction in the crack propagation occurs because of localized crystallization occurring in the compound due to regions of highly constrained polymer. These regions occur near the crack tip as well as in regions of high constraint due to the filler particles.

1.4   Rubber Crystallization

Rubber crystallization occurs due to a decrease in the localized entropy upon an imposed deformation[28-31]. This phenomena is explained by the Gibbs Free Energy. The thermodynamic formula the Gibbs Free Energy is shown as equation 1.2:

$$\Delta G = \Delta H - T\Delta S \qquad\qquad [1.2]$$

where ΔG is the change in the Gibbs Free Energy, ΔH is the change in the enthalpy, T is the absolute temperature and ΔS is the change in the entropy of the system. At equilibrium, in the liquid state, where $T > T_g$, the change in the free energy is zero and the change in the enthalpy is equal to the enthalpy of fusion, ΔH_f. In equation 1.2, T becomes the local melting temperature of the system, T_m. The entropy is given by the equation of Boltzmann as:

$$S = k \ln \Omega \qquad\qquad [1.3]$$

where k is Boltzmann's constant and Ω is the number of configurational states of the polymer. Under an imposed deformation the number of configurational states approaches one. This configuration change occurs for the polymeric chains aligning themselves in the direction of the applied load. Thus, ΔS approaches zero. In order to maintain continuity of equation 1.2, the local melting temperature must increase. Once T_m increases below the ambient testing temperature crystallization will occur.

Allegra[30,31] has found that the crystallization of rubber can be modeled as a third order transition. This is different than the second order theory of Flory[32]. Goritz et al.[29] discuss an additional

process of strain-induced crystallization. If a maximum in the degree of crystallinity in not reached under the applied load, then the remainder of the crystallizable chains crystallize on reducing the temperature. Goritz et al.[29] investigated both of the two strain-induced crystallization phenomena by performing differential scanning calorimetry scans on deformed specimens. For a cis-1,4 polybutadiene specimen extended to 400 % strain the two crystalline melting regions appeared separately. The full width half maximum, FWHM, of the temperature induced crystalline region was 267 K while the FWHM of the strain induced crystalline region was 310 K. The FWHM of the temperature induced crystallization between the strained sample and an unstrained sample differed by 5 K. Goritz et al.[29] explained this difference as an stress induced entropic effect.

Crystallization in NR is a stress induced an entropic effect. The reduction in the entropy can occur in the regions of high stress concentrations such as the tip of a crack. The interaction between rubber and filler can affect the mechanical properties of NR, but what effects are there to the compound as a function of time.

1.5 Aging of Rubber

The effects of aging on rubber have been studied to determine the time dependent effects on NR compounds[5,6,27,33-35]. The bulk of the research into the aging of rubber has concentrated on the oxidative effects. Thermal effects on the properties of natural rubber will be discussed in the context of rubber reversion. Oxidative effects occur when oxygen attacks the unsaturated bond along the backbone of the polyisoprene, natural rubber, chain. Braden and Gent[33,34] have defined the characteristics of static crack growth due to ozone. The research of Braden and Gent[33,34] concluded that a critical tearing energy is necessary for cracks to grow, crack length increases linearly with time for $T > T_o$ and the rate of crack growth is similar and proportional to the ozone concentration.

The research of Lake and Lindley[27,35] has expanded upon the work of Braden and Gent[33,34] to examine the role of ozone in the cracking and fatigue of rubber. As stated previously, Lake et al.[5,6], demonstrated that there is a threshold value for tearing energy below which all crack growth is attributable to ozone. In conjunction with the oxidation of rubber, there is an appreciable R-ratio effect

on fatigue crack growth. Lake and Lindley[27,35] demonstrated that the rate of crack growth is 10^4 times slower for dynamic testing with an R-ratio >0 compared to a test with an R-ratio = 0 at the same maximum tearing energy. This growth rate was very similar to the rate observed in relaxing tests below T_o, suggesting that ozone was the cause of the crack growth. Thus by not allowing the minimum tearing energy to fall below zero, the mechano-oxidative crack growth may be suppressed. This mechano-oxidative suppression led to a large increase in fatigue life. It was also shown that the crack growth rate was proportional to the concentration of ambient ozone; however, the inclusion of antiozonants could increase the critical energy required for crack propagation and decrease the rate of crack growth[36].

Oxidation attacks the backbone of the polymer. For energies below the critical tearing energy, all crack growth has been attributed to oxidation. A strong R-ratio effect appears to exist in NR compounds. For R > 0 the crack growth rate is of the same order of magnitude as that attributed solely to oxidation. The presence of oxygen affects the properties of NR, by attacking the backbone of the polymer chains; however, elevated temperature affect the crosslinks between chains.

1.6   Rubber Reversion

Rubber reversion is a thermally driven process by which the vulcanized rubber reverts back to the gum state. Research has demonstrated that this process involves three types of crosslinks in the vulcanizate: polysulfidic, disulfidic and monosulfidic[37-46]. In vulcanizates the bond energy between the sulfur crosslink atoms and the polymer backbone greatly differ. The thermal decomposition temperature of natural rubber is $70^o C$; however, the thermal decomposition of polysulfidic bonds may occur at a lower temperature[37]. Lyubchanskaya et al.[37] demonstrated that the thermal decomposition of polysulfidic bonds proceeds at one order of magnitude faster than the oxidation of the polymer chain for a vulcanizate not containing antiozonants. Blackman et al.[39] expanded the relationship between the natural rubber structure and thermal aging to include physical properties. They suggested that crosslink degradation processes might contribute to the deterioration in physical properties of the vulcanizate. The research of Blackman et al.[39] concluded that fatigue life was not necessarily a function of the crosslink type distribution.

The research of Nasir et al.[40] investigated the effects of the various crosslinks on the physical properties of NR. They found that for NR, polysulfidic crosslinks gave rise to improved mechanical properties, with the exception for tear strength, than either mono or disulfidic crosslinks. In their experiments they produced samples that were known to contain increased levels of polysulfidic crosslinks. To correlate the properties with the chemistry, Nasir et al. measured the total crosslink density rather than the exact levels of polysulfidic crosslinks. The ultimate stress was found to increase with inverse crosslink density until it leveled off. Further increases in M_c^{-1} resulted in a lowering of the ultimate stress. The initial increase was due to an increase in the number of chains in the network; however, once a maximum value was achieved the chains were shortened with an increase in M_c^{-1}. Other mechanical properties showing this inverse dependence were modulus, ultimate strain and hystersis.

Sloan[42] has investigated the effect of carbon black on reversion, and found that reversion was not a linear function of carbon black loading. The research of Bristow[41] presented evidence that the grade of natural rubber affects the reversion behavior of the vulcanizate. The rate of reversion varied by a factor of 1.8 for all grades of carbon black. Predictive models for reversion in order to prevent overcuring of tires have been generated by Rimondi et al.[44]. The spinup wear of aircraft tires has been investigated by Padovan et al.[43]. According to Padovan et al.[43], upon landing the friction generated by the tire and the runway can raise the temperature of a thin boundary layer of the tire to begin reversion. Once the local temperature of the reverting rubber is sufficient to lower the local tear strength compared to the shear stresses in the layer, deposition of the reverted rubber occurs. This leads to a layer of rubber being lost during landing.

Elevated temperature is a driving factor for the degradation of NR by causing the reversion of the crosslinked sulfur network back to the gum state. This process involves the crosslinks generated during the vulcanization process and can proceed at temperatures lower than the thermal degradation temperature of NR. For a vulcanizate that does not contain antiozonants, reversion of polysulfidic crosslinks proceeds at one order of magnitude faster than oxidation. Thus for a vulcanizate containing

29

antiozonants rubber reversion would appear to be the dominant non-mechanical degradation mechanism.

1.7   Rubber Molecular Orientation

The molecular orientation of rubber is typically investigated in terms of an applied load and the resulting strain induced crystallization[47-57]. Techniques such as wide angle x-ray scattering[46,49,54], deuterium magnetic resonance[47], fourier transform infrared spectroscopy[52] and stationary fluorescence polarization[55] have been applied to determine the orientation parameters of the network. However, when studying polymers one must always keep in mind the history of the specimen prior to testing. While the theory of rubber elasticity is based upon an irregular, three-dimensional network, it does not take into account any history effects. At room temperature there is no physical aging of a NR vulcanizate, because $T_g \approx -75^oC$, but there is a mechanical history to the specimen.

During vulcanization, a rubber compound changes from a relatively weak viscoelastic liquid to a relatively strong viscoelastic solid. In order for a sheet of vulcanized rubber to be formed it is typically milled down to the desired testing thickness. After milling the sheet is place in a hot press where it is cured at elevated temperature and high pressure[58]. Thus prior to the final vulcanized shape the sample has obtained a milling history that can orient the liquid polymer chains in a preferred direction. This orientation may affect the laboratory test results. Greater detail, as well as experimental evidence of a potential orientational effect in a vulcanizate, will be discussed in chapter 6.

1.8   Cord Rubber Composites

Thus far this review has focused on the research into the compounds and their properties. Particularly, the focus has been on the measurement of those properties and the reduction of those properties. However, real world applications such as tires are composite structures comprised of either steel or polymeric cords and the compounds. In order to validate the analytical approaches for tires and other more complex systems, cord rubber composite laminates are tested. The cord-rubber

composite is a common laboratory specimen because it resembles the structural belts of a tire as well as conveyer belts and other systems[58].

Cord-rubber composites have been investigated in order to determine their crack initiation and propagation mechanisms[59-67]. Using a model cord-rubber composite with exposed cords, Breidenbach et al.[59] examined the mechanics of propagation of interply cracks. Breidenbach et al.[59] assumed that the initiation process during which an interply crack was formed was relatively short and excluded the process from their study. In their work they classified the specimens into three deformation regions: a central region where deformations are relatively uniform and approximately obey a pantographing model, and two regions along the free edge where deformations vary in a complex manner. In these edge regions shear strains up to 1000% can occur from an overall extension of up to 5%. These high shear strains create stress concentrations at the edge and lead to the initiation of penny shaped cracks at the cord ends. These penny shaped cracks coalescence to form a line crack parallel to the direction of loading which in turn develops into an interply crack. The interply crack propagates with the crack growth characteristics of the material until delamination is extensive enough to exceed the load bearing capability of the laminate to the point of failure.

The initiation of penny shaped cracks has been investigated by Gent et al.[60] and Huang et al[62]. Gent et al.[60] assumed that the energy necessary to create a penny shaped crack needed to be greater than the sum of the energy required to fracture the cord-rubber interface and any increase in the strain energy of the rubber itself. Deformation in the cord was assumed to be negligible. Huang et al.[62], knowing that the two plies in a cord-rubber composite are rarely identical, demonstrated that cracks typically developed from the narrower ply. Huang et al.[62] also showed that the fatigue life of the composite was a linearly decreasing function with increasing dynamic amplitude, load and maximum interlaminar shear strain. Additional research into cord-rubber composites has focused on finite element modeling of the structure to determine areas of high stress concentration and to model the three-dimensional dynamic response of the composite[63-67].

1.9   Statement of Work

The focus of this research was to investigate the effect of thermal degradation upon the mechanical properties of natural rubber. The work was divided into two aspects of the mechanical properties: static and dynamic. This investigation focused on two different natural rubber compounds. The two compounds were natural rubber with 65 pphr carbon black. The exact composition of the compounds is proprietary.

The static behavior was based upon the correlation of chemical variables with static properties, such as ultimate stress, ultimate strain, modulus and shear strength. The chemical variables used were the percentages of polysulfidic and monosulfidic crosslinks as well as the total crosslink density. A master curve relationship between the chemical variables and the mechanical properties was developed to predict real world time scales from laboratory data.

The dynamic behavior was based upon the determination of the fatigue behavior and the crack propagation rates. The fatigue tests were performed on die cut sheet stock. The effect of the R-ratio upon the fatigue life was investigated. Crack propagation experiments were based upon the use of a double cantilever beam specimen. Both fatigue and quasi-static crack growth were examined. Crack growth and crack growth rates were examined in thermally aged as well as unaged specimens. An investigation into the possible cavitation of the rubber at the crack tip within the DCB specimen was performed. The effect of the rubber orientation upon the crack growth rates was examined.

A delamination damage analysis of the fatigue of a 2-ply cord-rubber laminate was performed in order to verify finite element models. The growth of the delamination area was tracked in accordance with the reduction of the composite modulus as a function of cycles. The failure of unaged and thermally aged 2-ply laminates was evaluated and compared to the crack growth of the thermally aged DCB specimens.

Predictions of the fatigue lifetime of unaged and thermally aged 2-ply laminates using the generated master curves and mechanical property data. The predictions were discretized into crack initiation and crack propagation. The crack propagation section utilized a residual strength approach; the crack propagation employed a fracture mechanics approach.

32

2.   ANALYSIS OF COMPOUNDS

As stated in the statement of work, this research will utilize two NR compounds. These two compounds are typical of those used in truck tires. For clarification these two compounds were deemed compound A and compound B. Due to the proprietary nature of the tire and rubber industry, only a limited amount of compound information accompanied the compounds. The information provided on the compounds was that both were 100% NR with a carbon black level of 65 pphr. In order to reduce the effects of oxidation, an antiozonant was added. Figure 2-1 shows the typical cross-section of a radial tire. The belt package, radial plies and tread are shown in the figure.
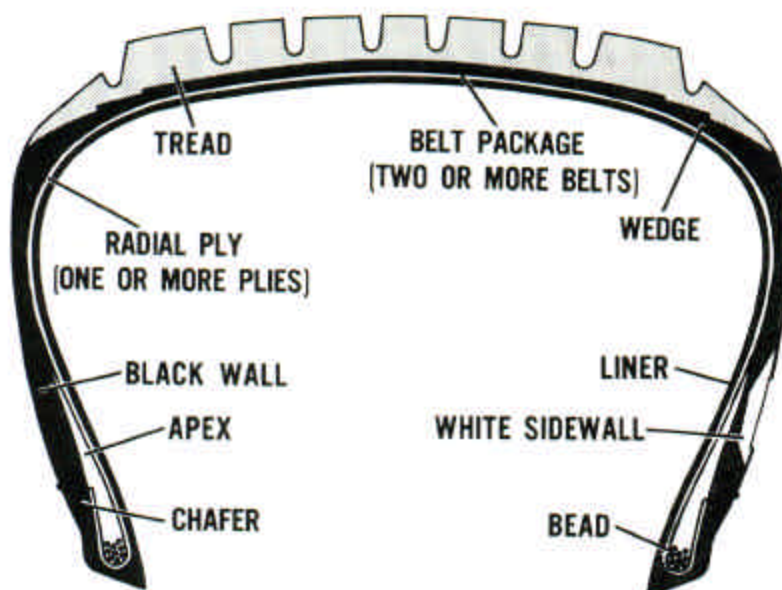
Figure 2-1   Cross-section of a radial tire showing the generalized structural design.[68]

Due to the limited amount of information provided on the two compounds it was necessary to perform material characterization experiments in order to determine the differences between compound

A and compound B. The testing performed was: dynamic mechanical analysis, thermogravimetric analysis, differential scanning calorimetry and transmission electron microscopy. Applications of these techniques allowed for the determination of the glass transition temperature, T_g, storage modulus, E', loss modulus, E'', constant pressure specific heat capacity, C_v, melting temperature, T_m, as well as quantification of the carbon black particle dispersion. The time dependent material differences between these two compounds were examined via creep rupture testing at both room temperature and elevated temperature.

2.1   Dynamic Mechanical Analysis

Dynamic mechanical analysis was performed using a Perkin-Elmer DMA7. Samples were cut from 2mm sheets of compound into rectangular specimens with dimensions of 14.5 x 3.9 x 2.0 mm. The samples were tested using a three-point bend fixture. Prior to the test, the samples and test fixture were cooled to -100^oC using liquid nitrogen. Once the test began the temperature was increased at the rate of 10^oC min^{-1} while the samples were sinusoidally loaded at 1 Hz under displacement control. During the test the storage modulus, loss modulus and tan δ were recorded as functions of the experimental temperature. The results of the DMA testing for both the compound A and compound B are shown in Figure 2-2 and Figure 2-3.
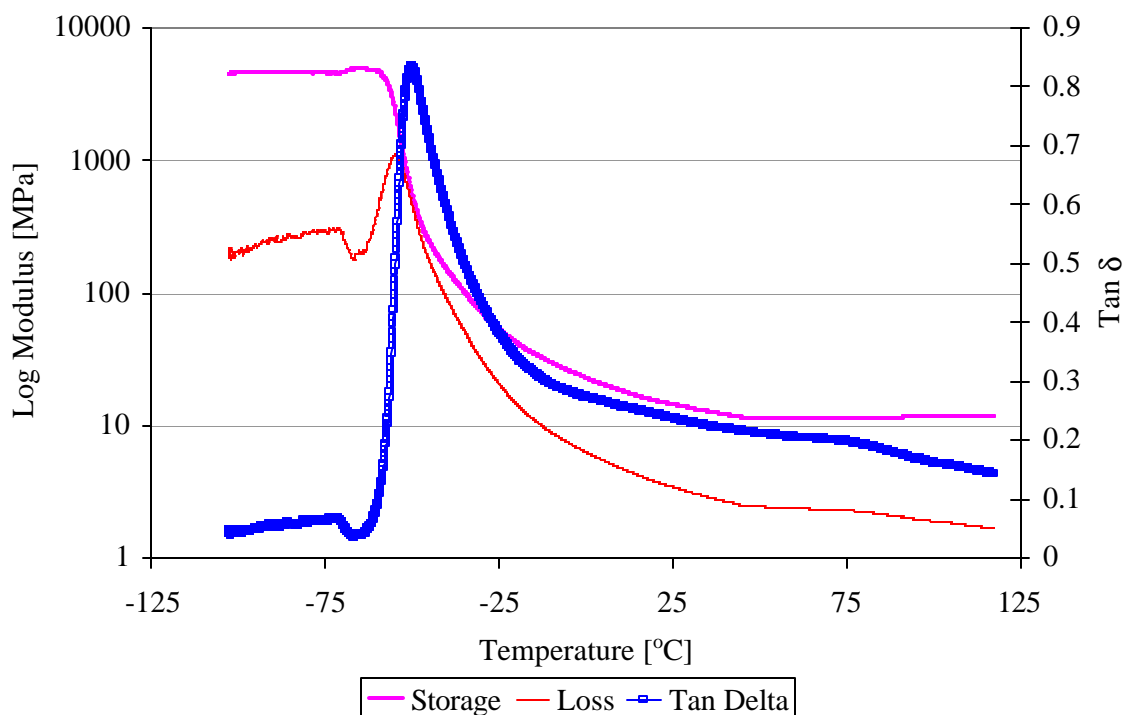
Figure 2-2   Dynamic mechanical analysis results of compound B.

From examination of Figure 2-2 and Figure 2-3 the storage and loss moduli as a function of temperature was evaluated. From the maximum of the tan δ in the figures the glass transition temperature, T_g, of compound B was -49°C and that of the compound A was -51°C. These values were significantly higher than the unvulcanized natural rubber glass transition temperature of -75°C[69]. The glass transition was expected to increase somewhat due to vulcanization; however, this temperature increase is typically less than 10 degrees Celsius. The T_g of the compounds will be investigated further using differential scanning calorimetry.

The room temperature storage modulus of compound B was 14 MPa, while the storage modulus of the compound A was 32 MPa. Given the information that accompanied these two compounds it was expected that both compounds would possess similar mechanical behavior. The differences between the two compounds may be explained by the differences in the type of carbon black that was used as the filler.
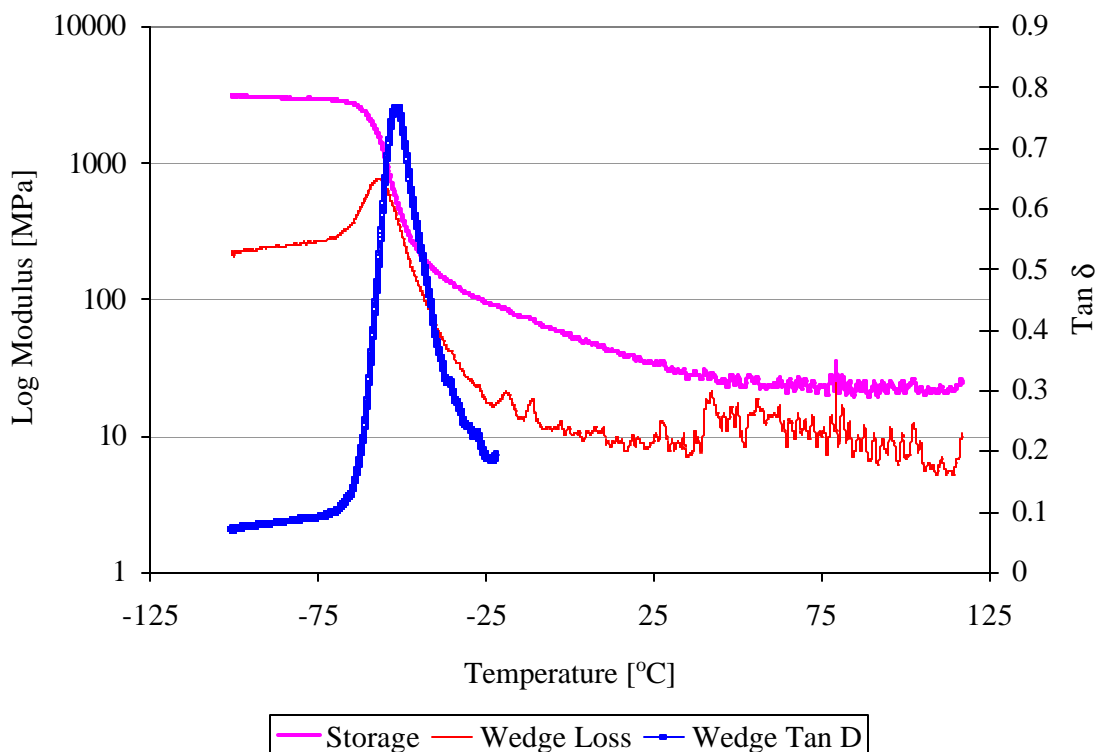
Figure 2-3   Dynamic mechanical analysis results of the compound A.

2.2   Differential Scanning Calorimetry

In order to obtain a clearer understanding of the glass transition temperature as well as to investigate the types of carbon black within the compounds differential scanning calorimetry was performed. The testing was performed using a Perkin Elmer Pyris 1 DSC. Samples of compound A and compound B with mass between 6.4 and 8.3 mg were extracted from the vulcanized sheets and placed into samples pans. The pans were then hermetically sealed and placed into the DSC. Prior to the beginning of the test, the pans were cooled to -150°C using liquid nitrogen. During the test, the temperature of the pans was increased at 10°C min^{-1} from -150°C to 125°C. Each temperature scan in the DSC was run twice in order to determine if any additional curing occurring during the course of the scan. It was found that no additional curing of the compounds occurred due to the temperature scans in

the DSC. The results from the scans are presented in Figure 2-4. The heat flow for each compound is normalized by the maximum heat flow in W g^{-1} that was attained during the scan of each compound.
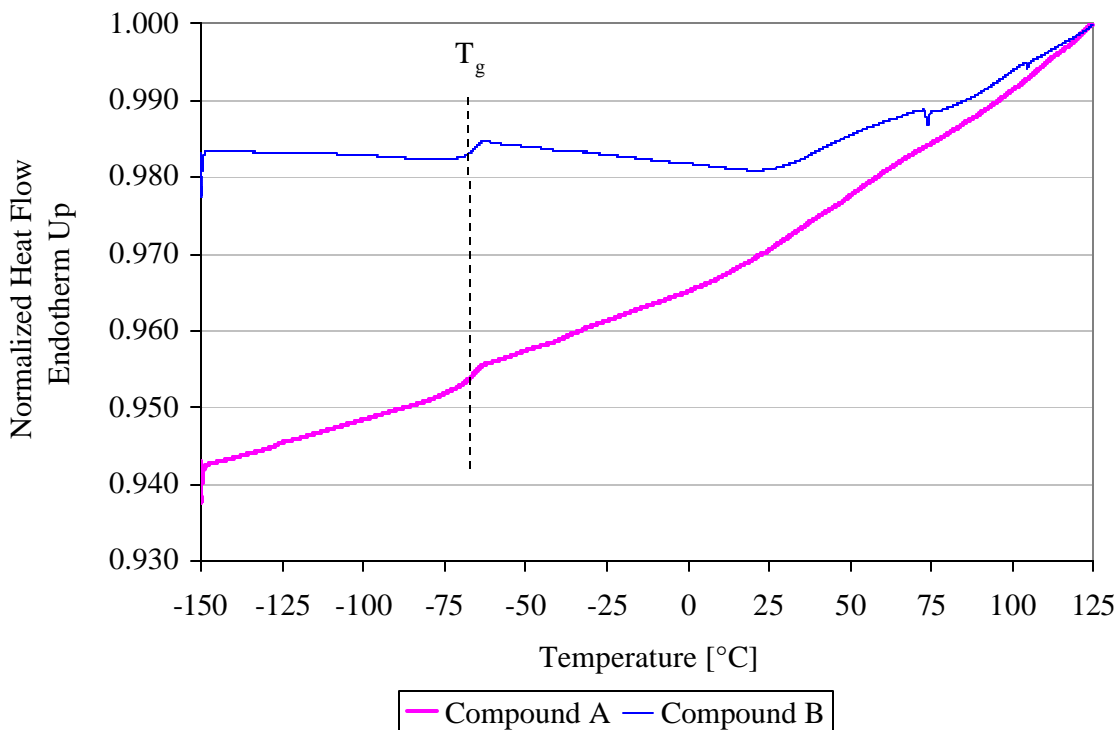
Figure 2-4   Differential scanning calorimetry traces of compound A and compound B.

The DSC scans showed the glass transition temperature for both compounds to be –65$^{\text{o}}$C. This temperature value is in better agreement with what was expected due to vulcanization. The higher value of the glass transition temperature given from DMA was possibly an artifact of the test frequency. Analysis of Figure 2-4 shows a potential difference in the specific heat at constant pressure, C_p, between the two compounds. The difference in the C_p may possibly be attributed to the different types of carbon black filler in the two compounds. Typical carbon blacks found in the compound A and compound B are shown in Table 2-1.

Table 2-1   Typical carbon black types and the range of particle sizes for compound A and compound B.[69]

Compound	Carbon Black Type	Range of Particle Sizes
Compound A	N-660	49 –60 nm
Compound B	N-330	26 – 30 nm

The difference in the heat flow between the two compounds may also be be due to drift of the baseline between each successive DSC trace. Unfortunately, an exact comparison of the DSC data of the two different compounds cannot be made since a sapphire baseline was not performed. Application of a sapphire baseline would have allowed for an exact comparison of the DSC traces of the two compounds by providing a standard from which to compare to.

2.3   Thermogravimetric Analysis

The DMA and DSC provided data on how the compounds may behave under typical operating conditions; however, the ablation temperature of the compounds is unknown. The thermal limits of the compound are required so as to prevent a thermal aging condition being chosen which results in the ablation of the compounds rather than the thermal reversion. In order to determine the ablation temperature of the compounds thermogravimetric analysis was performed.   The tests were performed using a DuPont Instruments 951 Thermogravimetric Analyzer. Samples were extracted from the sheeted compound into cubes with a mass ranging from 14 to 21 mg. The tests were run in a nitrogen atmosphere from room temperature to $500^{o}C$ with a heating rate of $10^{o}C\,min^{-1}$.

The results of the TGA are shown in Figure 2-5. The figure shows the percentage mass retention as a function of temperature for both compound A and compound B as well as two polybutadiene compounds with 30 and 60 pphr carbon black levels.   The two polybutadiene compounds were obtained from a separate study conducted prior to this research. In the figure the thermal decomposition for compound A and compound B began near $200^{o}C$ and was complete at $400^{o}C$. Both compounds had similar temperature dependencies and yielded identical mass retentions after thermal decomposition.   Given that the temperature corresponding to the onset of thermal decomposition was significantly lower than that achieved in either the DMA or DSC testing it was

38

assumed that no thermal decomposition of the material occurred during those tests. In Figure 2-5 the mass retention after thermal decomposition of the four compounds can be compared. As expected, the 65 pphr filler level of compound A and compound B yielded the highest mass retention of the four compounds. It is interesting to note the plateaus between the four different compounds and the relative mass retention between the 30, 60 and 65 pphr filler levels.
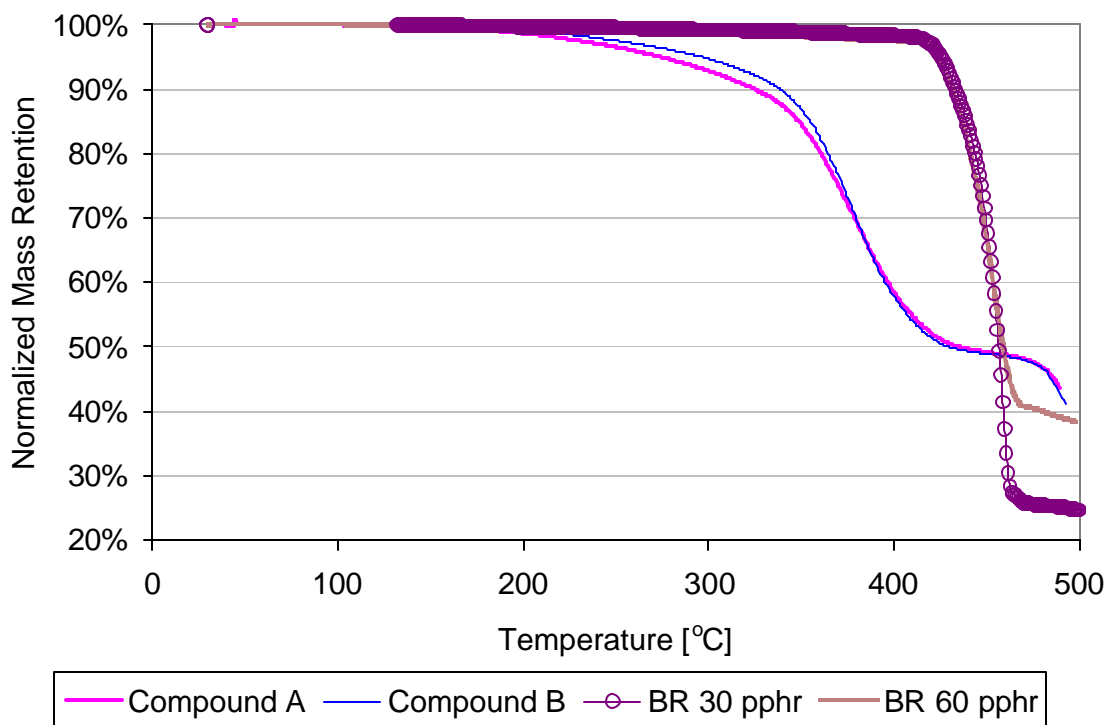
Figure 2-5   TGA temperature sweeps of both compound A and compound B as well as two polybutadiene compounds with 30 and 60 pphr levels of carbon black.

2.4   Transmission Electron Microscopy

The use of DMA, DSC and TGA provided basic material temperature dependence of the two compounds as well as providing an inkling of the probable differences in the type of fillers used in the two. This difference is potentially attributed to the type of filler that was used in the compounds. In

order to investigate this assumption, both compounds have been examined via transmission electron microscopy.

Samples for the TEM were prepared by microtoming in liquid nitrogen using a Reichert-Jung Ultracut-E Ultra Microtome with the FC 4D cryogenic attachment. The thickness of the samples was approximately 70 nm. After microtoming the samples were placed on a TEM sample grid and examined in a Philips 420T TEM in bright field under 100 kV. Figure 2-6 and Figure 2-7 are representative TEM images of compound B and compound A respectively. Both figures show individual carbon black particles as well as agglomerates. Only measurements of individual carbon black particles from the figures gave an estimate of the particle dimension. Examination of Figure 2-6 showed the smallest particle size to be approximately 25 nm. This particle size fell within the range of carbon black N-330 presented in Table 2-1. The measurement of the particle size in Figure 2-7 of the compound A was a bit more difficult. This difficulty was due to an artifact of the TEM image in which three-dimensional picture is represented in two dimensions. The best estimate of the smallest particle size was 40 – 50 nm. This value was somewhat low compared to the expected range of values from Table 2-1; however, since the dimensions were just typical values used in natural rubber compounds the error was acceptable. Thus the TEM supported the assumption that the size of the carbon black was likely the controlling factor in the difference in the heat capacity.
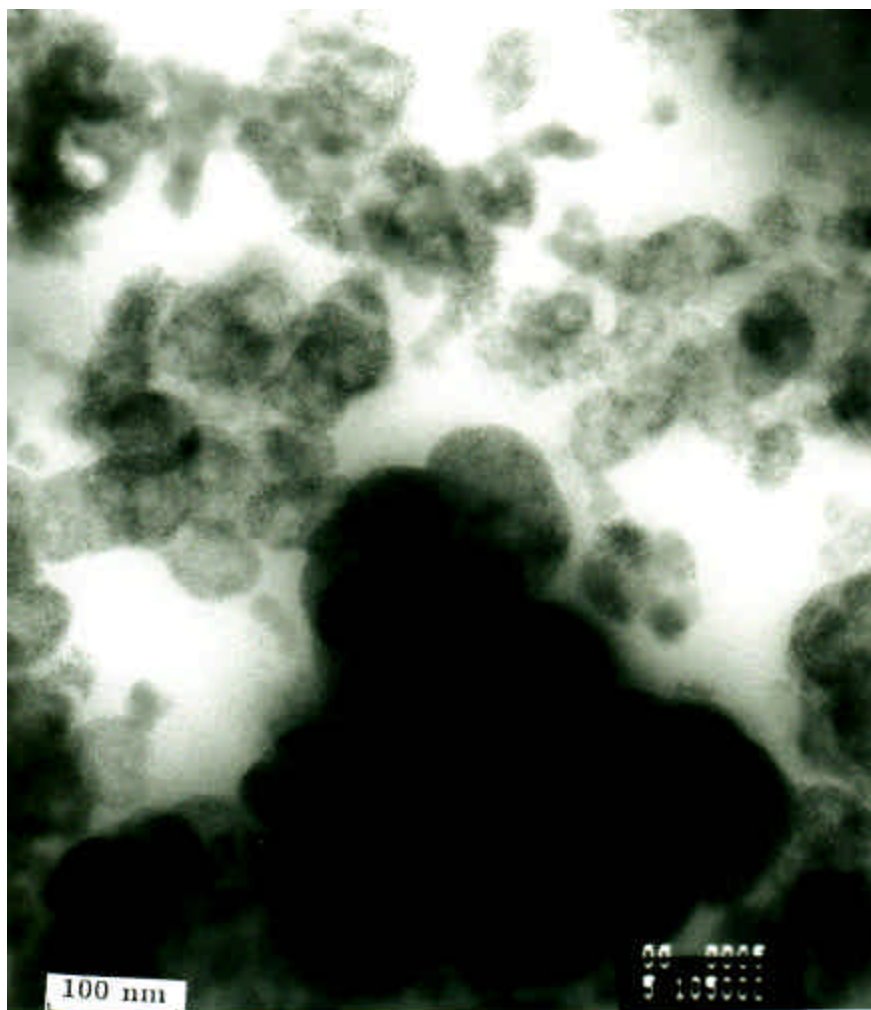
Figure 2-6   TEM image of compound B. The size scale is as shown.
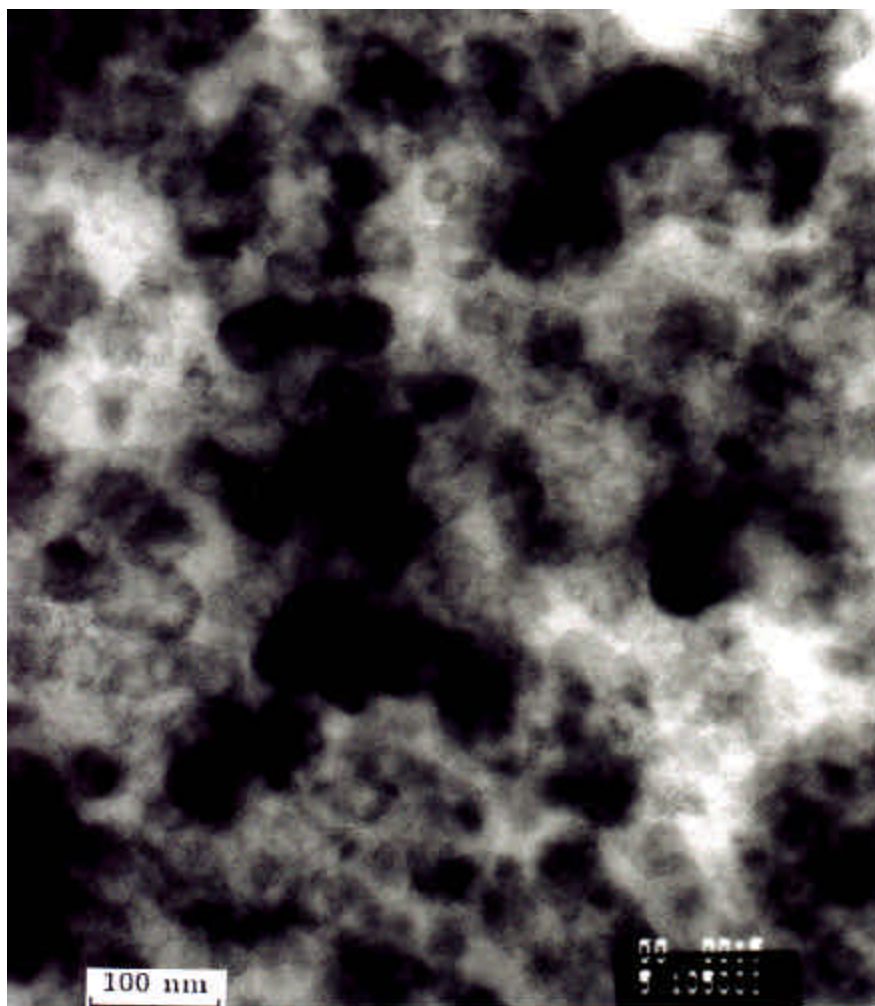
Figure 2-7 TEM image of compound A. The size scale is as shown.

2.4 Creep Rupture

Assuming that the particle size is known and that additional particles such as zinc oxide, cobalt stearate, or insoluble sulfur[68] are significantly smaller than the carbon black, the effect of these particle sizes on the mechanical properties can be evaluated. In order to examine this possible effect, creep rupture tests were performed. Creep rupture was chosen so that the behavior of the compounds as a function of time could be investigated. The time scale of the creep rupture testing allowed for the behavior of the compounds to be compared over several orders of magnitude in time.

The creep rupture tests were performed using a Texture Technologies Corporation Texture Analyzer XT2i. Dogbone samples were punched out of the sheeted compound using a die punch from the Dewes-Gum Die Company. The specimen overall dimensions were 22.5 x 7.7 x 2 mm, while the gage section of the dogbone was 10 x 2.7 x 2 mm. In order to reduce grip-induced failure the specimens were tabbed with 180 grit sandpaper. The dogbones were loaded in displacement control at the rate of 95 mm min^{-1} and held at a constant load until failure. The initial displacement rate was chosen to be fast so as to reduce any possible viscoelastic relaxation of the material that may occur during loading. Compound B was tested at three temperatures: 23, 60 and 90°C, while compound A was tested at 23 and 90°C. Elevated temperatures were obtained via a feedback controlled resistive heating system placed inline with the Texture Analyzer. Rupture time was calculated as the time spent at the constant applied load. Figure 2-8 and Figure 2-9 show the creep rupture behavior of both compounds.
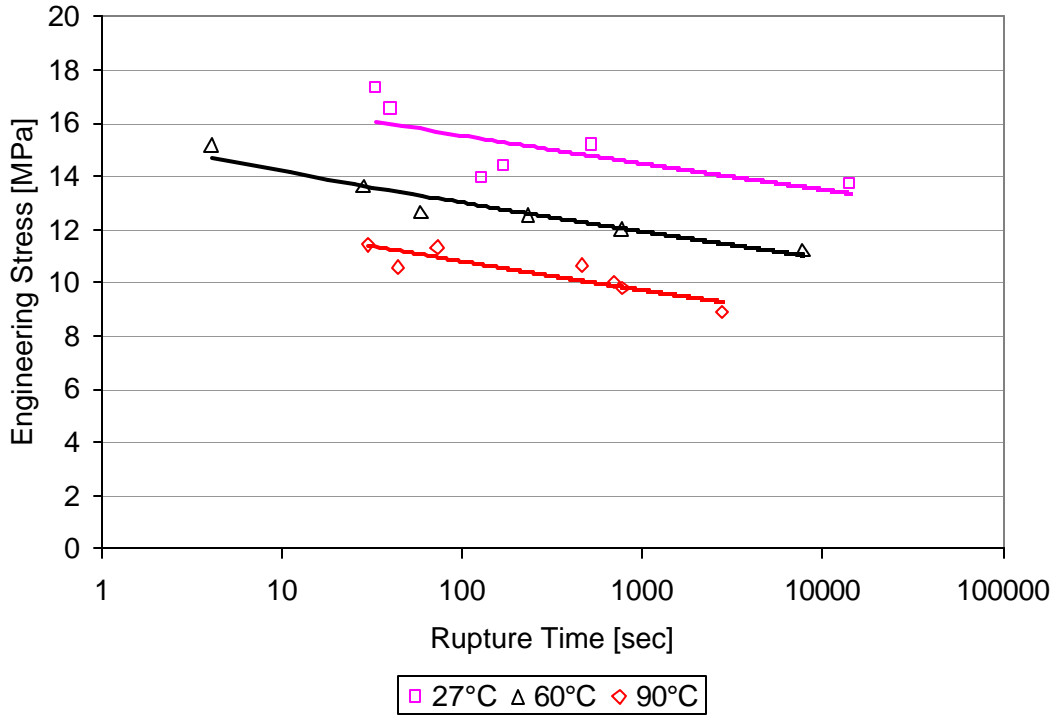
Figure 2-8   Creep rupture behavior of compound B.

Individual examination of Figure 2-8 and Figure 2-9 showed that the rupture behavior of the two compounds was as expected where the time to rupture for a particular stress level decreased with increased temperature. Furthermore, the behavior of both compounds could be fit with a power-law type expression and the data did not contain significant scatter. The slopes of the rupture data at the individual isotherms were similar thus leading to the belief that the curves should shift well into a master curve.
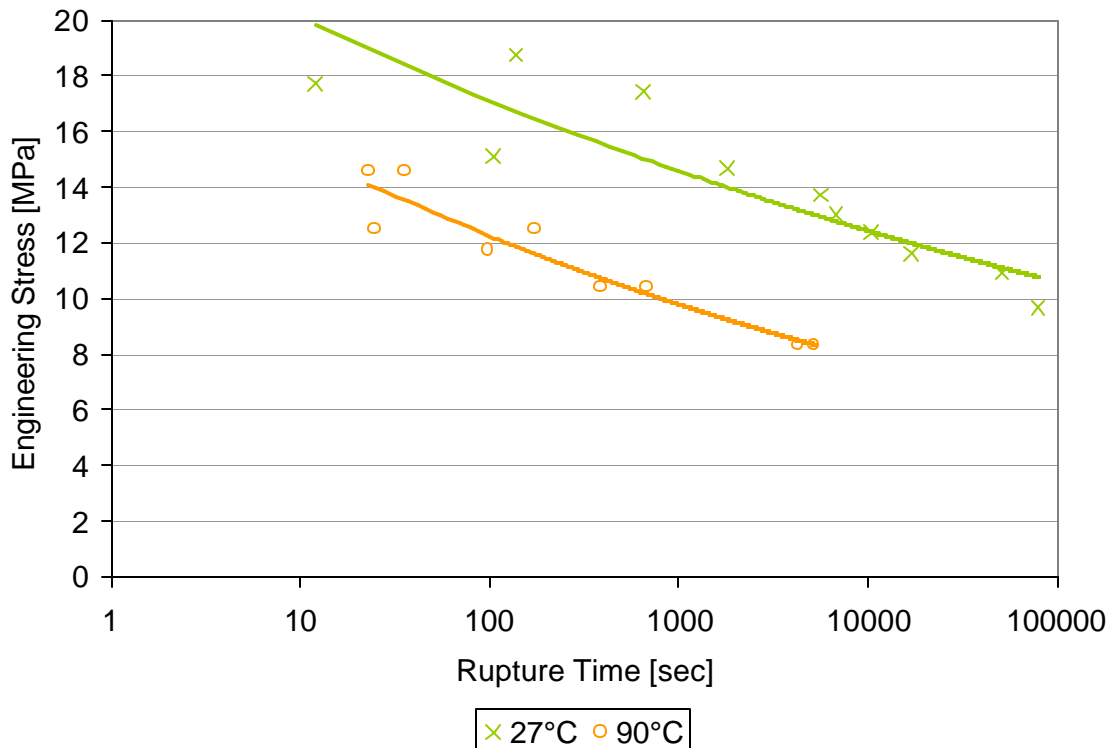
Figure 2-9   Creep rupture behavior for compound A.

A comparison of the creep rupture behavior between compound A and compound B at 23 and 90°C is presented in Figure 2-10. There were significant differences between the time dependent behaviors of the two compounds. For high loads compound A lasted significantly longer than compound B; however, at lower loads the two curves crossed and compound A ruptured before compound B One possible explanation for this rupture behavior is the strain amplification factor[24]. When carbon black is incorporated, the degrees of freedom of the rubber chains are decreased due to the interaction and adsorption of non-deformable carbon black into the rubber. The result is that upon an applied load the rubber must bear the total strain; however, the local strain within the rubber phase is greater than the global strain attained by the system. This difference is termed the strain amplification factor. Neogi et al.[24] found that for compounds containing the same level of carbon black particles the strain amplification factor decreases with increasing particle size. This decrease was attributed to the decrease in the amount of bound rubber between the carbon black particles. Thus compound A would

45

possess less bound rubber than compound B. Following the result of Neogi et al.[24] the argument can be made that the inclusion of the larger carbon black particles would result in the material lasting longer because of the decreased level of bound rubber i.e. more of the rubber was constrained. At high stress levels this reduction of bound rubber results in more of the load being carried by the particles; however, at the lower stress levels the particles may act more as flaws rather than reinforcement. It is possible that at the lower stress levels the higher levels of unbound rubber in compound A have less resistance to creep than compound B at the same stress level. The higher level of bound rubber in compound B may produce a higher level of strain-induced crystallization. This crystallization would serve to retard creep of the compound, thus leading to the longer rupture times. This is seen in Figure 2-10
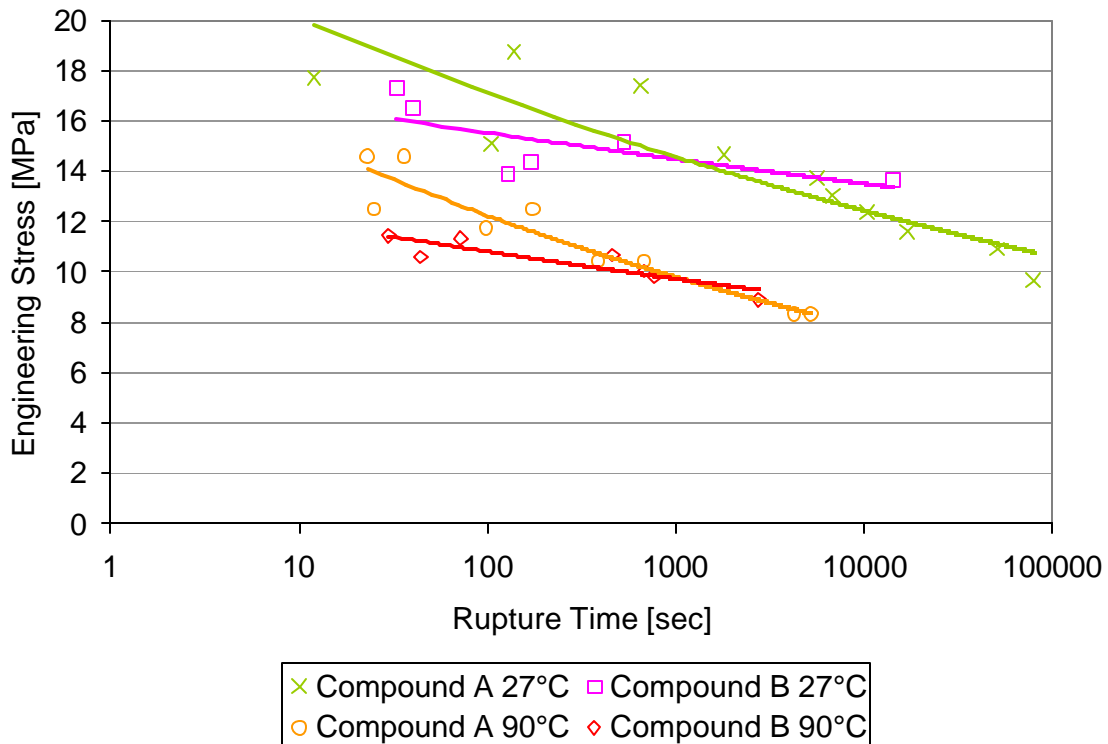
Figure 2-10   Comparison plot of the creep rupture behavior between compound A and compound B at 27 and 90°C.

46

2.7 Compound Seasonal Variation

Tire compounding can often be referred to as a black art. While the basic formulation of the compound is consistent over time there are variations that occur with the seasons. These variations are due to the local humidity at the time of manufacture and the desire to obtain the optimum cure conditions so as to achieve the most efficient tire manufacturing capacity of the plant. Figure 2-11 shows the effect that the seasonal variation in the compounds can have on the creep rupture behavior.
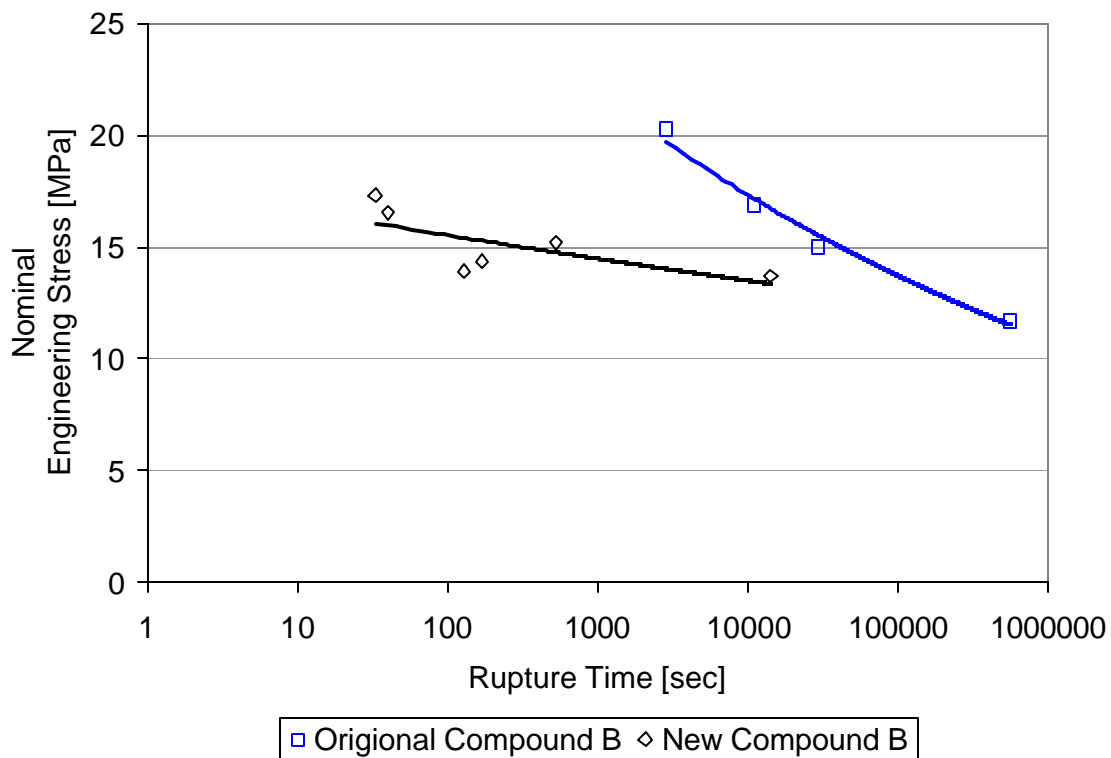
Figure 2-11   The effect of the seasonal variation upon the mechanical properties of tire compounds. The original compound B was manufactured in the late fall early winter while the new compound B was manufactured in late spring.

The figure shows compound B from two different manufacturing batches. The original compound B was produced during the early winter months while the new compound B was produced during the late spring. Both compounds underwent the same cure history; however, the difference

between the two was clearly noticeable. In order to avoid errors in the mechanical testing of the compounds all mechanical testing will be performed on the new compound B.

3.   THERMAL AGING AND CHEMICAL DATA

Compound A and compound B have been anaerobically thermally aged. This approach is a broadened test matrix from that of Huang et al.[37] whom investigated the effect of thermal aging on NR at only 100°C. The purpose of the aging was to track the extent of rubber reversion with time at elevated temperature. Thermal aging in natural rubber is a step process, where polysulfidic crosslinks revert to disulfidic, disulfidic to monosulfidic and monosulfidic crosslinks revert ultimately back to the gum state. Tracking the extent of rubber reversion was performed by determining the changes in the percentages of polysulfidic and monosulfidic crosslinks as well as the total crosslink density with time at elevated temperature[37-40]. Using this chemical data, a master curve relationship has been developed for the changes in the percentages of the type of crosslinks as a function of aging time multiplied by a shift factor. The development of the master curve relation allows for the predictions of real world timescales using typical laboratory timescales. The master curves will be applied to the fatigue lifetime predictions using finite element modeling in chapter 8.

3.1   Thermal Aging

In order to perform the aging without increasing the rate of oxidation due to the elevated temperature, all aging occurred anaerobically under isothermal conditions. To achieve isothermal anaerobic aging, sheets of compound were placed in a mylar foil bag and the bag was evacuated. In this first method the ambient oxygen was removed from the sample prior to isothermal aging. Due to the fact that the evacuation of the sheets occurred prior to aging, any small molecules produced during aging were trapped within the sample and not pumped out during the evacuation.

3.1.1 Thermal Aging Conditions

The aging temperatures and times for the sheets were 80, 100, 120°C for 3, 6, 12 and 24 days. These temperatures and times were chosen so as to mimic an industrial accelerated aging test.

3.2 Determination of Crosslink Type

The chemical determination of the percent polysulfidic and monosulfidic crosslinks was performed using a vulcanizate analysis[70]. The types of crosslinks were identified through the use of chemical probes in conjunction with the determination of the total crosslink density. The analysis for the types of crosslinks was based upon the chemical reactivity of the particular chemical probe. The total crosslink density was determined by swelling tests. Samples of the compounds were immersed in a low molecular solvent, heptane, and allowed to swell. The solvent was changed twice before the final mass of the swollen sample was measured. By changing the solvent any uncured polymer present in the sample was allowed to dissolve into the solvent. This led to an accurate value of the total crosslink density as well as the determination of the levels of soluble polymer within the material due to aging. The interaction parameter between the vulcanizate and the heptane was calculated based upon literature values[71,72]. It was found that the interaction parameter, χ, was 0.52.

The chemical probes allowed for the separate determination of the mono, di and polysulphic crosslinks. The chemical reactivity of tri, tetra and higher sulfides could not be separated out by the probes because they are chemically similar. The analysis was based upon the fact that S-S bonds undergo an exchange reaction with thiolate ions. Equilibrium was set up with di and polysulfic crosslinks by:

$$R'S^- + RS.SR \leftrightarrow R'S.SR + RS^- \qquad [3.1]$$

$$R'S^- + R'S.SR^- \leftrightarrow R'S.SR' + RS^- \qquad [3.2]$$
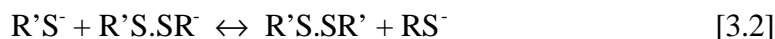
Equilibrium depended upon the nature of the R and R' groups. The exchange reaction may be driven to completion by use of an excess thiolate ion if the groups are chemically similar. If R in equation 3.1 is a rubber chain, all the di and polysulfidic crosslinks, RS.SR, can be cleaved if R'S⁻ is sufficiently reactive and sufficiently soluble in a solvent which will swell the rubber to provide an adequate excess of the

reagent. The sulphur-sulphur bond in polysulfidic crosslinks are more susceptible to nucleophilic attack by thiolate ions than the sulphur-sulphur bond of the disulphidic crosslinks. Provided a thiolate ion of limited reactivity was chosen, only the tri and higher sulfides would be attacked leaving the di and mono sulfides intact. This selective attack was achieved by use of a secondary thiolate ion in dilute solution.

The determination for the quantity of mono and disulfidic crosslinks was treatment of the vulcanizate with a solution of propane-2-thiol (0.4 M) and 0.4 M piperidine in heptane at 20°C for 2 hours. This treatment broke polysulfidic crosslinks according to equation 3.1 leaving di and monosulfidic crosslinks intact.

$$RS_xR + (2x\text{-}3)Me_2CHS^- \rightarrow RSSCHMe_2 + RS^- +$$

$$(x\text{-}2)S^{2-} + (x\text{-}2)Me_2CHSSCHMe_2 \qquad\qquad [3.3]$$

The treatment for the cleavage of di and polysulfidic crosslinks was exposure of the vulcanizate to 1 M hexane I-thiol in piperidine for 48 hours at 25°C. The polysulfidic crosslinks were cleaved according to equation 3.3, while the disulfides were cleaved according to equation 3.1 with R' = n-hexyl.

The determination of the total crosslink density from swelling tests performed before and after treatment with the thiolate ion allowed for the summation of the individual contributions of the mono, di and polusufidic crosslinks.

3.3   Polysulfidic and Monosulfidic Master Curves

The results from the chemistry data allowed for the determination of the percentages of poly and monosulfidic crosslinks as functions of time at elevated temperature. This dependence with time is plotted in Figure 3-1, showing the dependence of the polysulfidic crosslinks for compound B. The data in the figure show that the decrease of the polysulfidic crosslinks with time follow an exponential decay. This decay is the same that reported by Huang et al[37]. The magnitude of the decay is dependent upon the aging temperature and increases with increasing temperature. The next step was to generate a master curve to capture this dependence of the crosslink distribution on time at elevated temperature.
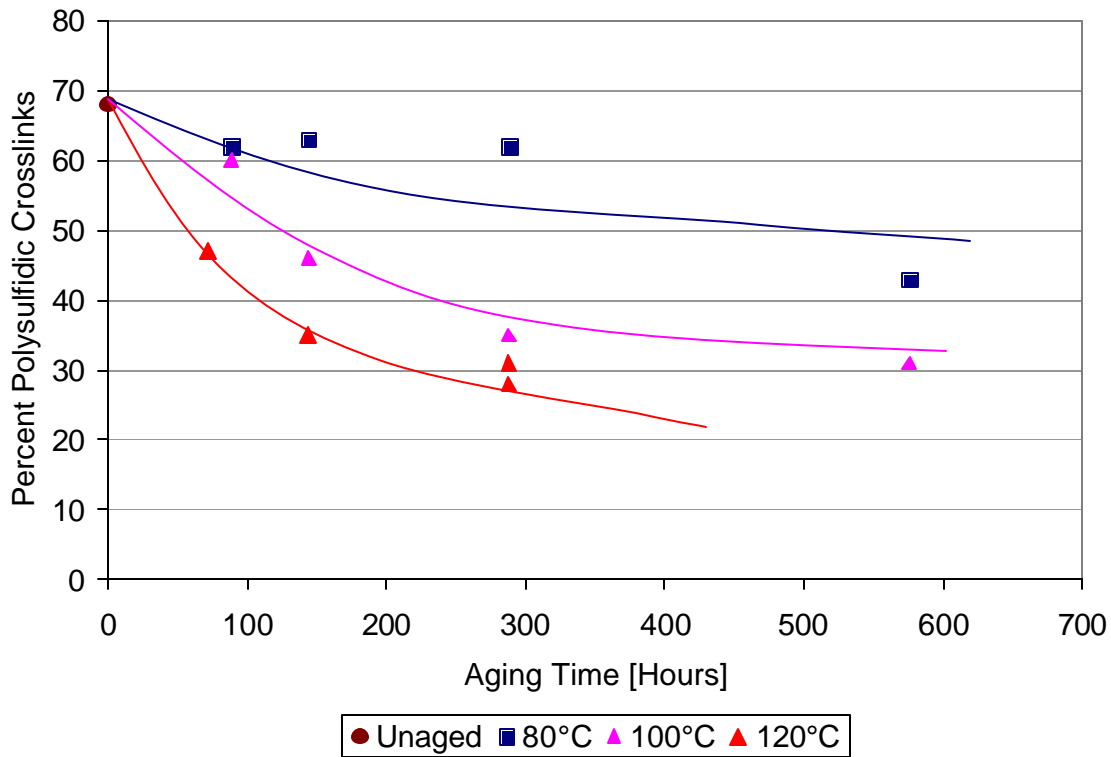
Figure 3-1 **Dependence of the percentage of polysulfidic crosslinks with time at elevated temperature for compound B.**

Time temperature superposition was utilized to generate master curves of the crosslink distribution as functions of reduced temperature, T - T_{ref}. Master curves were generated for both compound A and compound B with respect to the percentages of poly and monosulfidic crosslinks. Only horizontal shifting was employed in the generation of the master curves. Shift factor plots were generated and their acceptability was judged upon the following two criteria:

- Each shift factor plots is a reasonable shape containing no discontinuities.

- Each master curve is a reasonable shape containing no discontinuities.

Given that the aging effect being examined, thermochemical reversion, was not a viscoelastic phenomena and was occurring significantly far from the glass transition temperature the Willliams-Landel-Ferry equation, WLF, was not applicable.

3.3.1 Compound A

Figure 3-2 is a master curve of the percent of polysulfidic crosslinks versus log aging time plus the shift factor. The data converged very well into a master curve with no discontinuities, thus demonstrating that one mechanism is dominant. Figure 3-3 is the master curve of the percent of monosulfidic crosslinks versus log aging time plus the shift factor.
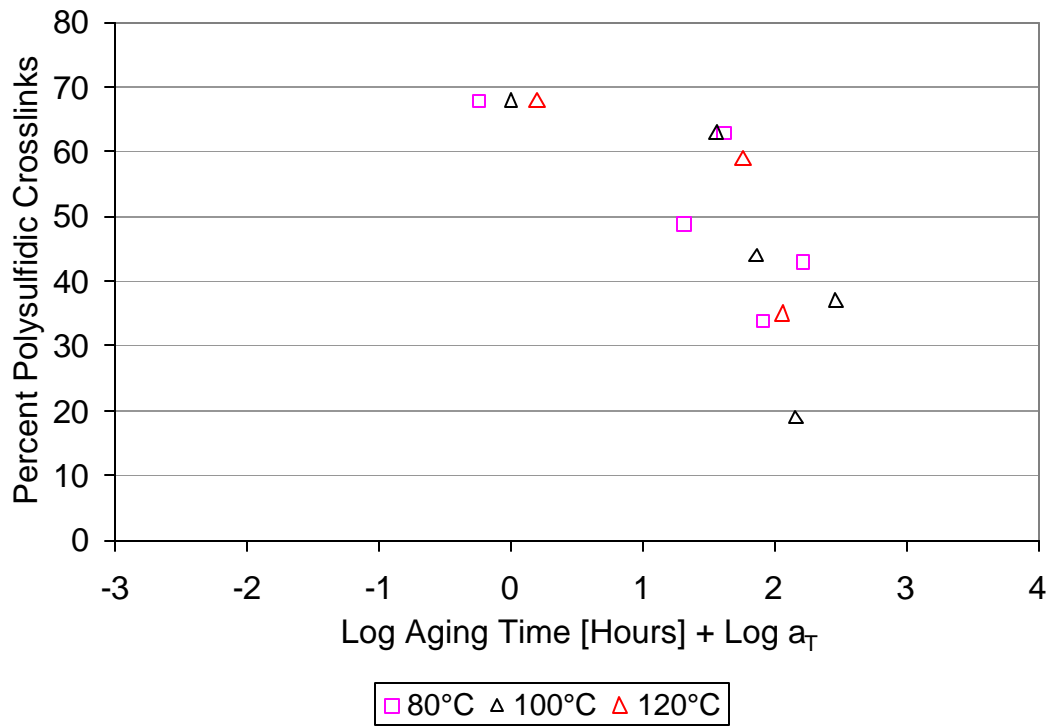
Figure 3-2 **Compound A master curve of the percent polysulfidic crosslinks versus log aging time. $T_{ref} = 100^{o}C$**
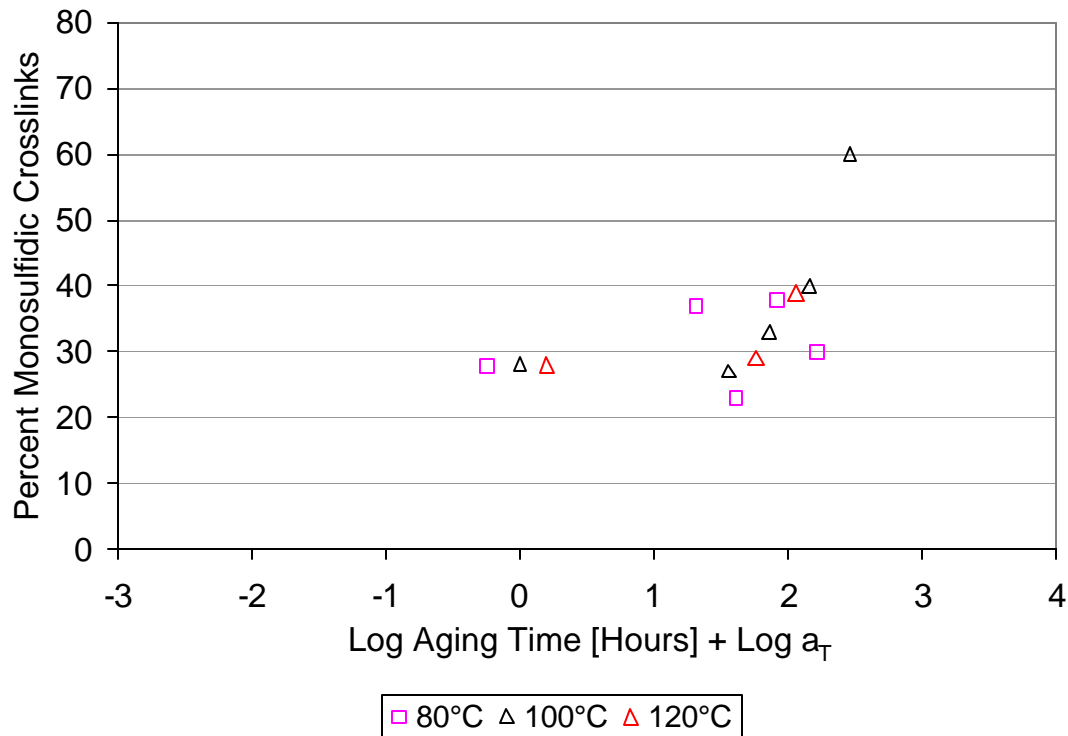
Figure 3-3 **Compound A master curve of the percent monosulfidic crosslinks versus log aging time + log a_T. $T_{ref} = 106^oC$**

The shift factor plot for compound A is presented in Figure 3-4. The same shift factors were applied for both the polysulfidic and the monosulfidic crosslinks. As can be seen in the figure, the shift factor plot was a reasonable shape and contained no discontinuities. Given that the shift factor plot was linear it was conjectured that thermochemical reversion was an Arrhenius activation energy driven process. The Arrhenius relation is shown as equation 3.4.

$$a_T = \exp\left(\frac{-E_a}{RT}\right) \qquad [3.4]$$

where: E_a is the activation energy,

            R is the gas constant and

            T is the absolute temperature.

The activation energy, E_a, was calculated from the slope of the log a_T versus T^{-1} plot shown as Figure 3-5. The activation energy for compound A was calculated to be 29.9 kJ mol^{-1}.
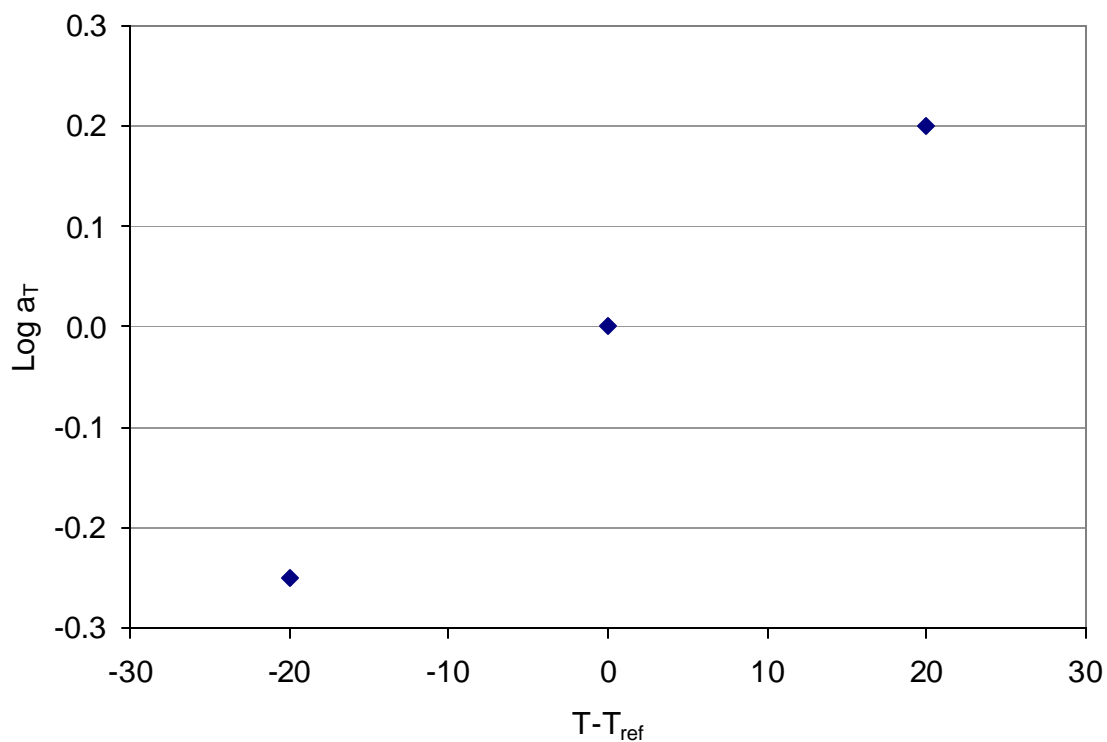
Figure 3-4   **Compound A shift factor plot, log a_T versus $T - T_{ref}$, for the percentage change of polysulfidic and monosulfidic crosslinks vs. log aging time $+ a_T$. $T_{ref} = 100°C$.**
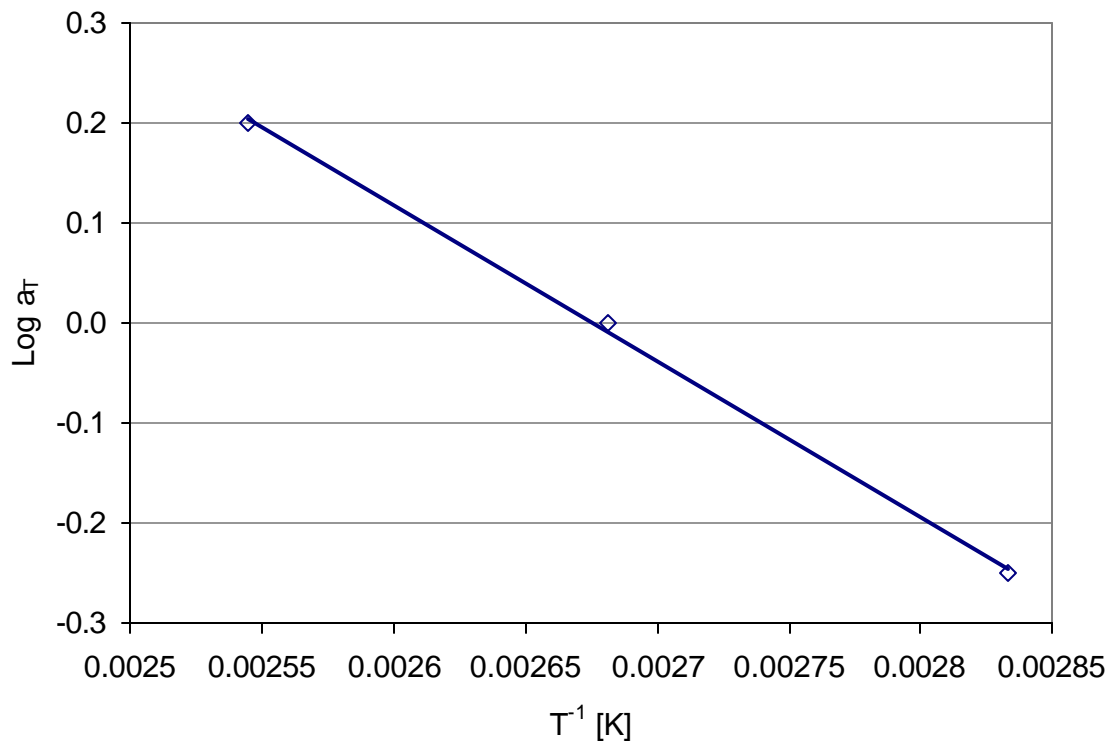
Figure 3-5   **Linearized arrhenius plot for the calculation of the Arrhenius activation energy for thermochemical reversion.**

3.3.2   Compound B

Utilizing the same process applied to compound A, master curves were generated for compound B. Figure 3-6 is a master curve of the percent of polysulfidic crosslinks versus log aging time + log a_T. As in the case of compound A, the data converged very well into a master curve with no discontinuities. Figure 3-7 is the master curve of the percent of monosulfidic crosslinks versus log aging time + a_T. Both the polysulfidic and the monosulfidic crosslink distribution reduced well into master curves. The same shift factors were applied for both the polysulfidic and the monosulfidic crosslinks. As with compound A the shift factor plot was a reasonable shape and did not contain any discontinuities.
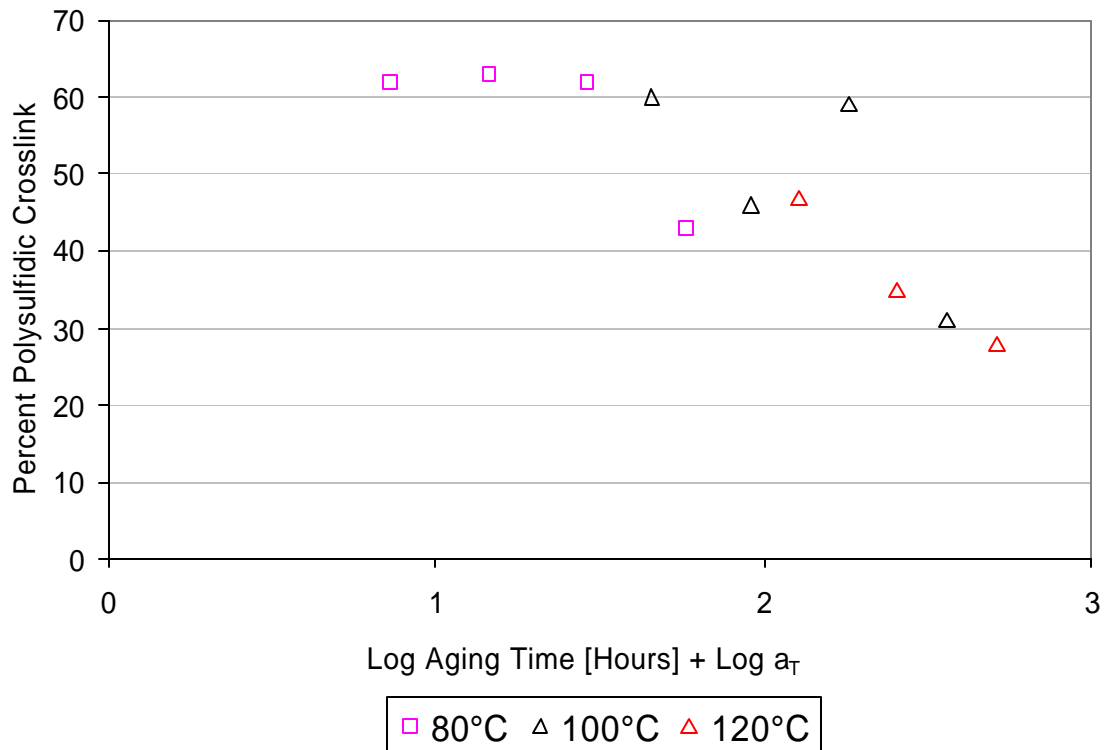
Figure 3-6 **Compound B master curve of the percent polysulfidic crosslinks versus log aging time. $T_{ref} = 106^oC$**

The activation energy for compound B was calculated by applying equation 3.6. The activation energy was calculated to be 83.3 kJ mol^{-1}. This value for E_a was nearly three times greater than that of compound A. This difference between the activation energies may be indicative of the different composition between the compounds A and compound B. However, given the fact that the exact composition of the compounds is unknown an accurate comparison of the activation energies could not be performed.
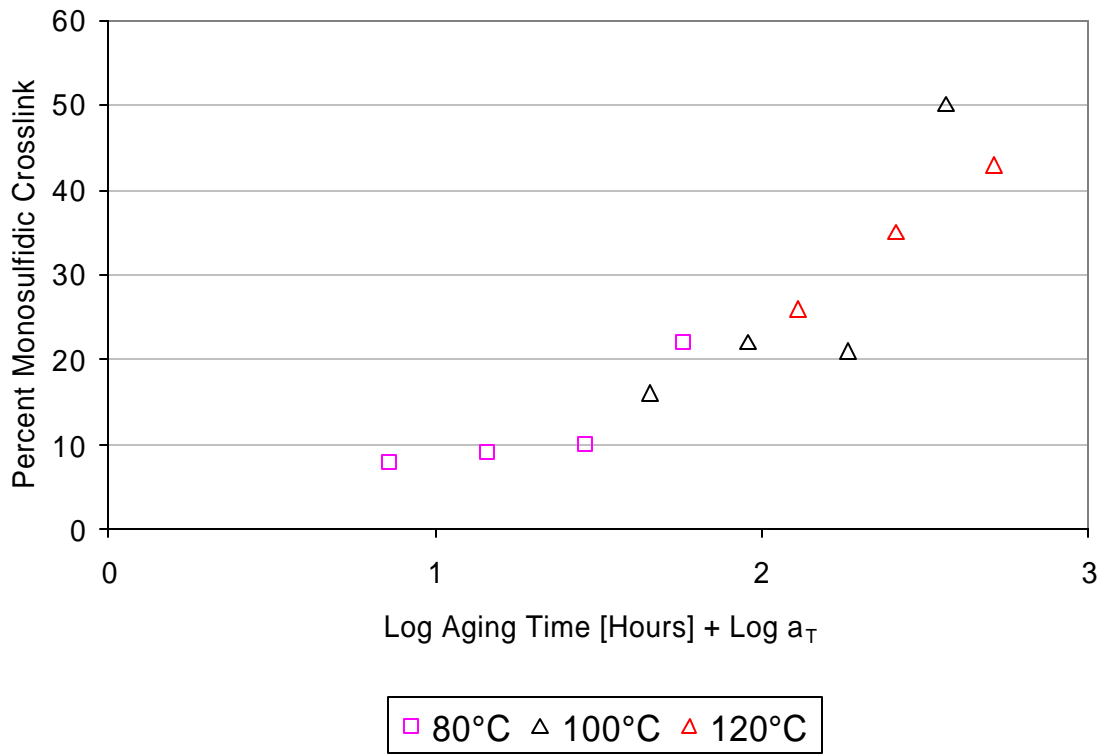
Figure 3-7 **Compound B master curve of the percent monosulfidic crosslinks versus log aging time. $T_{ref} = 103^{o}C$**
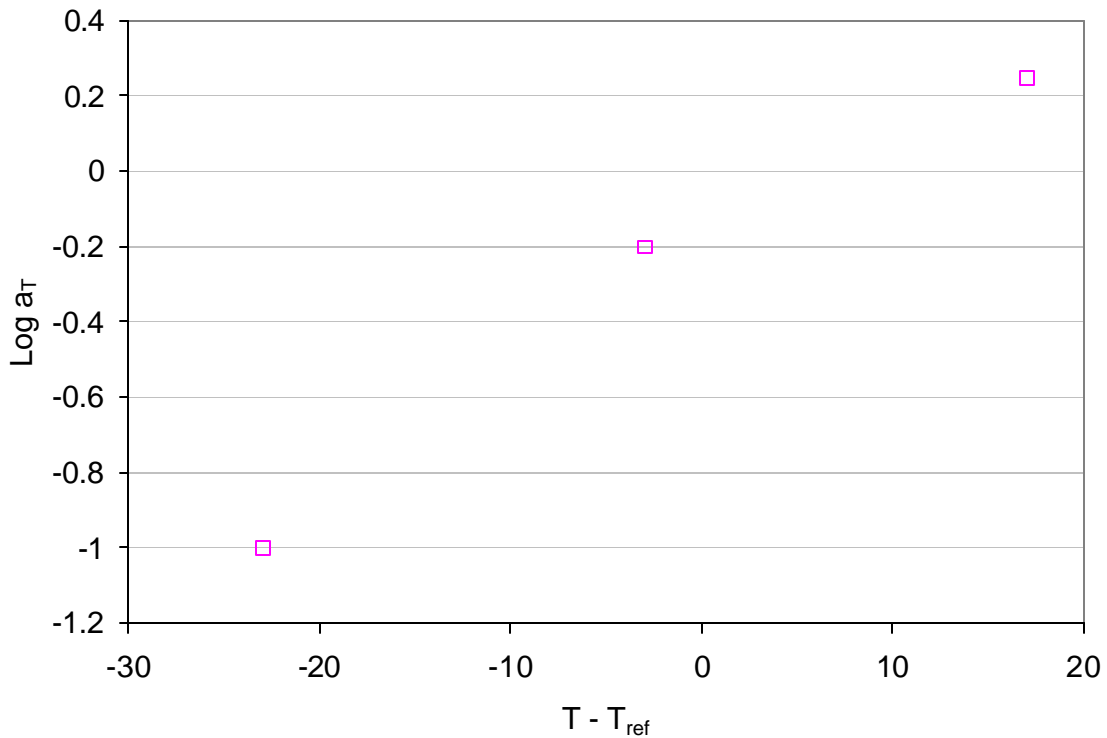
Figure 3-8 **Compound B shift factor plot, log a_T versus $T - T_{ref}$, for the percentage change of polysulfidic and monosulfidic crosslinks vs. log aging time + log a_T. T_{ref} = 103°C.**

3.4 Total Crosslink Density Master Curve

The dependence of the total crosslink density on time at elevated temperature was investigated. This dependence of the total crosslink density with time at elevated temperature for compound B is shown in Figure 3-9. Unlike the percentages of the crosslink distributions, the total crosslink density did not reduce into a master curve. The total crosslink density did not show the same exponential decrease with aging time, as did the distribution of crosslinks, Figure 3-1. While the total crosslink density data does not reduce into a master curve, the decrease in the total crosslink density with time at elevated temperature could be discerned. The total crosslink density did not reduce well into a master curve due to its initial increase and subsequent decrease with aging. The next step was to verify that the level of reverted or soluble polymer increased with increasing time at elevated temperature.
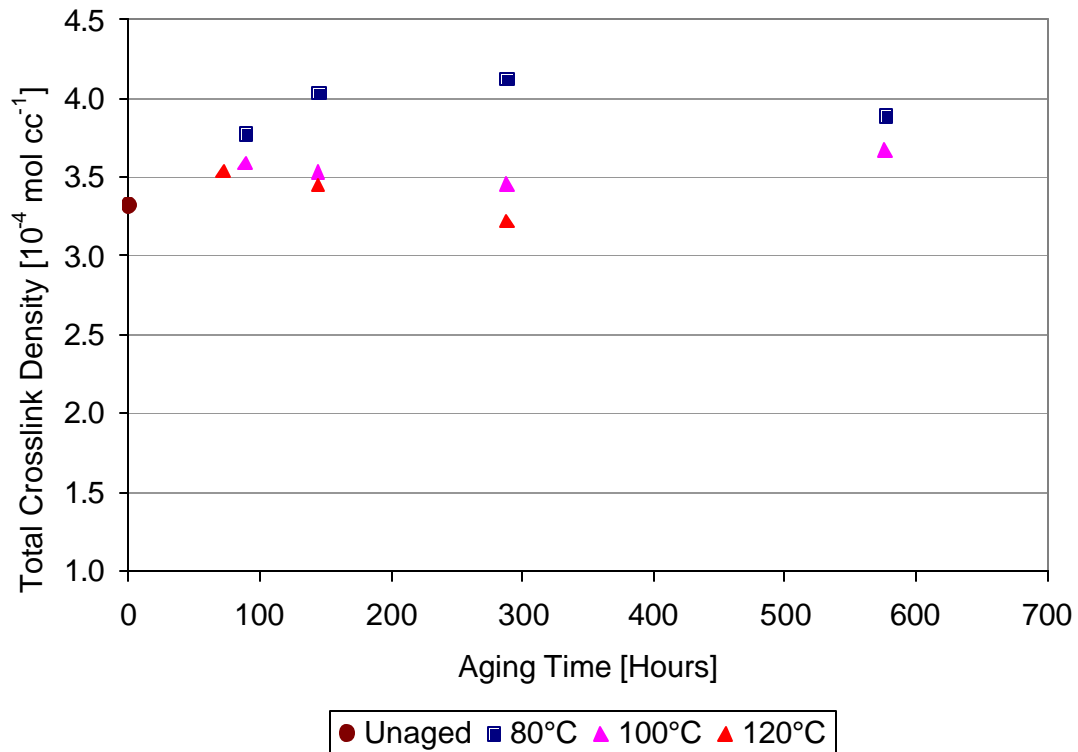
Figure 3-9 **Dependence of the total crosslink density with time at elevated temperature for compound B.**

3.5 Soluble Polymer

As the extent of reversion increases, so should the levels of soluble polymer within the compound. The levels of soluble polymer were obtained during the swelling test portion of the vulcanizate analysis. Soluble polymer levels increased as reversion progressed and polymer went from the vulcanized to the gum state. A master curve of the weight percent of soluble polymer for compound B has been generated, Figure 3-10. Similar to the poly and monosulfidic crosslinks, the data reduced well into a master curve. The shift factor plot, Figure 3-11, was a linear function and contained no discontinuities. Applying equation 3.6, the activation energy was calculated to be 119.6 kJ mol^{-1}.
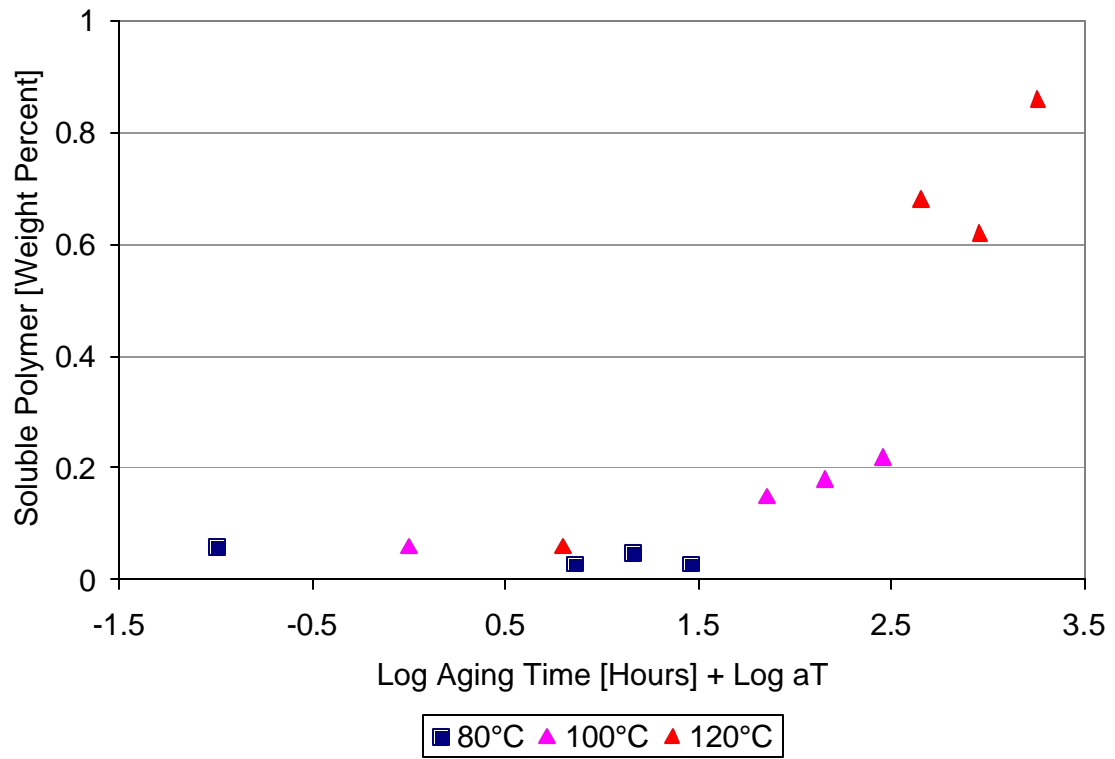
Figure 3-10   Weight percentage of soluble polymer master curve for compound B. T_{ref} = 100°C.
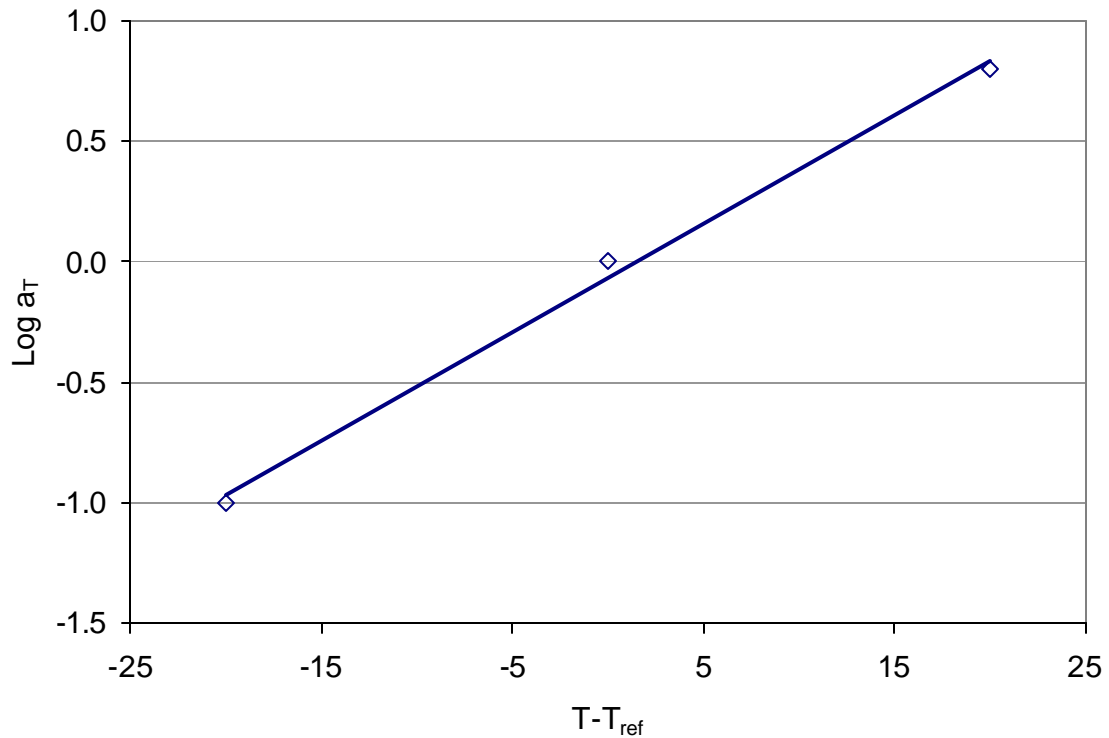
Figure 3-11   Shift factor plot, log a_T versus $T - T_{ref}$, for the weight fraction change of soluble polymer vs. log aging time + a_T. $T_{ref} = 100^{o}C$.

3.6   Summary

Application of time temperature superposition provided the means to track the changes in the chemistry of the vulcanizate with time at elevated temperature.   In order to perform predictions of cord-rubber composites structures these changes in chemistry must be related to the mechanical properties. Chapter 4 will discuss the relation between the changes in the chemistry with the reduction of quasi-static mechanical properties. The relation with the dynamic properties will be discussed in chapter 6 and crack propagation in chapter 7 and chapter 8.

4.   QUASI-STATIC TESTING

In order to determine the ultimate stress, ultimate strain, modulus and shear strength of the aged and unaged compounds quasi-static testing has been performed. The ultimate stress, ultimate strain and modulus were determined by displacement controlled testing using an ASTM D412-D dog bone specimen. All testing was conducted at room temperature at a constant displacement rate of 95 mm min^{-1}. This displacement was chosen in an attempt to reduce any viscoelastic effects. In order to calculate the modulus, the stress versus strain response of the compounds was approximated as a linear function, Figure 4-1. The linear nature of the compounds was attributed to their high percentage of filler and high degree of crosslinking.
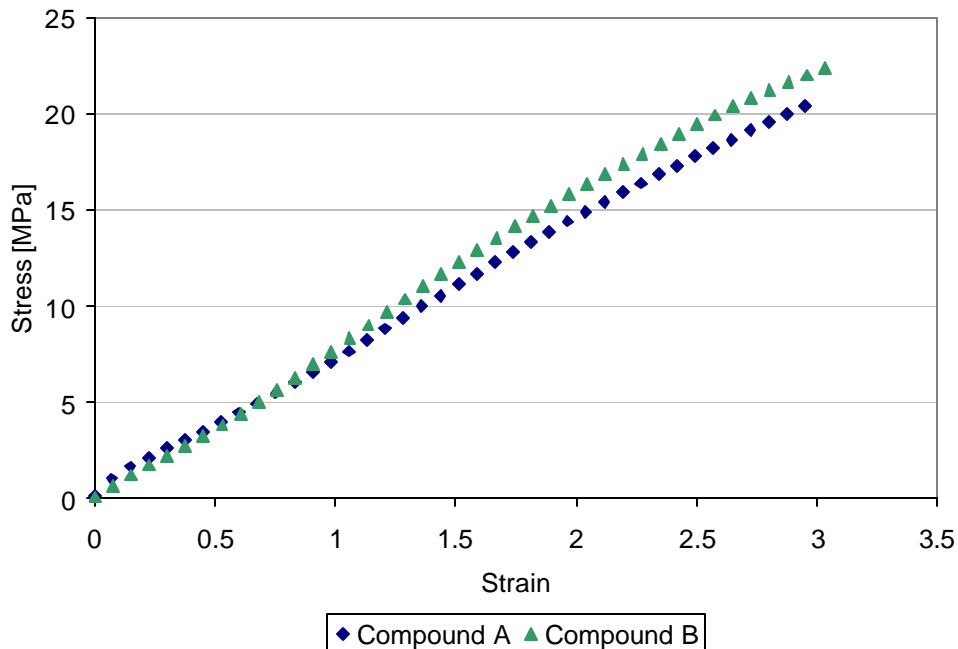
Figure 4-1   Stress versus strain response of compound A and compound B.

The shear strength of the materials was obtained using an ASTM D732 standard test method for shear strength of plastics by punch tool[73]. The punch was used to test both the aged and unaged compounds.

The mechanical properties were correlated with the crosslink distribution. The ultimate stress, ultimate strain, modulus and shear strength were plotted as functions of the changes in the percent poly and monosulfidic crosslinks as well as the total crosslink density. This correlation between the quasi-static mechanical properties will link the rubber reversion at elevated temperature to the reduced quasi-static mechanical properties of the compounds.

4.1   Ultimate Stress

4.1.1   Compound A

All of the quasi-static properties of the compound A presented are the average of three individual tests.

The dependence of the ultimate stress on the percent polysulfidic, monosulfidic crosslinks as well as the total crosslink density are presented in Figure 4-2 -Figure 4-4. For the both the poly and the monosulfidic crosslinks there was a linear correlation with the ultimate stress, with a 27% reduction i.e. the ultimate stress due to thermal aging. The ultimate stress was reduced from 18 to 13 MPa. The trend was that the higher the percentage of polysulfidic crosslinks the greater the mechanical property. This dependence with the polysulfidic crosslinks was expected from the research of Nasir et al.[40], who found that the high levels of polysulfidic crosslinks gave rise to better mechanical properties. These mechanical properties include: ultimate stress, ultimate strain and modulus. Following this argument there should have been no significant dependence of the ultimate stress with the total crosslink density, which was the case shown in Figure 4-4. The plot of ultimate stress as a function total crosslink density showed no significant trend.
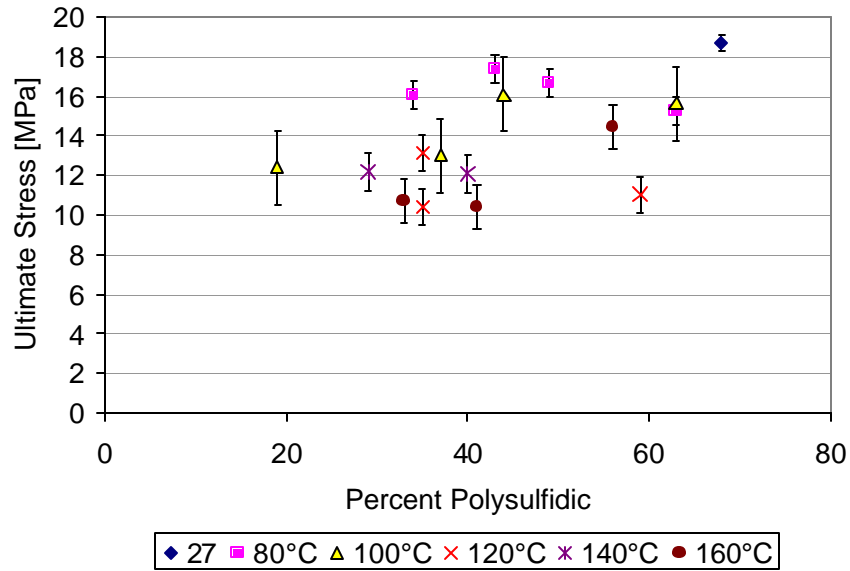
Figure 4-2 **Compound A ultimate stress versus the percentage of polysulfidic crosslinks. The error bars represent one standard deviation.**
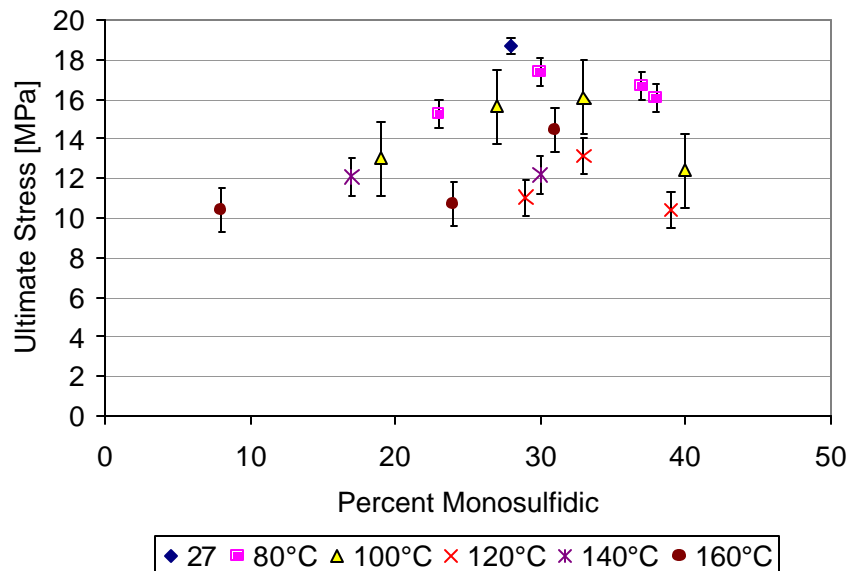
Figure 4-3 **Compound A ultimate stress versus the percentage of monosulfidic crosslinks. The error bars represent one standard deviation.**
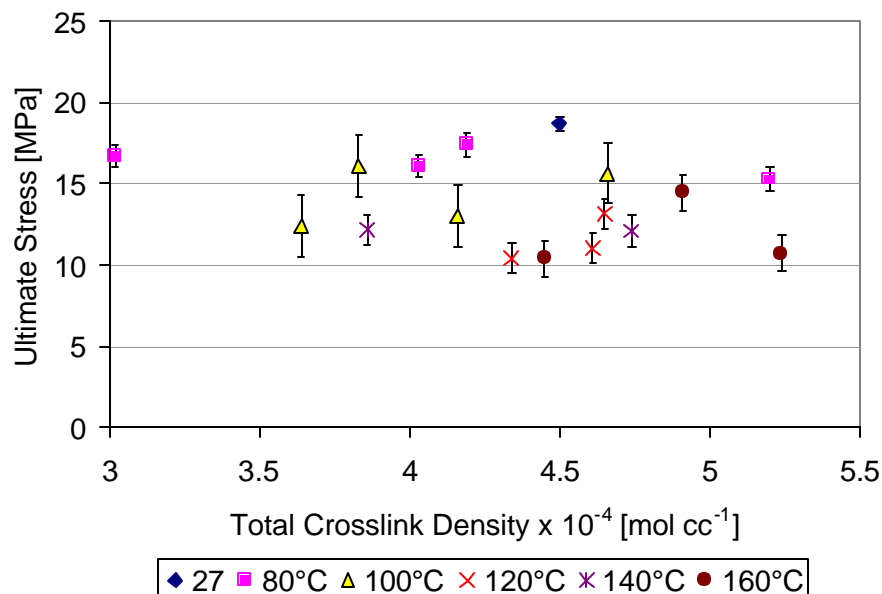
Figure 4-4   **Compound A ultimate stress versus the total crosslink density. The error bars represent one standard deviation.**

4.1.2   Compound B

All of the quasi-static properties presented for compound B are the average of five individual tests.

The dependence of the ultimate stress of compound B on the percent polysulfidic and monosulfidic crosslinks as well as the total crosslink density are presented in Figure 4-5 - Figure 4-7. There was a linear correlation between the ultimate stress and the percent poly and monosulfidic crosslinks. This linear correlation was in agreement with the results of by Nasir et al[40]. In general the higher mechanical properties were associated with the higher level of polysulfidic crosslinks. The ultimate stress was reduced from 21 to 13 MPa as the percentage of polysulfidic crosslinks fell from 68 to 18%. However, unlike compound A, the ultimate stress of the behavior of compound B correlated moderately with the total crosslink density.
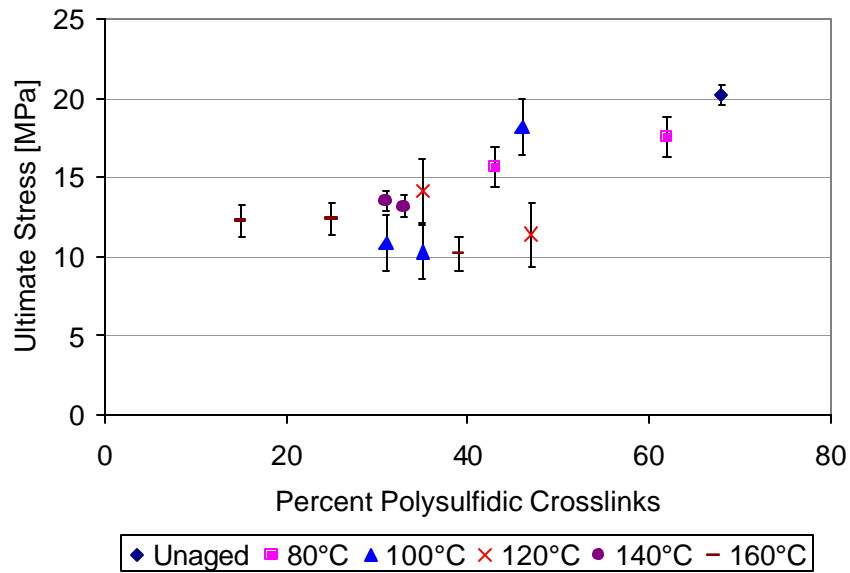
Figure 4-5   **Compound B ultimate stress versus the percentage of ploysulfidic crosslinks. The error bars represent one standard deviation.**
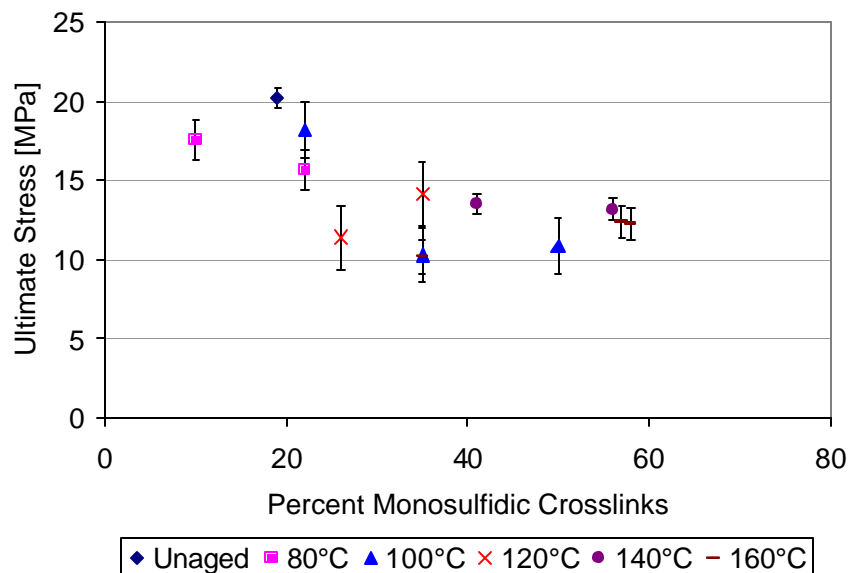
Figure 4-6   **Compound B ultimate stress versus the percentage of monosulfidic crosslinks. The error bars represent one standard deviation.**
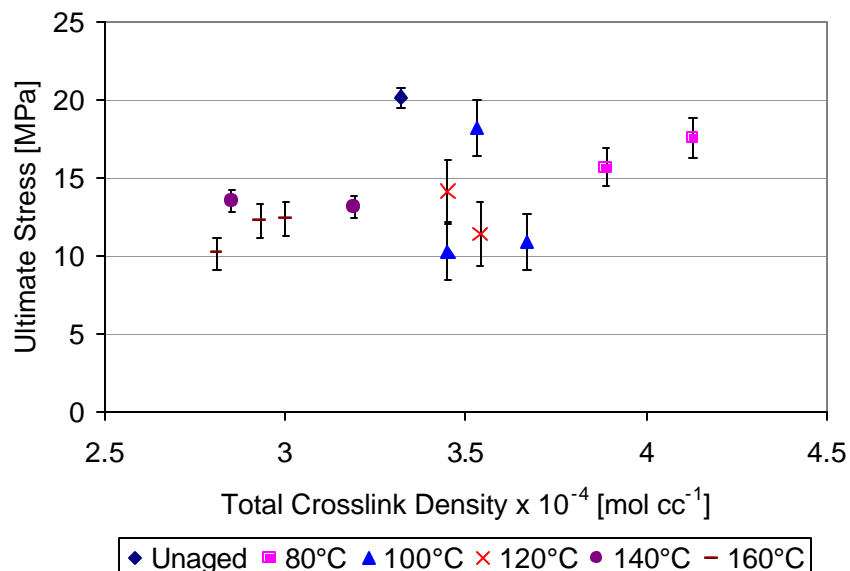
Figure 4-7 **Compound B ultimate stress versus the total crosslink density. The error bars represent one standard deviation.**

4.2   Ultimate Strain

4.2.1   Compound A

Figure 4-8 - Figure 4-10 present the dependence of the ultimate strain on the percent polysulfidic, monosulfidic crosslinks as well as the total crosslink density.   Unlike the ultimate stress, there was a very low linear dependence of the ultimate strain with the percentage of poly and monosulfidic crosslinks. The strains ranged from 3.0 to 2.3, as the percentage of polysulfidic crosslinks are reduced from 68 to 5%. The ultimate strain showed no distinct trends with the total crosslink density.
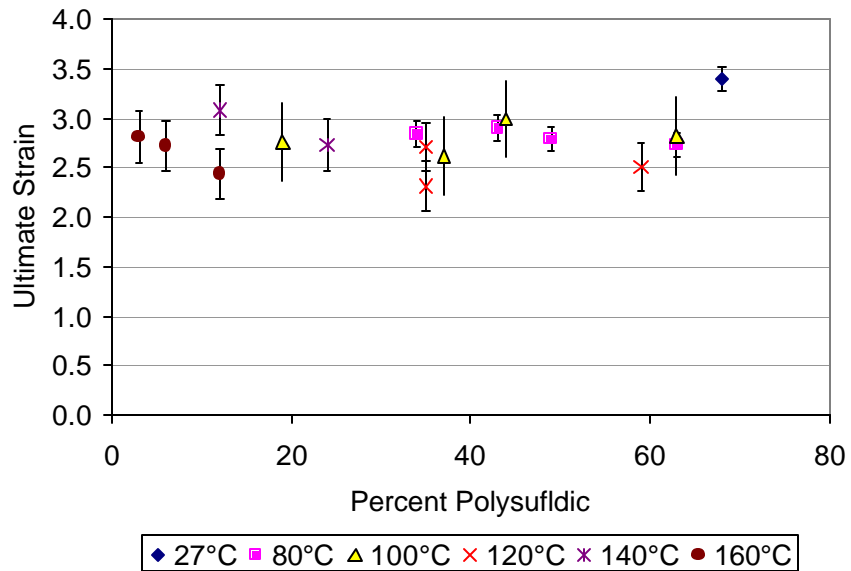
Figure 4-8 Compound A ultimate strain versus the percentage of polysulfidic crosslinks. The error bars represent one standard deviation.
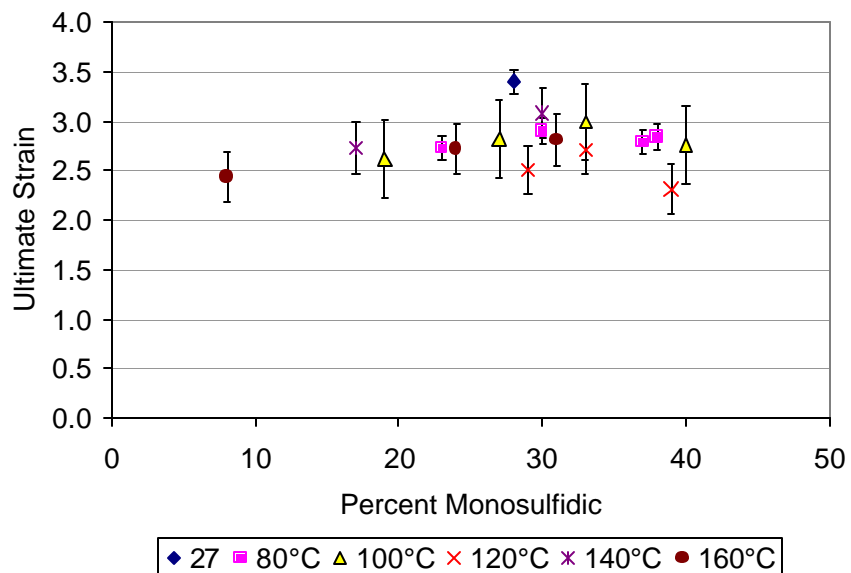
Figure 4-9 Compound A ultimate stress versus the percentage of monosulfidic crosslinks. The error bars represent one standard deviation.
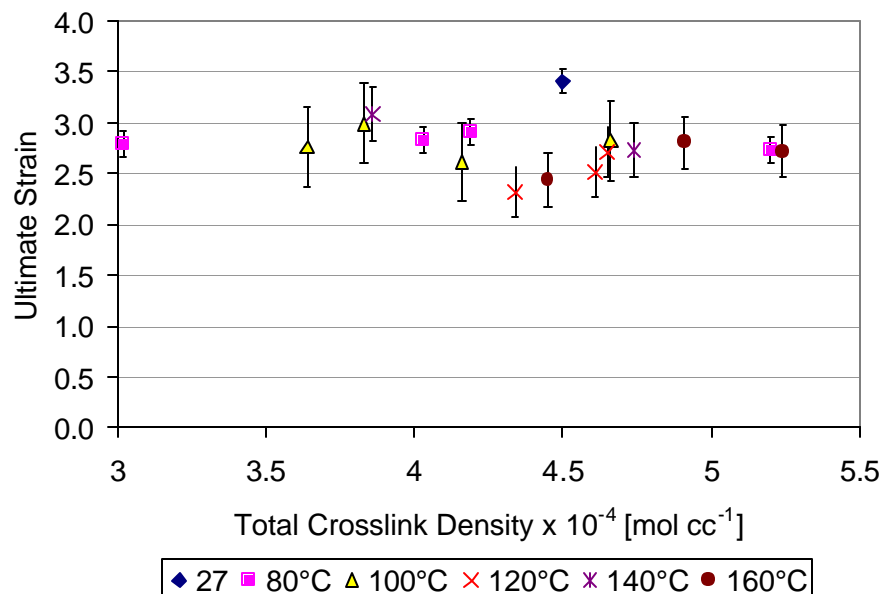
Figure 4-10 **Compound A ultimate stress versus the total crosslink density. The error bars represent one standard deviation.**

4.2.2 Compound B

Figure 4-11 - Figure 4-13 present the dependence of the ultimate strain on the percent polysulfidic, monosulfidic crosslinks as well as the total crosslink. Like the ultimate strain for compound A, there was a very low linear dependence of the ultimate strain with the percentage of poly and monosulfidic crosslinks. The strains ranged from 2.8 to 3.7, as the percentage of polysulfidic crosslinks are reduced from 68 to 18%. There was a large amount of scatter in the mechanical test data for polysulfidic crosslinks between 30 and 50%. The ultimate strain showed no distinct trends with the total crosslink density
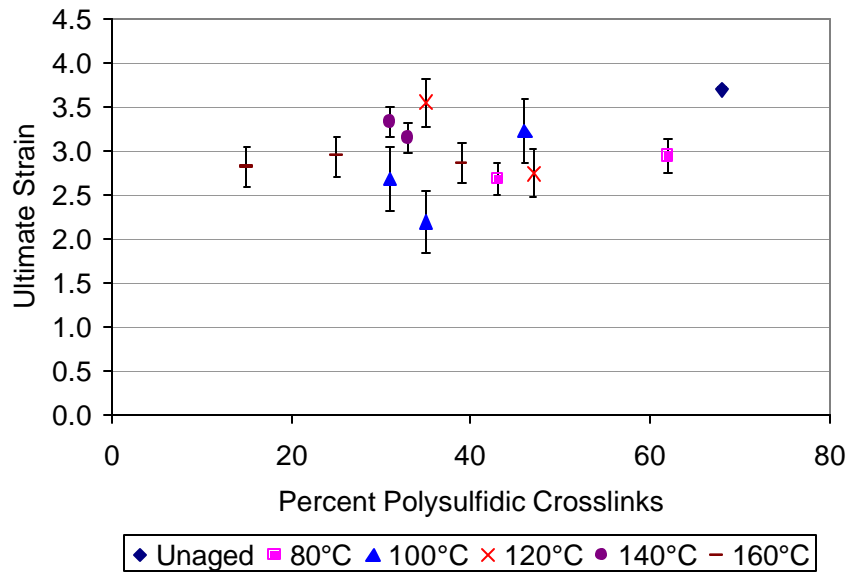
Figure 4-11 Compound B ultimate strain versus the percentage of polysulfidic crosslinks. The error bars represent one standard deviation.
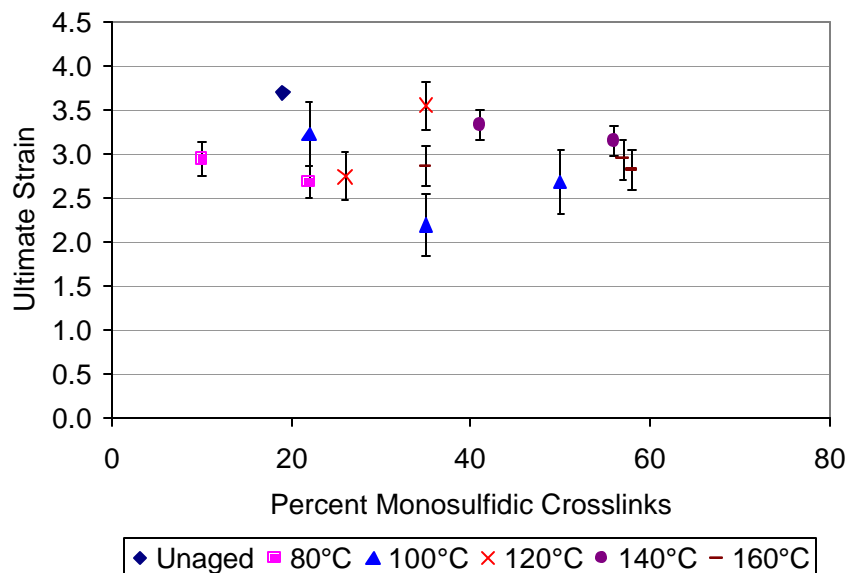
Figure 4-12 Compound B ultimate strain versus the percentage of monosulfidic crosslinks. The error bars represent one standard deviation.

71
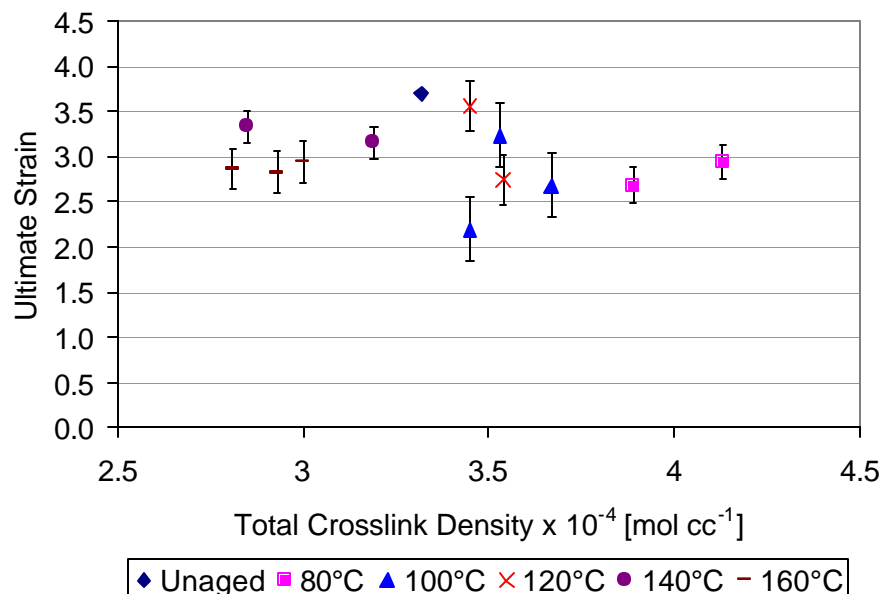
Figure 4-13   Compound B ultimate strain versus the total crosslink density. The error bars represent one standard deviation.

4.3   Youngs Modulus

4.3.1   Compound A

The dependence of the initial Young's modulus upon the crosslink distributions is shown in Figure 4-14 - Figure 4-16. There was the same linear trend, as with the ultimate stress and ultimate strain, of decreasing mechanical properties with decreasing percentage polysulfidic crosslinks; however, the linear trend was less apparent. There appeared to be no significant change in the modulus of the compound with the total crosslink density, Figure 4-16. This lack of trend contrasted with the M_c^{-1} dependence that would be predicted from the theory of rubber elasticity:

$$E = \frac{3\,rRT}{M_c} \qquad\qquad [4.1]$$

This difference may be attributed to the fact that in the derivation for equation 4.1 the small strain assumption is applied to relate the deformation ratios to the engineering strain. All the test data here are

the result of "full" quasi-static tests out to strains on the order of 300%. At the large values of strain the small strain assumption is not applicable. This may account for the lack of agreement between the data and equation 4.1.
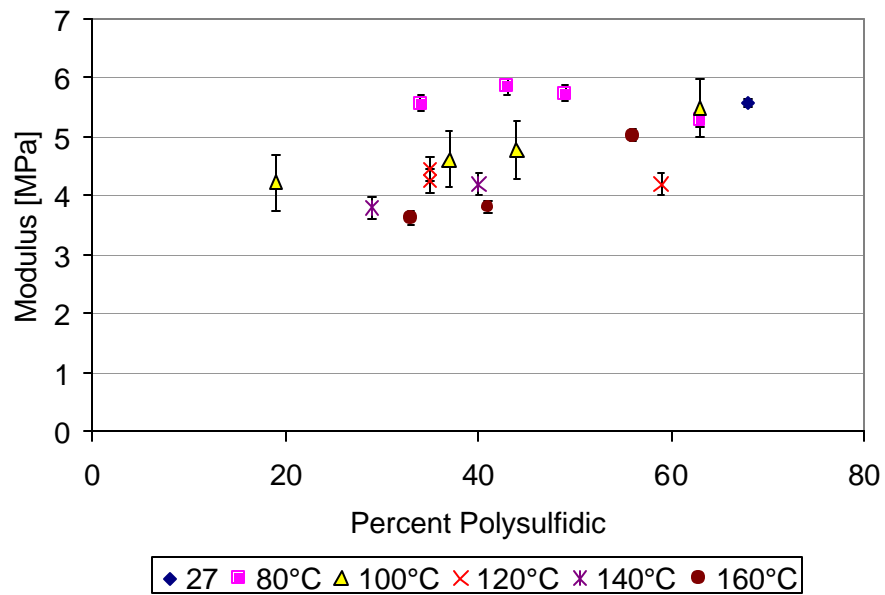
Figure 4-14 Compound A modulus versus the percentage of polysulfidic crosslinks. The error bars represent one standard deviation.
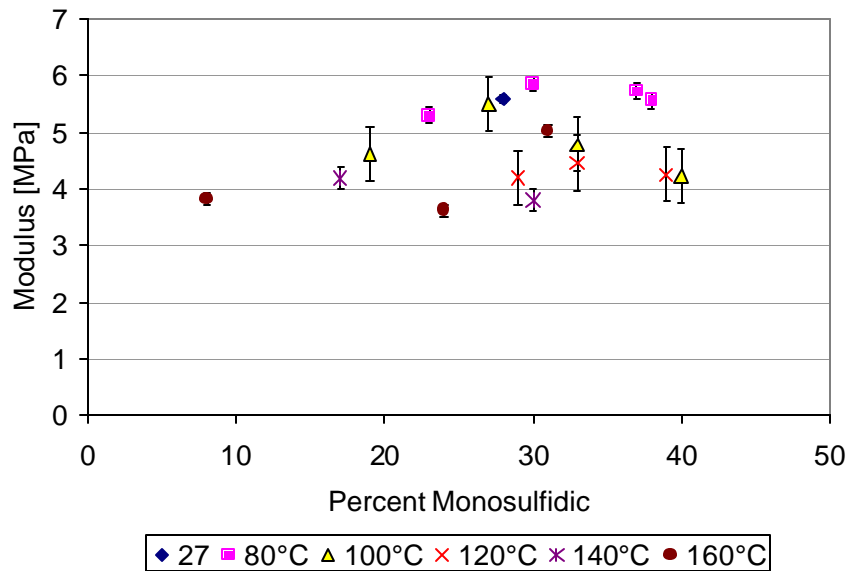
Figure 4-15 Compound A modulus versus the percentage of monosulfidic crosslinks. The error bars represent one standard deviation.
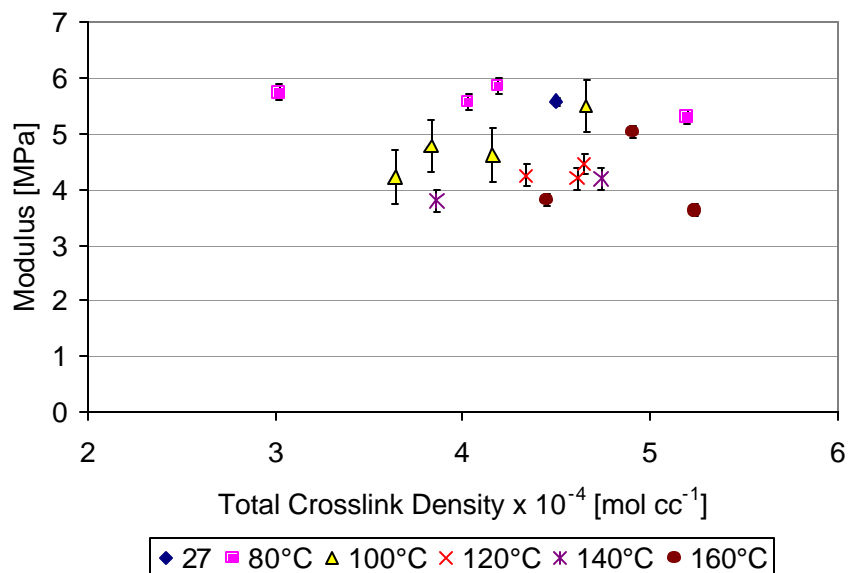
Figure 4-16 Compound A modulus versus the total crosslink density. The error bars represent one standard deviation.

4.3.2 Compound B

The dependence of the modulus upon the crosslink distributions is shown in Figure 4-17 - Figure 4-19. Unlike the ultimate strain there was a stronger dependence with the crosslink distribution. The dependence was a linear trend with the higher level of polysulfidic crosslinks giving rise to better mechanical properties. Unlike the modulus of compound A, there was a significant correlation of the modulus on the total crosslink density. The modulus followed the opposite trend of that expected from theory of rubber elasticity, equation 4.1, with the higher level of crosslinking yielding the highest modulus values.
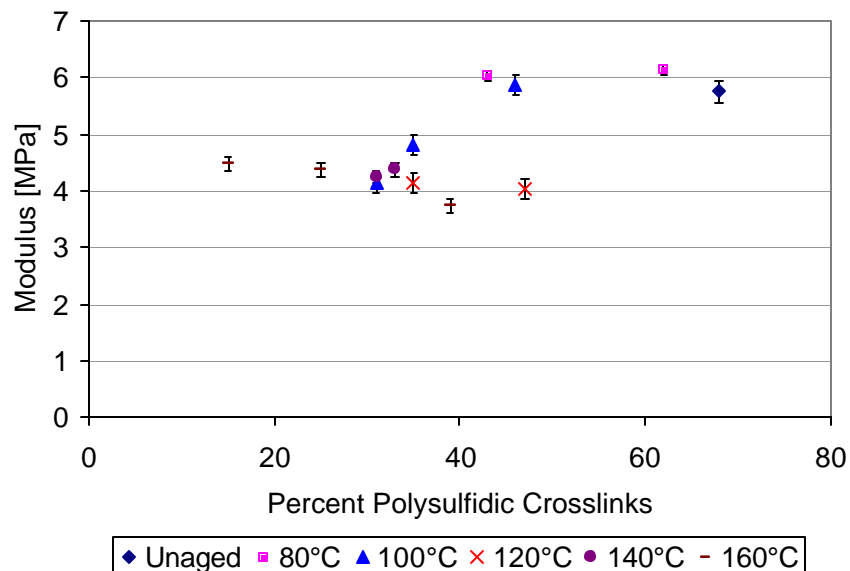
Figure 4-17   Compound B modulus versus the percentage of polysulfidic crosslinks. The error bars represent one standard deviation.
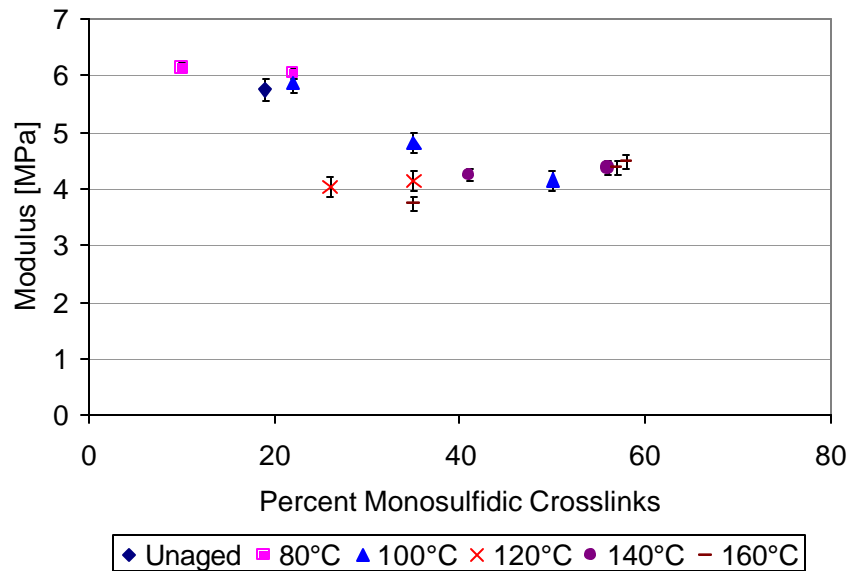
Figure 4-18   Compound B modulus versus the percentage of monosulfidic crosslinks. The error bars represent one standard deviation.
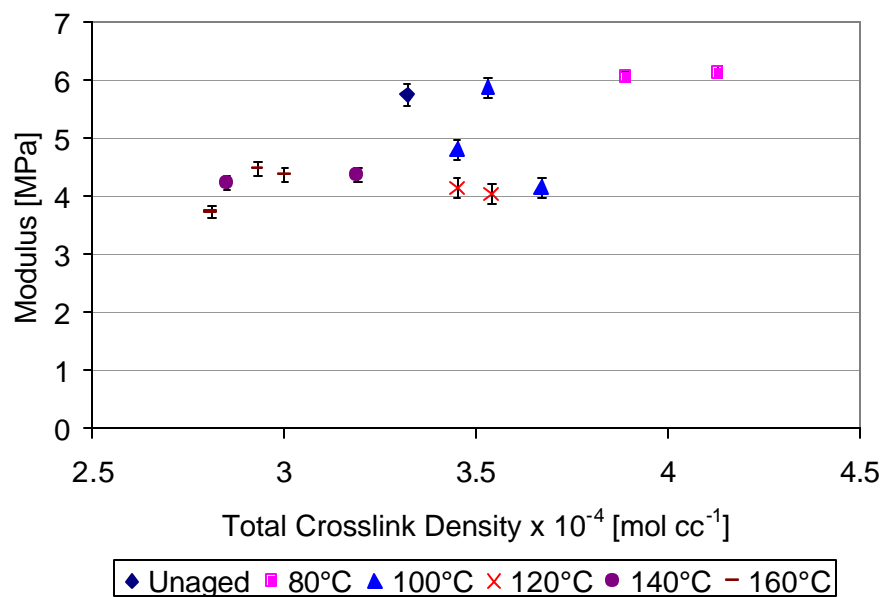
Figure 4-19   Compound B modulus versus the total crosslink density.

4.4   Shear Strength

The shear strength of the materials was obtained using an ASTM D732 standard test method for shear strength of plastics by punch tool[73]. The tests were conducted in displacement control at a constant rate of 95 mm min^{-1}.

The values of shear strength obtained from the test appeared reasonable and have very small error bars; however, there were no literature values of the shear strength of rubber to compare to. This lack of literature results from that fact that the high compliance of the rubber tends to turn shear testing into angled tensile testing. Application of the ASTM D732 fixture diminished this risk by placing the amount of tested compound in a highly constrained state.

The correlations of the shear strength with the crosslink distribution for compound A and compound B are shown in Figure 4-20 - Figure 4-25. The figures showed no dependence on the crosslink distribution for both compounds. The shear strength of compound A was slightly greater than that of compound B.
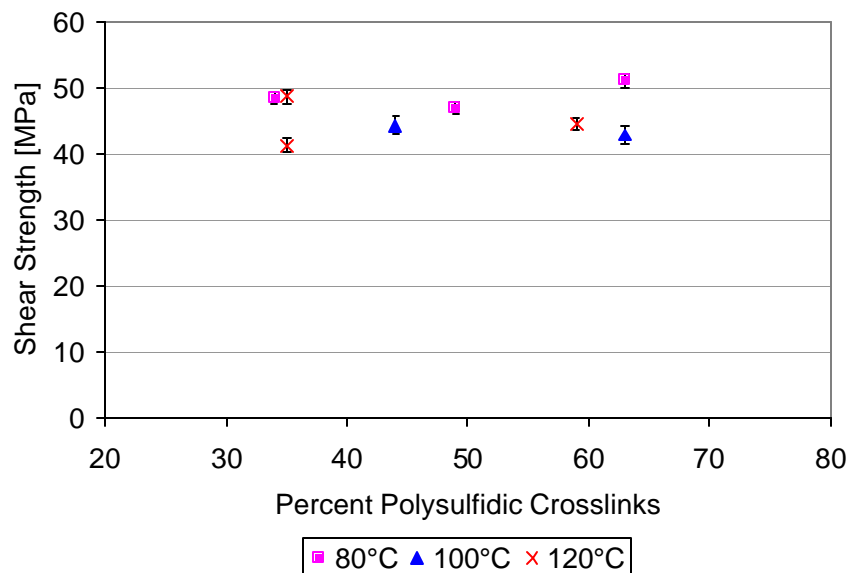
Figure 4-20   Compound A shear strength versus the percentage of polysulfidic crosslinks. The error bars represent one standard deviation.
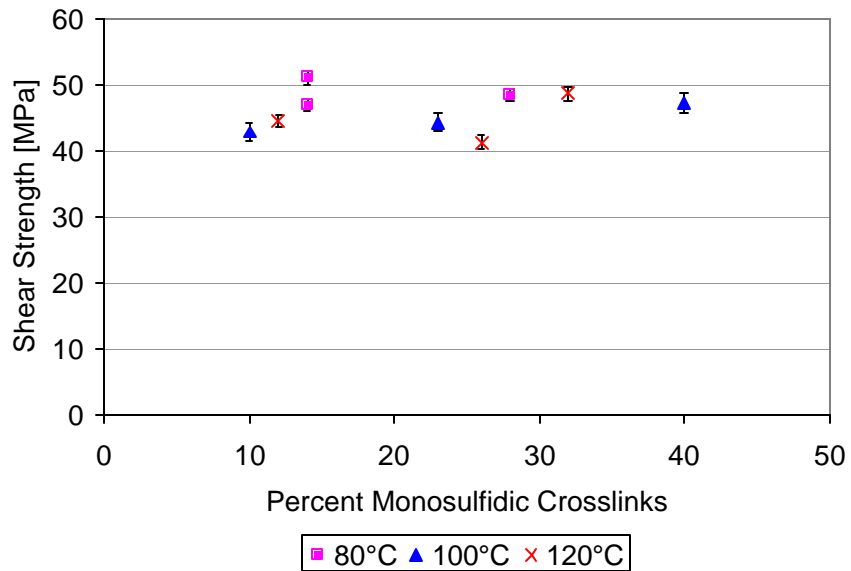
Figure 4-21   Compound A shear strength versus the percentage of monosulfidic crosslinks. The error bars represent one standard deviation.
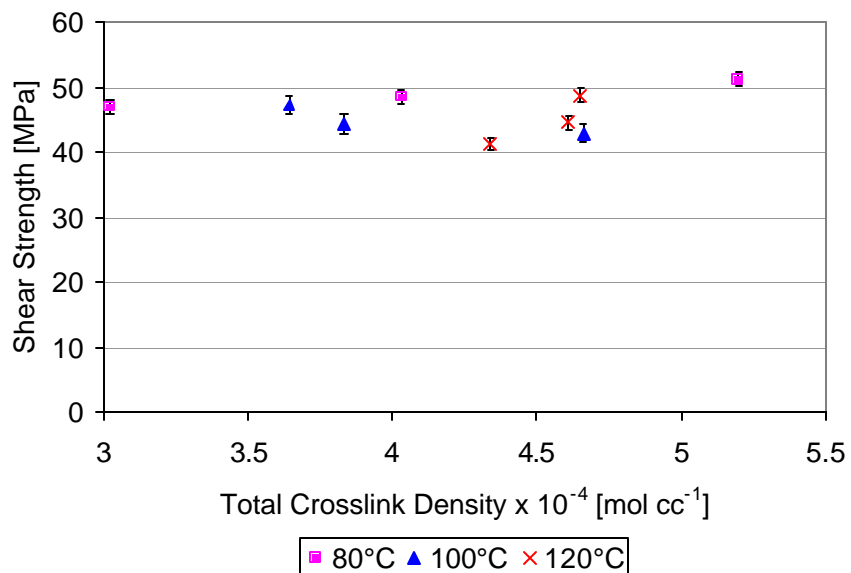
Figure 4-22   Compound A shear strength versus the total crosslink density. The error bars represent one standard deviation.
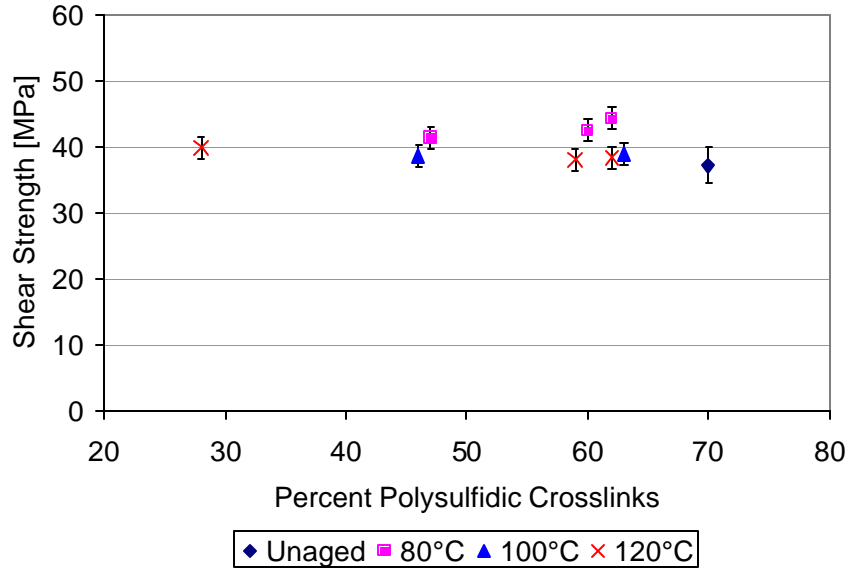
Figure 4-23 **Compound B shear strength versus the percentage of polysulfidic crosslinks. The error bars represent one standard deviation.**
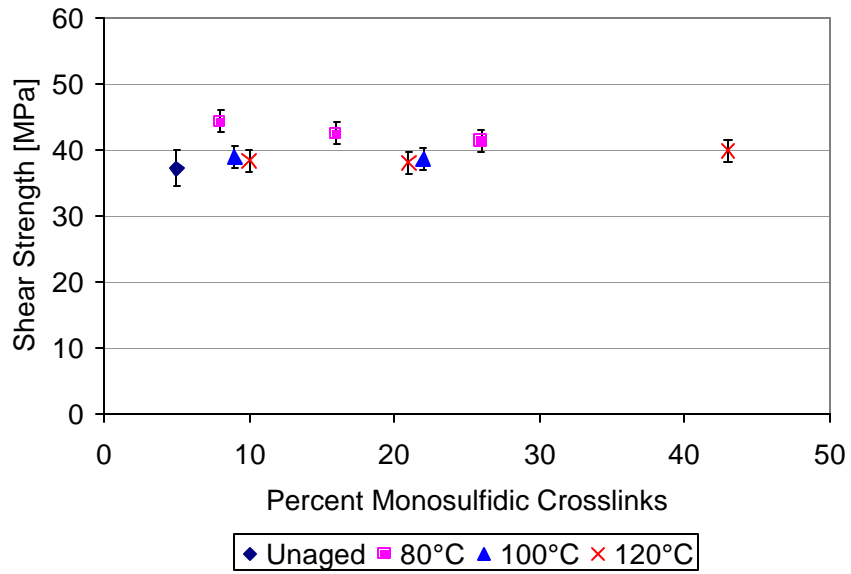
Figure 4-24 **Compound B shear strength versus the percentage of monosulfidic crosslinks. The error bars represent one standard deviation.**
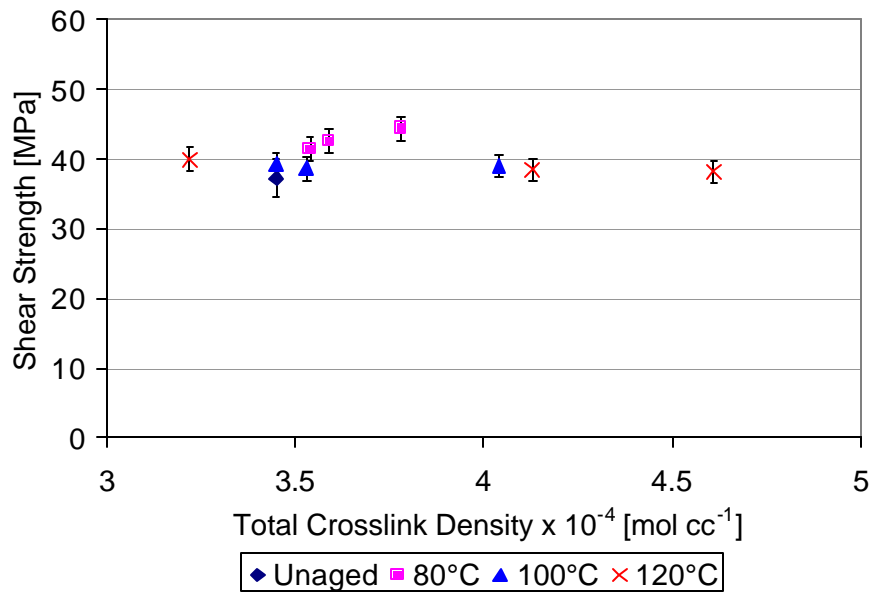
Figure 4-25   Compound B shear strength versus the total crosslink density. The error bars represent one standard deviation.

4.5   Summary

A good correlation between the quasi-static mechanical properties and the crosslink distribution exists. In agreement with the research of Nasir et al.[40], the higher levels of polysulfidic crosslinks generally correlate with the higher mechanical property values. Testing results for the both compounds showed a linear dependence of the ultimate stress, ultimate strain and modulus on the percentage of polysulfidic and monosulfidic crosslinks. The modulus of compound B displayed a linear trend with the percentage total crosslink distribution.   Compound A did not exhibit this linear correlation. This difference in the modulus behavior between compound A and compound B may be attributed to the difference in the size of carbon black filler. The larger area carbon black particles in compound A may limit the response of the natural rubber due to a higher volume fraction of filler.   There was no correlation between the shear strength and either the percentage of poly and monosulfidic crosslinks or the total crosslink density. Curve fits for all of the figures presented in the chapter are tabulated in

APPENDIX A.

The predictions of the mechanical performance of the compounds will be made using the master curves of Figure 3-2 and Figure 3-3 in conjunction with these correlations. These mechanical property values will be used in the life prediction of the 2-ply laminate. Research into how thermal aging and rubber reversion affects the dynamic mechanical properties will be presented in the following three chapters.

5.   FATIGUE LIFE

The previous chapters dealt with determining the effects of thermal degradation on both compounds. Application of the master curve to both compounds showed that the results were not singular and could be applied to the two different natural rubber vulcanizates. The analyses for the fatigue life and the crack propagation were applied solely to compound B. This reduction of the test matrix was performed because the 2-ply laminate is comprised solely of compound B.

5.1   R-Ratio Effect on Fatigue Life

Fatigue testing of R-ratios between zero and one were performed to see if the fatigue life of compound B demonstrates suppression of the mechano-oxidative crack growth, as well as to determine the R-ratio fatigue effect for the life prediction of the 2-ply laminate. As stated in the literature review the R-ratio affects the fatigue life of NR compounds that do not contain antiozonants[27-35]. This R-ratio effect was characterized as being the suppression of the mechano-oxidative crack growth when $R > 0$.

The fatigue tests were conducted at room temperature under load control at a frequency of 0.25 Hz using an Instron servo-hydraulic test frame fitted with a MTS 407 controller and gripped with MTS double roller tensile grips. The R-ratio was defined as the quotient of the minimum stress level divided by the maximum stress level. The results of the testing are plotted in Figure 5-1. In the data there was seen a strong R-ratio dependence. This dependence showed that increasing the R-ratio led to improved fatigue behavior. This trend was the same behavior that has been reported by Bathias et al[9]. Furthermore, there appeared to be a change of failure mechanism between R=0.1 and R=0.2. This change in failure mechanism is distinguished by the abrupt change in behavior. The R=0.1 fatigue behavior followed the same trend as the R=0; however, the R=0.2 fatigue behavior followed the rupture behavior, R=1.0. If a master curve were generated from Figure 5-1 this change in failure mechanism would appear as a discontinuity in either the master curve or the shift factor plot.
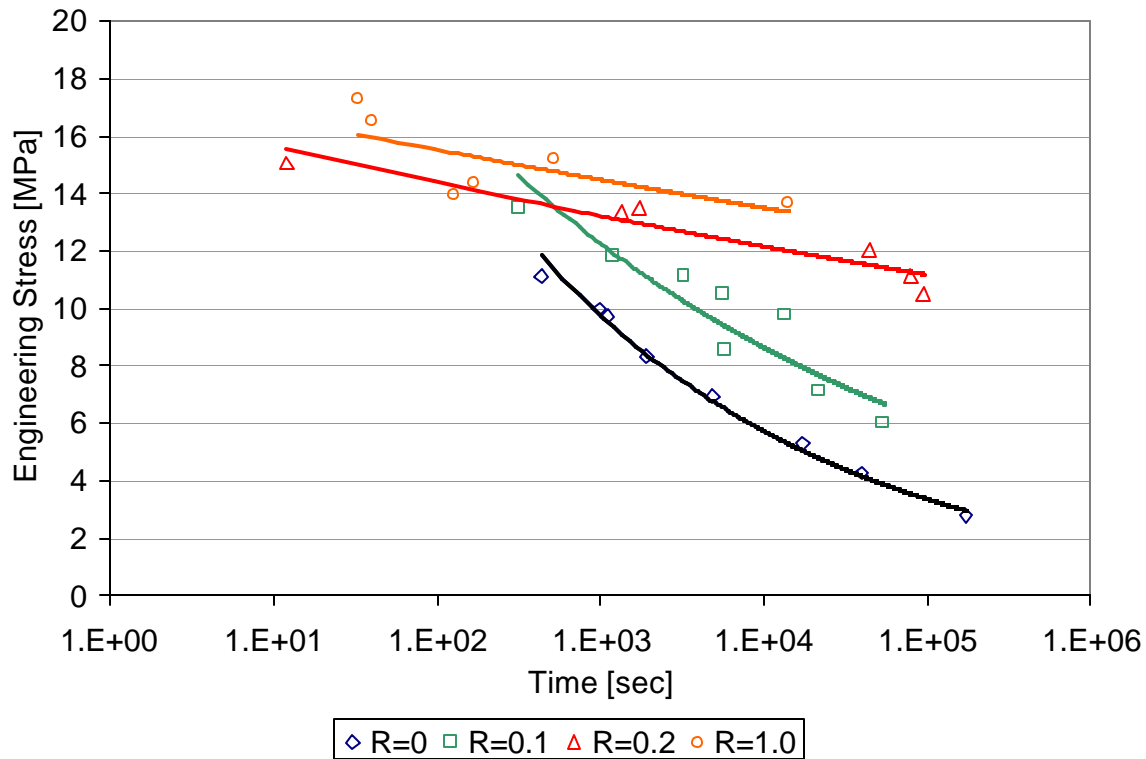
Figure 5-1   Fatigue life dependence upon R-ratio.

Without this change in the fatigue failure mechanism a plausible explanation for the R-ratio effect would have been strain induced crystallization[9]. Increasing the R-ratio would have served to increase the fatigue life while maintaining the same basic fatigue curve. However, the change in the failure mechanism begs for a different explanation. One plausible answer is given by the two-network model of Rivlin et al[16]. In the two-network model, rupture and recombination of crosslinks takes place upon the relaxation of the elastomer. A physical interpretation of this model is that the network chains are bound together in a knot. Variable tension fatigue provides the energy for the knot to become undone. As the knot becomes undone, the elastomer relaxes, a new network is created containing a different network configuration. The worst-case scenario is the fully relaxed case, R=0, where the network chains have the greatest opportunity to relax after the applied load. The new network based upon the strained state would lead to the lower time to failure. For the case of stress rupture, R=1, the original

network does not have the opportunity to relax and is most likely dominated by strain induced crystallization. The change in the failure mechanism of Figure 5-1 was probably the transition from domination by relaxation and creation of the new network to domination by strain induced crystallization.

5.2 Elevated Temperature Fatigue Life

Elevated temperature fatigue was carried out in order to examine the effect of temperature on the fatigue lifetime of compound B. The fatigue tests were conducted at a R-ratio of zero, under load control at a frequency of 0.25 Hz using an Instron servo-hydraulic test frame fitted with a MTS 407 controller and gripped with MTS double roller tensile grips. ASTM D412-D samples of compound B were tested in load control at 60 and 90°C. Elevated temperature was obtained with a feedback-controlled forced convection chamber, Figure 5-2. The elevated temperature fatigue results for compound B are plotted in Figure 5-3. The results were as expected with the fatigue life decreasing with increasing testing temperature. For these tests it was assumed that no significant thermal aging occurring during the life of the test. The failures were dominated by the cyclic damage at the elevated temperature.

Figure 5-2   Elevated temperature fatigue testing arrangement.
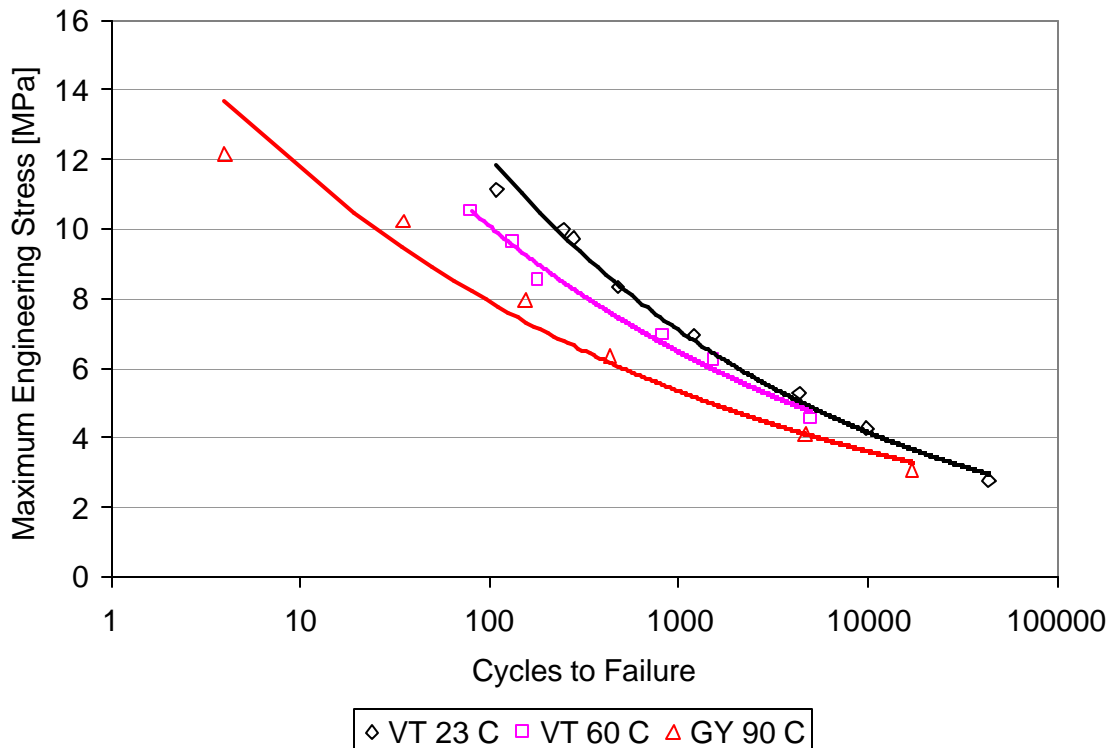
Figure 5-3   Compound B fatigue life dependence on temperature.

5.3   Thermal Aging Effect on Fatigue Life

Fatigue testing was conducted on the aged compounds to see the effect of thermal aging on fatigue life. The fatigue tests were conducted at room temperature under a R-ratio of zero in load control at a frequency of 0.25 Hz using an Instron servo-hydraulic test frame fitted with a MTS 407 controller and gripped with MTS double roller tensile grips. Only the 12 day at 120°C aged compound was tested. The results of the testing are presented in Figure 5-4. As seen in the figure there was a distinct thermal aging effect on the fatigue life. This result of the testing was the opposite of the observations of Blackman et al.[39], that fatigue life was not necessarily a function of the crosslink type distribution. Aging for 12 day at 120°C reduced the percentage of polysulfidic crosslinks from 70 to 28 percent. Thus it would seem reasonable to state that the crosslink distribution does contribute to the fatigue life of the vulcanizate.

The effect of thermal aging on the fatigue life is similar to the effect of temperature. In both the thermal and the aged fatigue data the number of cycles to failure converge for low stress levels. This asymptotic stress value is approximately 3 MPa.
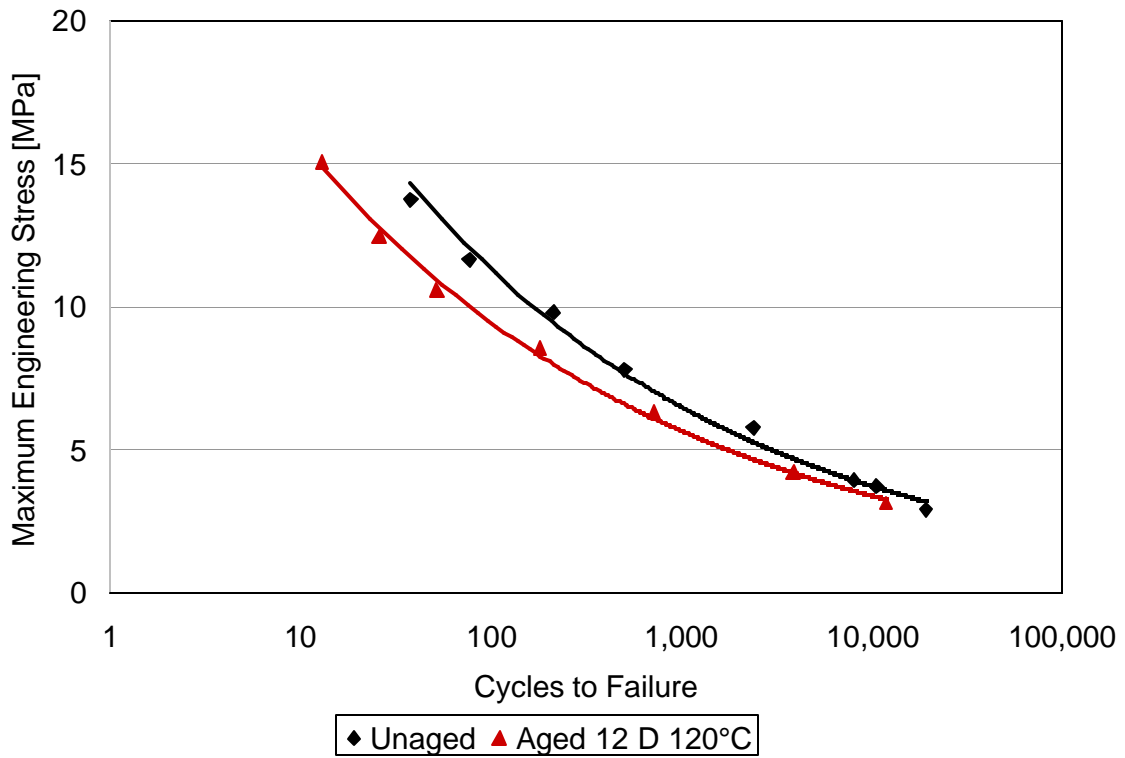
Figure 5-4   Effect of thermal aging on fatigue life.

6.   CRACK PROPAGATION

Crack propagation have been studied using a double cantilever beam specimen. This specimen was a modification of that described by Lefebvre et al[11]. To the authors knowledge this was the first time this type of specimen has been applied for the study of crack propagation in NR vulcanizates. A unique aspect of this specimen design was that it allowed for crack propagation under plane strain rather than plane stress conditions. The majority of the research in the literature concerning crack propagation in NR has been on single edge crack specimens, which exhibit a condition of plane stress[1-8,12-14,16-19]. As with the investigation into the fatigue behavior, the crack propagation portion of this research only investigated compound B.

6.1   Double Cantilever Beam

The basic design of the DCB test is presented in Figure 6-1. The rationale for applying a DCB to study crack propagation was to have two stiff rigid adherends with a highly compliant adhesive between them. The adherends were to mimic the structural belts of a tire while the adhesive was the tire compound. The generalized structural design of a tire including the belt package was presented in Figure 2-1. The beams were 26.67 cm in length, 2.54 cm wide with 1.27 cm thick adherends. The elastomer was one hundred percent natural rubber with a carbon black filler level of 65 parts per hundred parts rubber by weight. Prior to lay-up inside the DCB specimens, the elastomer was milled to a thickness of 2 mm. The elastomer was then vulcanized inside the beam in a hot press for 27 minutes at 150°C. A 0.635 cm hole was drilled through the sides of the beam so that the beams could rotate about a pin. The pin was used so that the bending moment about the end of the beam due to loading could be minimized.

Tests were performed in quasi-static displacement controlled conditions and in load controlled fatigue test using an Instron servo-hydraulic test frame fitted with a MTS 407 controller and gripped

with MTS hydraulic grips. A pre-crack was inserted into the middle of the compound and load was applied. This test was a mode I opening crack growth test. Brass and aluminum were chosen as the adherends for the DCB test. Brass was chosen so as to mimic the brass coated steel cords of the structural belts of a truck tire and to reduce the chance of an adhesive failure. Aluminum was chosen to see if the thick aluminum oxide layer that forms on the bar would lead to an adhesive rather than a cohesive failure. After initial testing it was found that aluminum adherends did not produce an adhesive failure. From this result, for the majority of the remaining tests aluminum was used at the adherend because it offered a reduced cost in the bar stock price. Some brass DCB specimens were tested in order to use up the bar stock that was initially purchased.

1.27 cm

26.67 cm
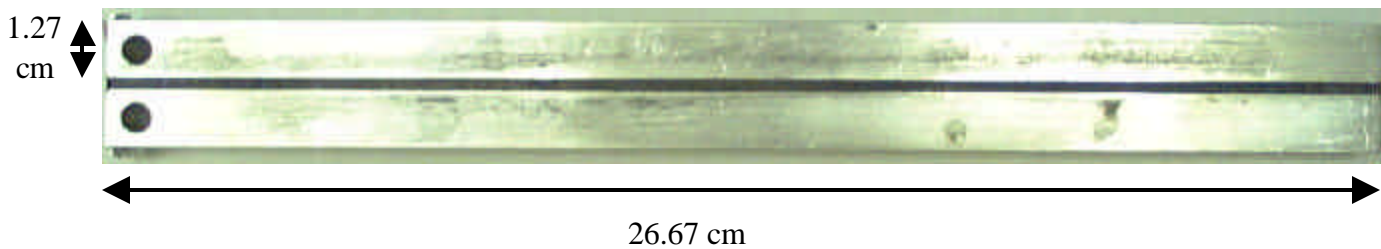
Figure 6-1   Design of the DCB test.

6.1.1   Quasi-Static DCB Testing

Quasi-static tests were performed on the DCB specimens in both displacement and load control conditions. The load-controlled test produced a catastrophic failure, where once the first crack propagated the sample continued to fail as the machine tried to increase the load to the prescribed set point. Displacement controlled tests produced much more usable results. The tests were run at a displacement rate of 5.08×10^{-6} m sec^{-1}. A typical load versus displacement profile for a displacement controlled DCB test is shown in Figure 6-2. The failures in displacement control were a stick-slip type failure, where once the sample possessed sufficient fracture energy the crack propagated. The crack arrested once the driving fracture energy had been expended in crack growth.
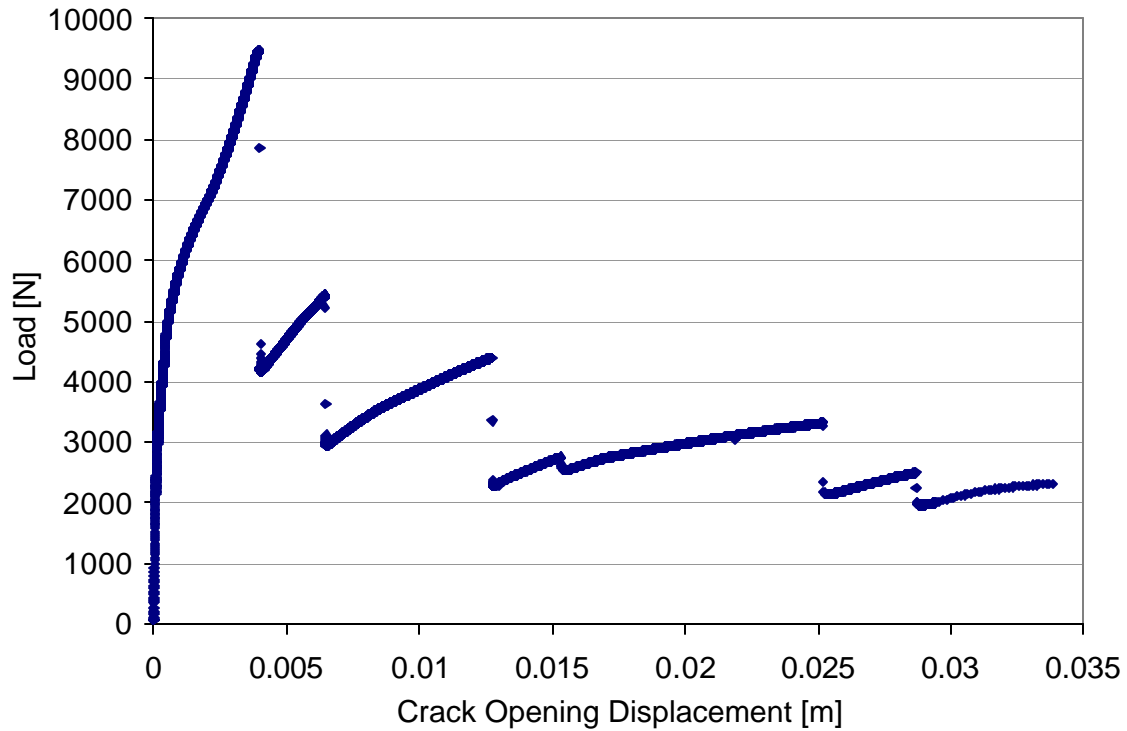
Figure 6-2   Typical load versus displacement profile for a displacement controlled DCB test. Sample contained a pre-crack of 1.75 mm

The strain energy release rate was calculated from the experimental data using the Griffith equation:

$$G = \frac{P^2}{2}\left(\frac{\partial C}{\partial a}\right)_l \qquad [6.1]$$

Where P is the applied load, a is the crack length, C is the experimental compliance and l is the displacement. Given the slow displacement of the test the constant displacement condition of equation 6.1 was assumed to have been met. The crack length was measured from the failed sample. The failure surface showed very clearly a stick-slip behavior of the crack propagation. Figure 6-3 shows this stick-slip behavior as well as the cohesive failure of the DCB specimen. The calculated strain energy release rate is shown in Figure 6-4 for the first four crack jumps of an aluminum sample. The strain energy

release rate range of 15 to 20 kJ m^{-2} was in the range of values that has been measured for compound B by other test methods[74].

Figure 6-3 **Failure of a displacement controlled DCB sample. The photos show the stick slip behavior as well as the cohesive nature of the failure.**
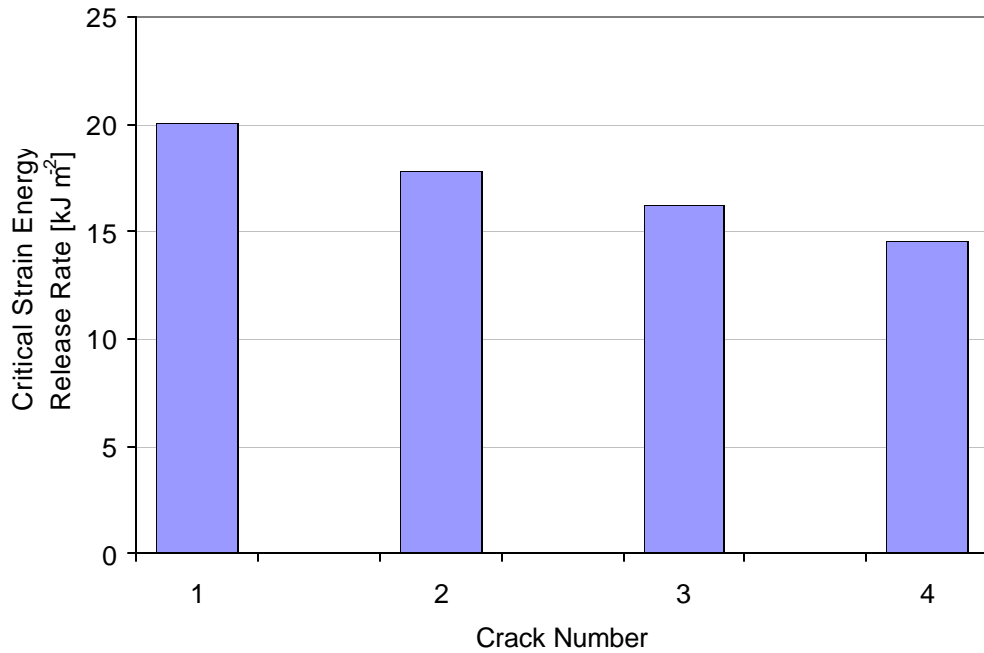
Figure 6-4 **Experimentally determined critical strain energy release rate for the first four cracks of a DCB sample.**

6.1.2 Single Edge Notch Testing

Single edge notch testing was performed in order to compare the crack growth rate results with those obtained from the DCB specimens. Rectangular specimens were cut from 2 mm thick sheets of the elastomer after undergoing the same cure of 27 minutes at 150°C in a hot press. A notch was inserted into one edge of the specimen using an exacto knife. The specimens were fatigued in load control under the following conditions: R-ratio = 0.0, frequency = 0.25 Hz. The crack length was measured during fatigue using a micrometer and the number of cycles to that crack length was recorded. The strain energy release rate, tearing energy, was calculated using equation 1.1.

6.1.3 Fatigue of DCB Specimens

Fatigue of the DCB specimens was conducted in order to obtain a da/dn versus ΔG curve. Following the literature data [3-7], it was expected that this curve would follow a Paris law trend and be fit by a generic equation of the form:

$$\frac{da}{dN} = a(\Delta G)^b \qquad [6.2]$$

Initial fatigue testing was carried out for numerous samples at different maximum loads all with an R-ratio of zero. A pre-crack was inserted in the center of the compound layer with an exacto knife. Initial testing began with the fatigue crack growth beginning directly from this pre-crack; however, it was found that the subsequent crack growth was heavily dependent upon the sharpness of the pre-crack. A new approach was developed where the pre-crack was placed in the compound and then the sample was loaded under displacement control until the crack propagated. Essentially, the first crack jump of a quasi-static DCB test was reproduced. By allowing the crack to propagate the crack tip became self-aligned and a natural pre-crack existed. From this initial testing it was determined that the following testing parameters yielded a reproducible environment:

- R-ratio $= 0.0$

- Frequency $= 2$ Hz

- $P_{max} = 2224$ N

- Testing performed at room temperature

This value of maximum load yielded from one to two decades of strain energy release rate, ΔG. Lower values of maximum load would have yielded a wider range of ΔG; however, the increased testing time at lower load did not make such testing efficient. The strain energy release rate was calculated from the experimental data using the modified Griffith relation of equation 6.1.

The crack length at a given number of cycles was measured by profiling the depth of the debond during fatigue loading. A 0.254 mm and a 0.0508 mm profiling tool was inserted into the crack and the depth of penetration was noted on the tool. The crack length was then measured from the profiling tool using a micrometer and the number of cycles to that crack length was recorded. Figure 6-5 shows the smooth instantaneous crack growth that occurs under the displacement controlled test as well as the load controlled fatigue crack growth surface. For all tests crack growth was a cohesive failure.

Pre-Crack   Stick-Slip Crack Growth   Fatigue Crack Growth
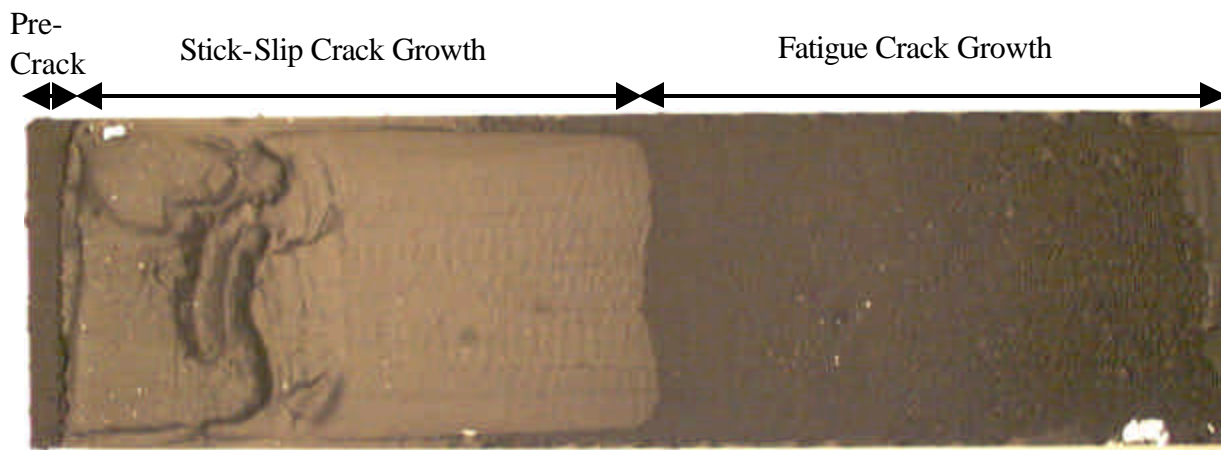
Figure 6-5   Failure surface of a DCB sample showing the pre-crack, stick-slip crack growth under displacement control and the fatigue crack growth. The plane strain planar crack growth and the plane stress condition along the specimen edge can be seen.

The experimentally obtained crack growth rate as a function of the change in the strain energy release rate for the DCB test is shown in Figure 6-6. Included in the figure is the crack growth rate vs. ΔG data for the single edge notch test. As expected for crack growth data of NR compounds, there was significant scatter in the data. The significant aspect of this data was its difference when compared to the single edge crack data. For the same value of ΔG the crack growth rate was two orders of magnitude higher. It was inferred from the data that cracks grow faster under a state of plane strain rather than plane stress. This hypothesis was verified through inspection of Figure 6-5. The interior of

the DCB specimen was dominated by plane strain; however, due to the Poisson effect the edge of the compound was controlled by plane stress.
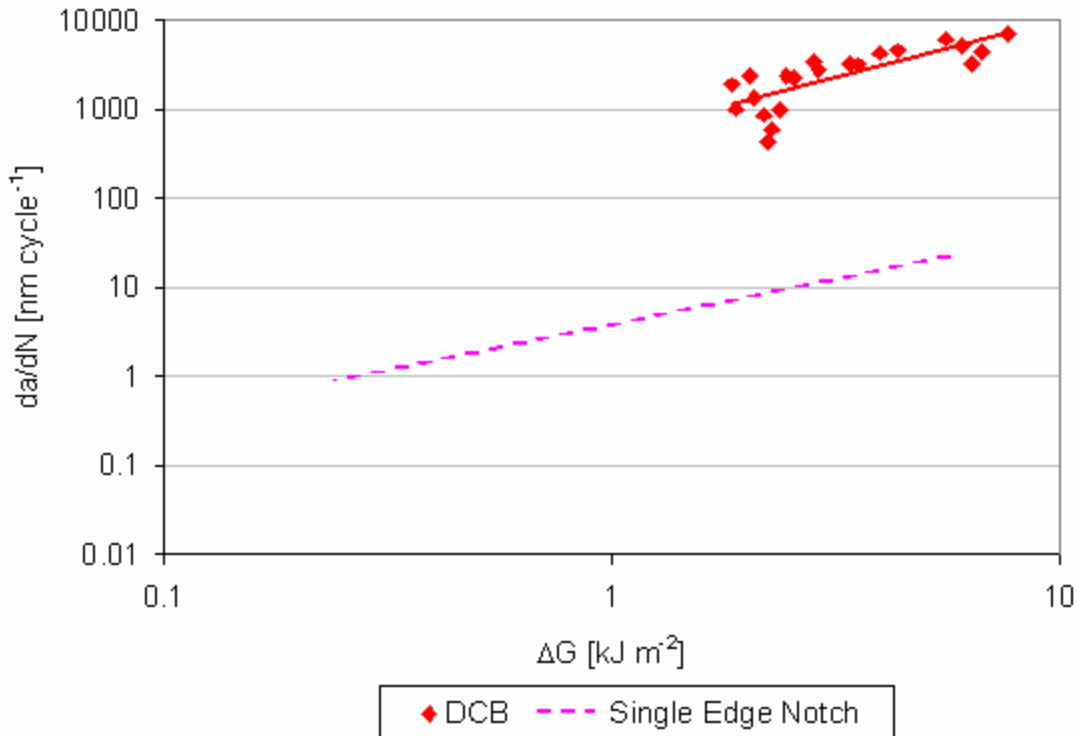
Figure 6-6   Crack growth rate versus the change in strain energy release rate.

6.2   DCB Verification

Thus far the discussion on the double cantilever beam has been focused on its applicability as a test specimen. Now the discussion must focus on the verification of the DCB as a test specimen with regards to its behavior as predicted by mechanics. In the case of a beam on a rigid foundation the compliance is based on the relationship

$$C = \frac{8a^3}{Ebh^3}$$
[6.3]

Where *a* is the crack length, *E* is the modulus of the adherend, *b* is the specimen width and *h* is the thickness of each adherend. From this simple solution the compliance of the beam is expected to increase with the third power of the crack length. This relationship between the compliance and the crack length is shown in Figure 6-7 for three different unaged DCB specimens. As can be seen the compliance did indeed increase as the third power of the crack length. The difference between the three specimens was the initial crack length.
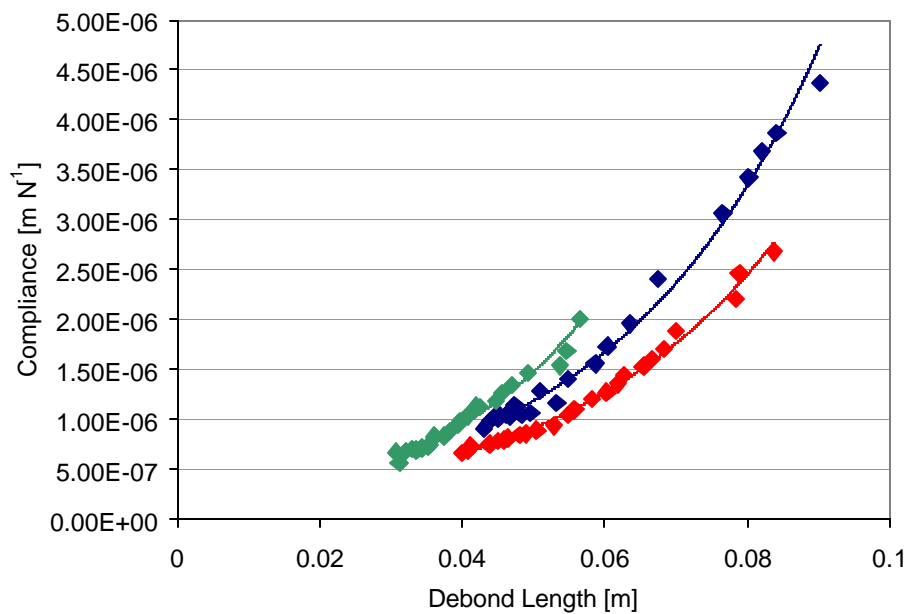
Figure 6-7 **Compliance versus fatigue cycles for three different DCB specimens.**

The beam on a rigid foundation relationship for the compliance can be rewritten and linearized as:

$$C^{\frac{1}{3}} = \sqrt[3]{\frac{8a^3}{Ebh^3}}$$ [6.4]

The results of equation 6.4 are plotted in Figure 6-8. The compliances for the three different samples were linear functions with the crack length; however, they did not pass through zero. The compliance of the system should be zero when the crack length is zero. This additional compliance was partly due to

plasticity in the adherends. The beam on a rigid foundation is based upon linear elastic fracture mechanics, which allows for plastic deformation in the crack tip zone but not in the adherends. To adjust for this additional plasticity two calibration methods were applied [75,76]. The methods were the crack length calibration method and a compliance calibration method.
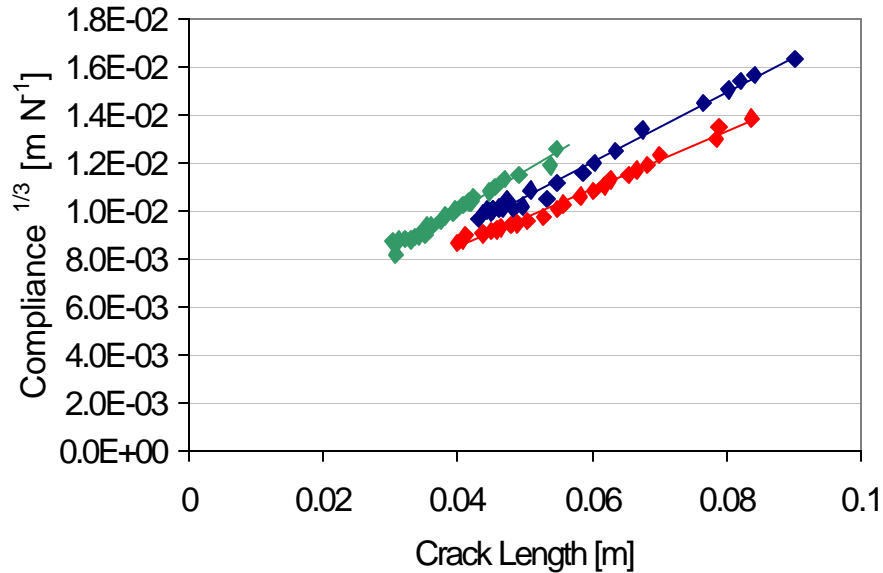
Figure 6-8   Linearized beam on a rigid foundation model.

The crack length calibration method[75] is based upon modified beam theory. The modified equation for the strain energy is given by:

$$G = \frac{3P^2}{2b} m^3 (a + x)^2 \qquad [6.5]$$

where m is the slope of the compliance to the one third versus crack length line, Figure 6-8. The compliance calibration method[76] is given by the following equation:

$$G = \frac{m_2 P\Delta}{2ba} \qquad [6.6]$$

where m_2 is the slope of the log compliances versus log crack length plot, and Δ is the crack opening displacement. The results of the calibration calculations for both methods are plotted against the raw

97

DCB data as well as data from a single edge notch test in Figure 6-9. The calibration from both methods yielded similar values of G. The slope of the Paris-Law fit was approximately the same for both the experimental values of ΔG and the values obtained after the calibration. The trend that cracks under plane strain grow 100 times faster than cracks under plane stress was conserved. The crack length calibration method will be applied for the calculation of the DCB ΔG values for the remainder of this dissertation.
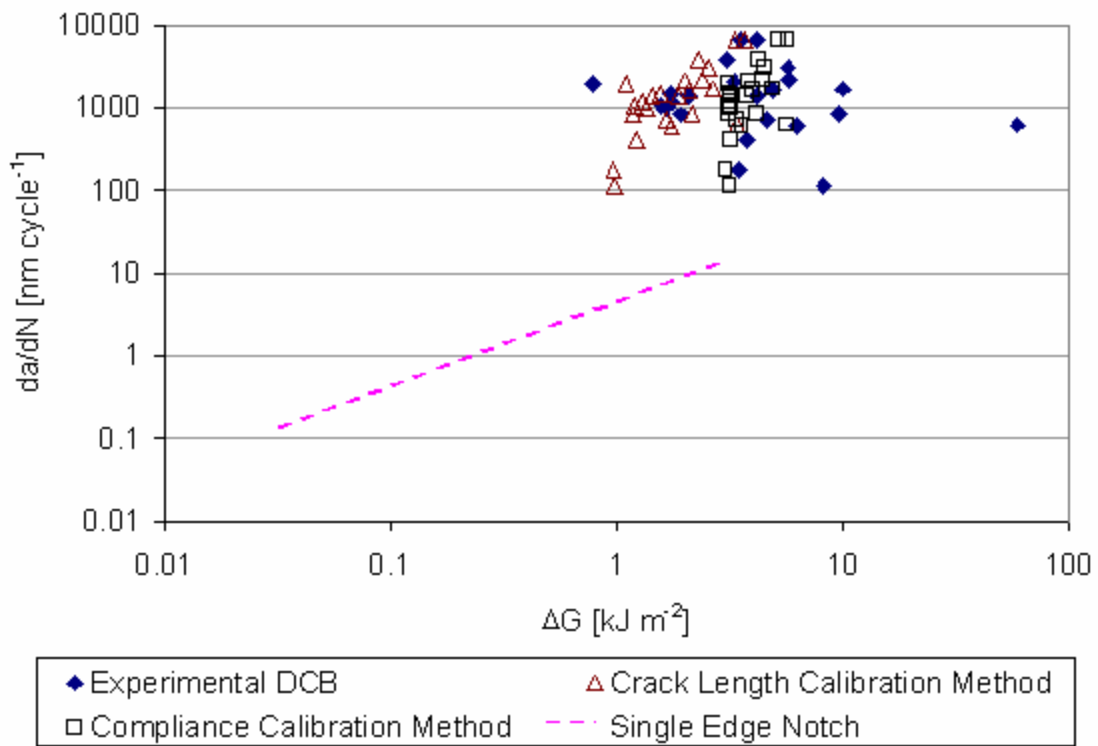
Figure 6-9   Crack growth rate versus the change in strain energy release rate for the experimental DCB, single edge notch and the crack length calibration and compliance calibration method.

While the beam on a rigid foundation model predicts the behavior of the DCB, it was assumed that the assumption of a rigid foundation was not applicable in the case being investigated. Figure 6-10 presents a comparison of the compliance versus crack length for the experimental and the rigid

foundation models. As can be seen the rigid foundation greatly underestimates the compliance of the system. An improved approximation for the compliance was required. To establish this approximation, Lefebvre et al.[11] assumed that the thin rubber layer acted as a classical elastic foundation, Figure 6-11. They developed a closed-form solution based on the finite length beam on an elastic foundation solution given by Hetenyi. In their approach the total beam deflection at the loading point B, was given by:

$$y_B = y_A + q_A \cdot a + \frac{Pa^3}{3EI} \qquad [6.7]$$

The slope, θ, and the deflection, y, at a point A, corresponding to the crack length, could be calculated using Hetenyi's solution for a finite beam on an elastic foundation. In the case of equal applied forces on both beams, symmetry required that there be no horizontal frictional forces and that the failure modes be solely mode I. The error arising from the nonsymmetry due to the rubber remaining on the adherend was negligible. The applied force at point B was translated to the crack length at Point A and an equivalent moment was also applied at point A. The governing differential equation for a beam on an elastic foundation was:

$$\lambda = \sqrt[4]{\frac{k}{4EI}} \qquad [6.8]$$

where k was the foundation stiffness and I was the area moment of inertia of the cross-section. For beams of finite length, equation 6.8 depended on the nondimensional quantity λ(L-a). In the case of the DCB specimens, this quantity exceeds π and may be classified as a long finite length beam. For an applied force P at point A, the slope and deflection at A were given by:

$$q_A = \frac{2P\lambda^2}{k} \frac{Sinh^2\lambda\zeta + Sin^2\lambda\zeta}{Sinh^2\lambda\zeta - Sin^2\lambda\zeta} \qquad [6.9]$$

$$y_A = \frac{2P\lambda}{k} \frac{Sin\lambda\zeta Cos\lambda\zeta - Sin\lambda\zeta Cos\lambda\zeta}{Sinh^2\lambda\zeta - Sin^2\lambda\zeta} \qquad [6.10]$$

where $\zeta = L - a$. For an applied moment of Pa at point A, the slope and deflection were given by:

$$q_A = \frac{4Pa\lambda^3}{k} \frac{Sin\lambda\zeta Cos\lambda\zeta + Sin\lambda\zeta Cos\lambda\zeta}{Sinh^2\lambda\zeta - Sin^2\lambda\zeta} \qquad [6.11]$$

99

$$y_A = \frac{2Pa l^2}{k} \frac{Sinh^2 l V + Sin^2 l V}{Sinh^2 l V - Sin^2 l V}$$

[6.12]

The closed form solution for the total deflection of the DCB specimen was obtained by superimposing the results of equations 6.9 – 6.10 and substituting them into equation 6.8. The compliance was simply calculated as the deflection divided by the load. The fit of the elastic foundation model to the experimental compliance data is presented in Figure 6-10.
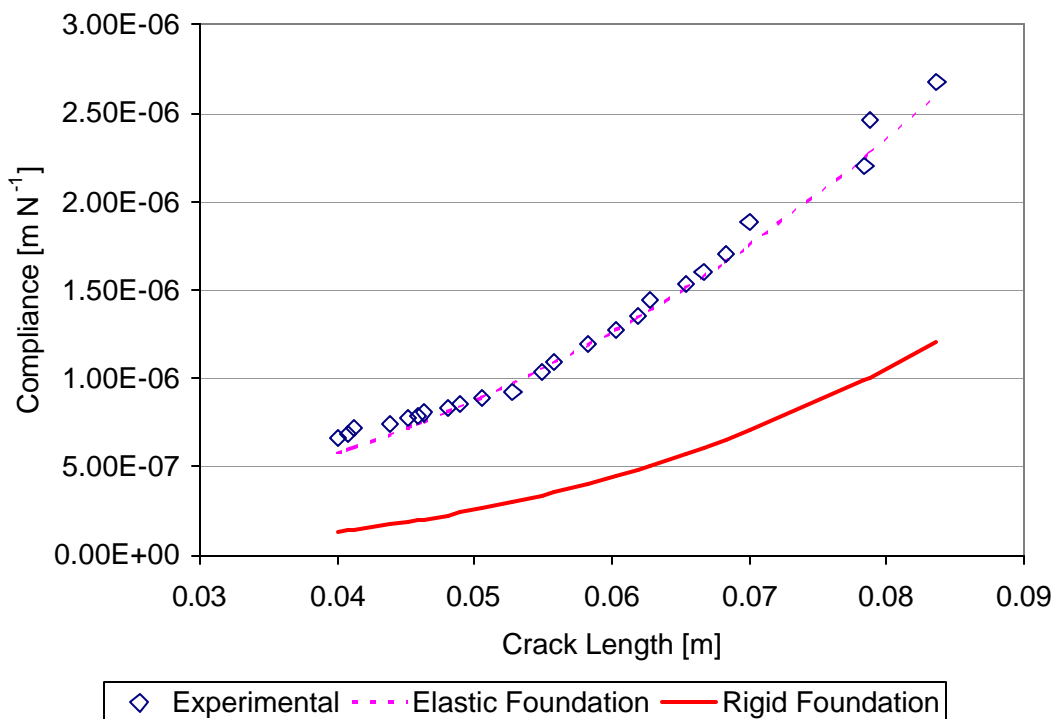
Figure 6-10   Comparison of double cantilever beam data to the beam on an elastic foundation and beam on a rigid foundation models.
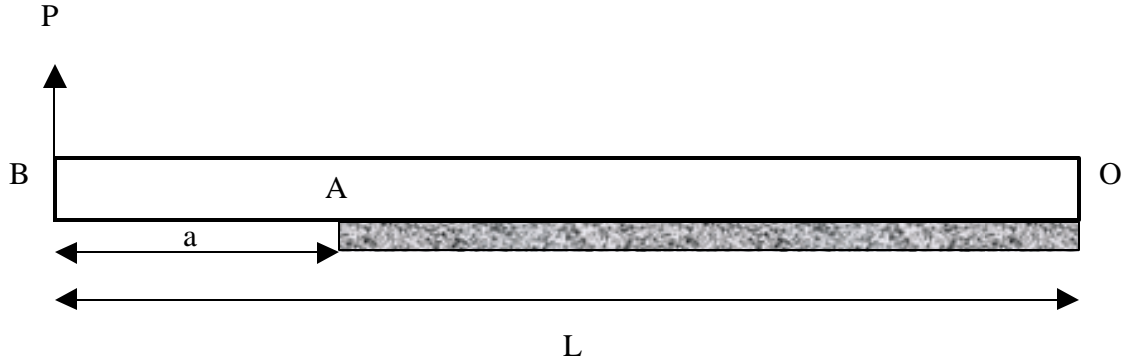
Figure 6-11   Upper half of a DCB specimen modeled as a beam on an elastic foundation.

The elastic foundation model was fit by varying the foundation stiffness. Essentially the foundation stiffness was used as a fitting parameter for the model. The stiffness can be predicted analytically using a procedure developed by Gent et al[77,78]. In their procedure the stiffness was determined from the equation:

$$k = 2\left(\frac{4}{3} + \frac{b^2}{3t^2}\right)E \qquad\qquad [6.13]$$

It was found that the prediction from equation 6.13 was substantially lower than the experimental values. Similar results were reported by Lefebvre et al[11].   In the work of Gent et al.[77,78], they attributed the differences between the analytical solution and the experimental fitting of the foundation stiffness to be due to the solution accounting for the end occurring at the debond tip and the fact that their analytical solution does not account for the damped sinusoidal displacement. Both of these factors resulted in an overprediction of the foundation stiffness.

If the data for neoprene rubber of Lebevre et al.[11] is combined with the natural rubber data, the effect of rubber thickness upon the deviation of the experimental from the analytical foundation stiffness can be seen. This effect is plotted in Figure 6-12. In the figure it can be seen that the agreement between the experimental and the analytical values for the foundation stiffness are strong functions of the rubber thickness. Assuming that the combination of the neoprene and the natural rubber data was

101

acceptable, then the ideal thickness to have agreement between the experimental and the predicted values of the foundation stiffness would be 0.87 mm.
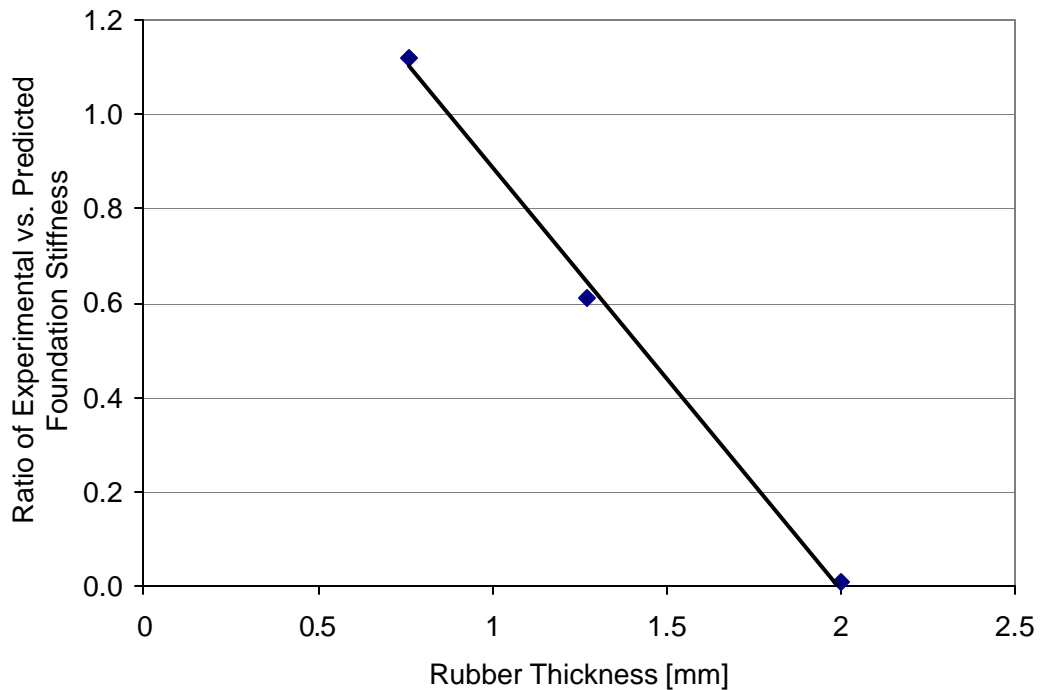
Figure 6-12   Ratio of the experimental versus the predicted foundation stiffnesses as functions of the rubber thickness.

Despite the differences between the experimental and analytical values for the foundation stiffness, the DCB was a valid specimen based upon the mechanics. In order to fully be confident in the validity of the specimen the potential for cavitation at the crack front within the rubber was investigated.

6.3   Cavitation at the Crack Front

In the literature review it was stated that Gent et al.[22] found that a thin long block was likely to undergo internal cavitation prior to achieving sufficient fracture energy to propagate a crack inwards. This cavitation would be a result of the hydrostatic tension generated inside the rubber due to the applied load. Bathias et al.[9] has reported cavitation occurring inside a NR pancake specimen that has

been subjected to static and cyclic presure. The development of this cavitation was attributed to high hydrostatic tension within the specimen. In light of these findings, investigations into whether or not cavitation occurs within the beams were performed.

Gent et al.[22] generated their analysis based upon the assumption that thin bonded rubber blocks subjected to tilting exhibited an linearly elastic response. This was a simplification for the case of rubber compounds. For the case of a long thin block subjected to tilting they developed an equation to calculate the maximum value of the strain energy for which cavitation would not occur. This equation is:

$$G = aE \frac{1}{6} \left(\frac{P_m}{E} \right)^2 \frac{h^5}{ab^4} \left(1 + \left(\frac{b}{h} \right)^2 \right) \qquad [6.14]$$

Where a is the beam length, b is the beam width, h is the beam thickness, P_m is the maximum attainable hydrostatic pressure without causing cavitation and E is the elastic modulus of the rubber. Gent et al. assumed that the maximum acceptable value of $\frac{P_m}{E}$ is unity. Inserting the values from the DCB testing assuming a nominal modulus value of 5.8 MPa the maximum value attainable value of the strain energy release rate was calculated to be 50 Jm^{-2}. This value was much less than the 20 to 15 kJm^{-2} values that were experimentally determined, Figure 6-4. From this analysis it would appear that all the strain energy values from the quasi-static tests were in error. To determine if cavitation was occurring the failure surfaces of the DCB specimens were examined and compared with those reported by Gent et al[79]. Figure 6-13 presents an image of cavitation inside a cylindrical test piece after application of a large tensile load. The cavitations were spherical in nature. Figure 6-14 shows the failure surface of the DCB specimen from which the strain energy release rates values of Figure 6-4 were calculated. There was no discernable cavitation. The failure surface did not demonstrate spherical failure features similar to the cavitation in Figure 6-13. It appeared that cavitation was not occurring during the quasi-static crack growth. To investigate the fatigue growth, field emission scanning electron microscopy has been used to view the region of Figure 6-5 where quasi-static crack growth ended and fatigue crack growth began. An image of this region is shown in Figure 6-15. At the 100x magnification no spherical cavitation was discernable.
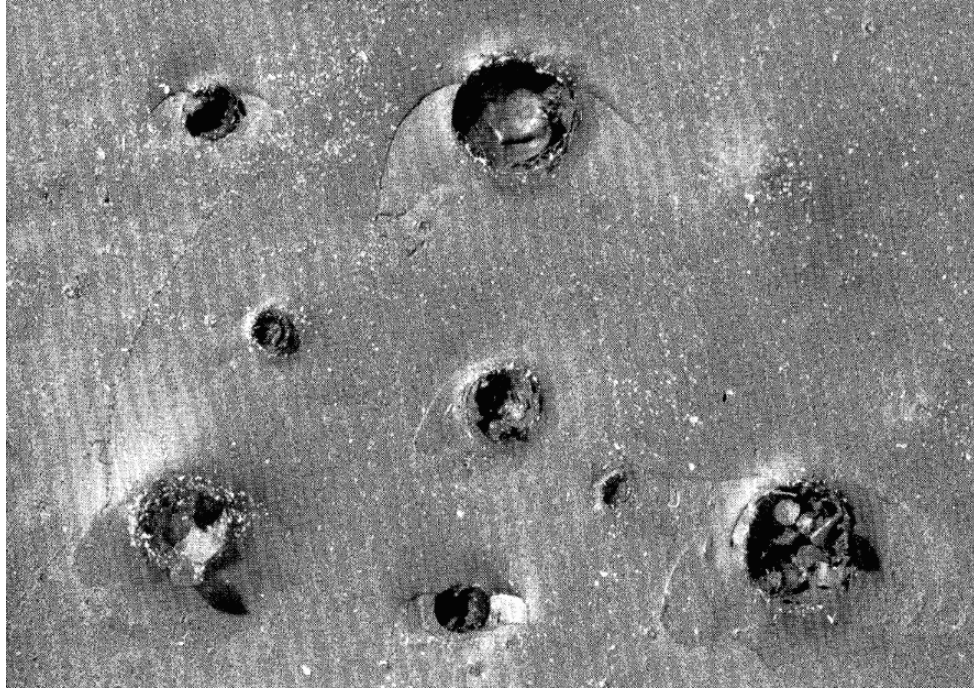
Figure 6-13 Cavitation inside a carbon black filled vulcanizate after application of a large tensile load. The magnification is 13x[79].

Figure 6-14 Failure surface of a displacement controlled DCB test. The first four stick-slip crack jumps can be seen. No cavitation is discernable. The magnification is 1x.
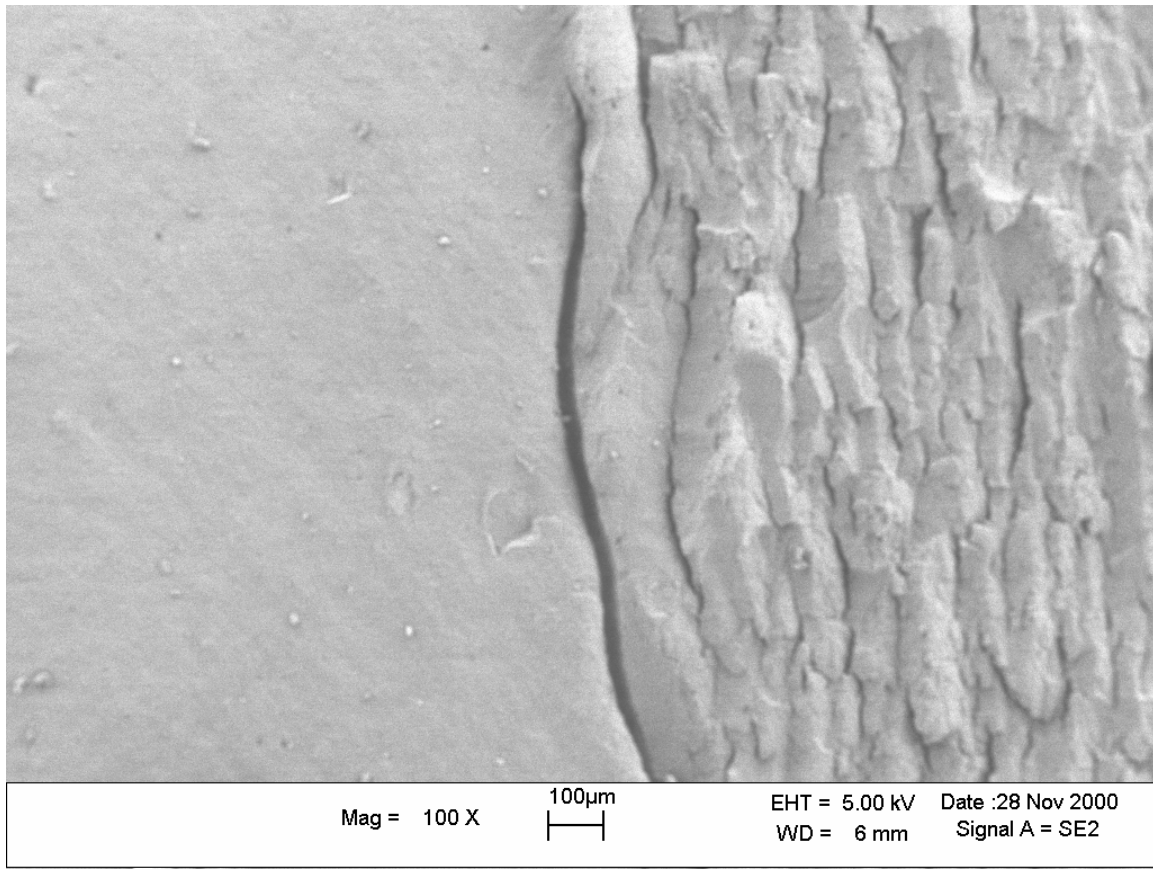
Figure 6-15   FESEM image of the transition between quasi-static crack growth and fatigue crack growth. No cavitation of the rubber is discernable.

Thus it appeared that cavitation did not occur within the DCB specimen. The error in the predicted maximum values of the strain energy may lie in the linear elastic assumption that was applied to the model. Conversations with Dr. Gent have revealed another possible answer to account for this error, which is due the fast speed at which the cracks propagate[80]. Under such high speed, near instantaneous, conditions the rubber may effectively be much harder and less likely to cavitate before or during fracture.

6.4   Molecular Orientation

Prior to vulcanization within the DCB specimens, compound B was prepared to the desired thickness by milling. The sheeted stock was milled down to the thickness of 2 mm using an industrial

rubber mill. It is proposed that an orientation of the flowing uncured polymer network may occur during this milling. To support this hypothesis quasi-static testing of aged samples in both the mill and transverse direction has been performed. Figure 6-16 shows the direction dependence of the energy density at break for compound B aged at 80°C for 3, 6 and 12 days. The error bars represent two standard deviations for each measure. In the unaged condition, the energy for both directions was statistically equal, but as the aging occurs the difference between the mill and transverse direction increased.

This reduction in energy may have occurred because some orientation of the polymer chains occurred during the milling process. As thermal aging proceeds the crosslinks between the chains were lost due to rubber reversion. This loss of crosslinks had less of an effect in the direction of the chains than perpendicular to them. Consequently, the energy density at break in the mill direction should be greater than then energy density at break in the transverse. Given that the mill direction demonstrated the highest energy density at break it was expected that the mill direction would demonstrate slower crack growth that the transverse direction for the same level of ΔG.

To investigate this possible effect on crack growth, DCB specimens were prepared with the mill and transverse directions along the length of the specimen. From examination of Figure 6-16 the aging condition of 6 days at 100°C was chosen. This condition appeared to have the greatest difference in the energy at break between the mill and the transverse direction. The test matrix consisted of two test specimens for the unaged mill and transverse directions and three test specimens for the 6 days at 100°C thermally aged mill and transverse direction specimens. The results of these molecular orientation tests are presented in Figure 6-17. The crack length calibration method, equation 6.5, was applied to calculate the values of the strain energy release rate, ΔG.
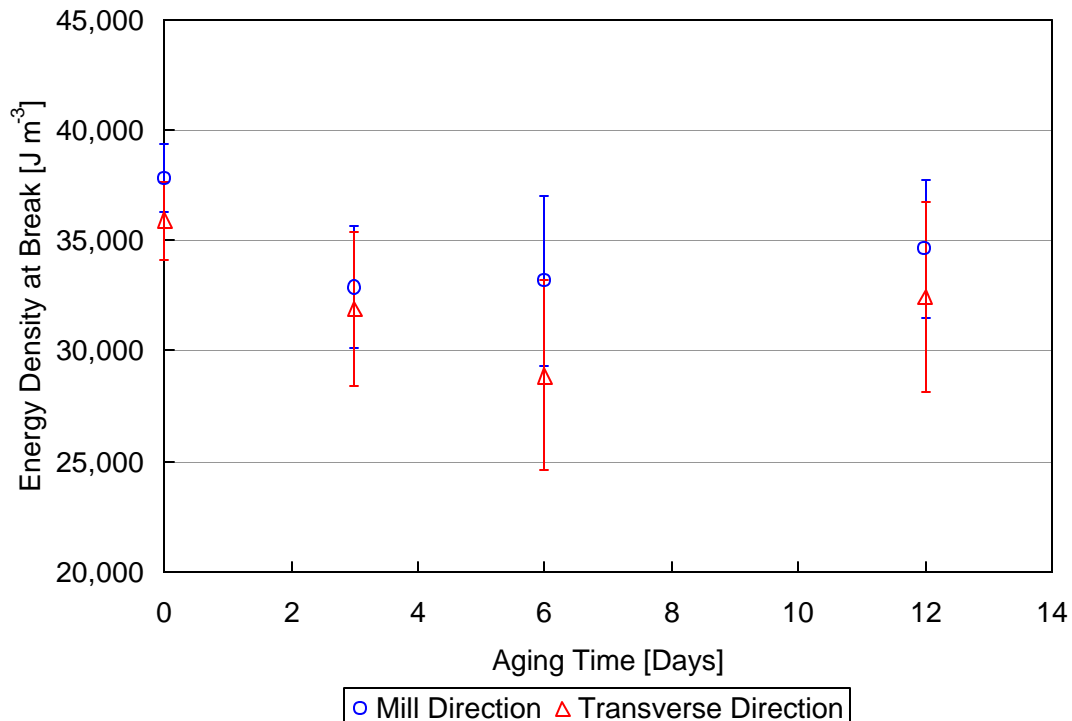
Figure 6-16 Dependence of energy density at break for the mill and transverse directions. The data is for compound B aged at 80°C. The error bars represent two standard deviations for the respective measure.

Through inspection of Figure 6-17 there appeared to be little difference in the crack growth rates between the aged mill and the transverse directions. This difference in the crack growth rates was not significant. A linear regression analysis revealed that the difference in the Paris Law fitting parameters, α and β, was not significant with p=0.095. Thus it appeared that the effect of the molecular orientation did not have a significant effect upon the crack growth rates. This result was encouraging, as the orientation on all of the DCB specimens, except for those specific specimens for the investigation into the molecular orientation, was not known. The effect of thermal aging on the crack growth rates is investigated in the next section.
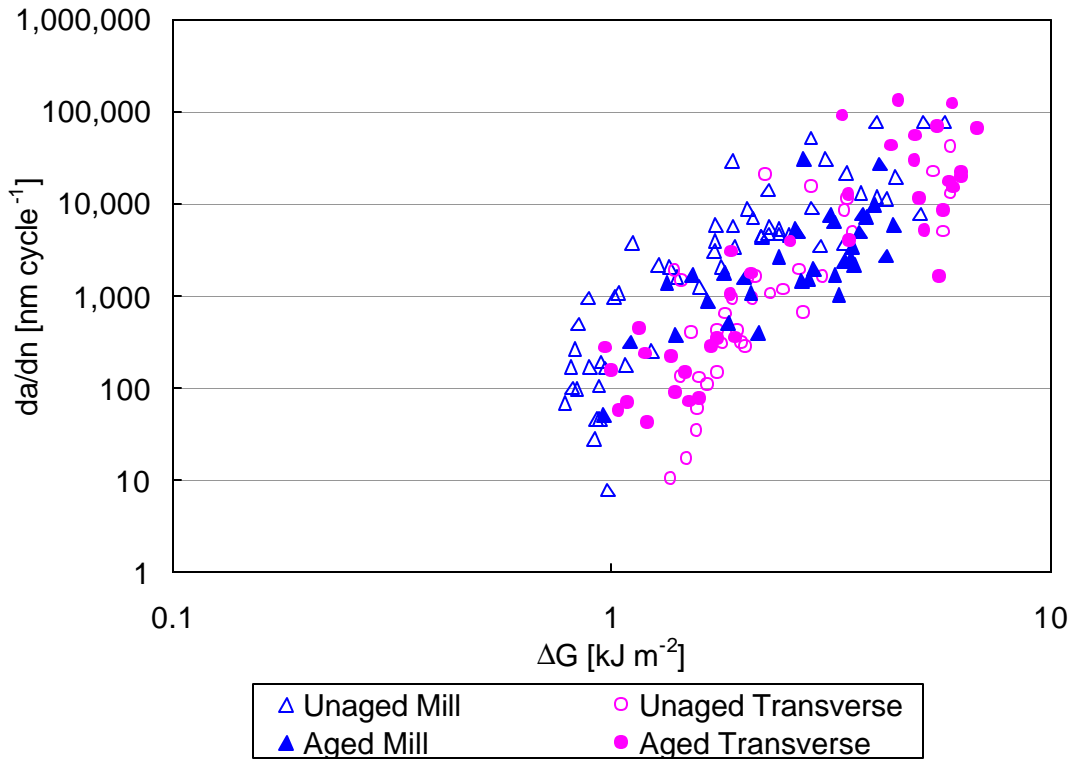
Figure 6-17   Aged and unaged crack growth rates in the mill and transverse direction.

6.5   Thermal Aging Effects On Crack Propagation

The concept that thermal aging of a natural rubber compound affects the mechanical properties of the compound has been applied to crack propagation. As shown in Figure 6-16, the energy density at break was a function of the aging time. Given that the crack propagation rate is proportional to energy via the Paris-law equation, it is proposed that a difference in the crack growth rate will be seen with isothermal anaerobic aging. In order to examine the affects of thermal aging upon the fatigue crack growth rates of natural rubber, an aging study has been performed. The protocol for the study consisted of 30 DCB samples. There were three temperatures: 80, 100 & 120°C and three times 3, 6 & 12 days. Three samples were assigned to each condition as well as to a control condition. The samples were vacuum-sealed in a mylar foil bag prior to aging to reduce the effects of oxidation. After aging the DCB specimens underwent crack growth testing under the following conditions:

- R-ratio = 0.0

- Frequency = 2 Hz

- P_{max} = 2224 N

- Testing performed at room temperature

Upon the completion of the crack growth testing, the compounds were extracted from the beams with an exacto knife and the vulcanizate analysis was performed. Due to the amount of time involved in the vulcanizate analysis, the analysis was performed on only one sample from each of the nine aging conditions as well as the control.

The results of the mechanical and chemical analysis are presented in Figure 6-18 through Figure 6-22. The crack length calibration method, equation 6.5, was applied to calculate the values of the strain energy release rate, ΔG. Examination of Figure 6-18 showed that there was a strong effect from the thermal aging on the crack growth rates. Comparison of the two aging extremes e.g. unaged and 12 days at 120°C, yielded an increase in the crack growth rates due to thermal aging approaching one order of magnitude. This increase in the crack growth rates with aging follows the same trend as the quasi-static properties, that thermal aging reduces the mechanical properties of the compound.

While Figure 6-18 is a valid comparison of the aging data, it is not useful for the purposes of modeling. For use in FEA modeling the connection between the crack growth rates and the crosslink distribution needs to be made. The dependence of the Paris-Law coefficient, α, and the exponent, β, with the percentages of poly and monosulfidic crosslinks are presented as Figure 6-19 - Figure 6-22. From the figures it was seen that a linear dependence exists for α and β with the percentages of both the poly and monosulfidic crosslinks. The coefficient, α, increased with the decreasing percentage of polysulfidic crosslinks and decreased with the increasing percentage of monosulfidic crosslinks. This trend was expected from examination of Figure 6-18. As aging proceeds the percentage of polysulfidic crosslinks decreased and the rate of crack growth increased. The value of alpha was increased by 575% due to aging at 12 days at 120°C.

The dependence of β with the percent crosslink distribution was not as strong as in the case of alpha. β decreased with the decrease in the percentage of polysulfidic crosslinks and increased with the increase in the percentage of monosulfidic crosslinks. However, the total decrease in beta between the extents of aging was only 46%.
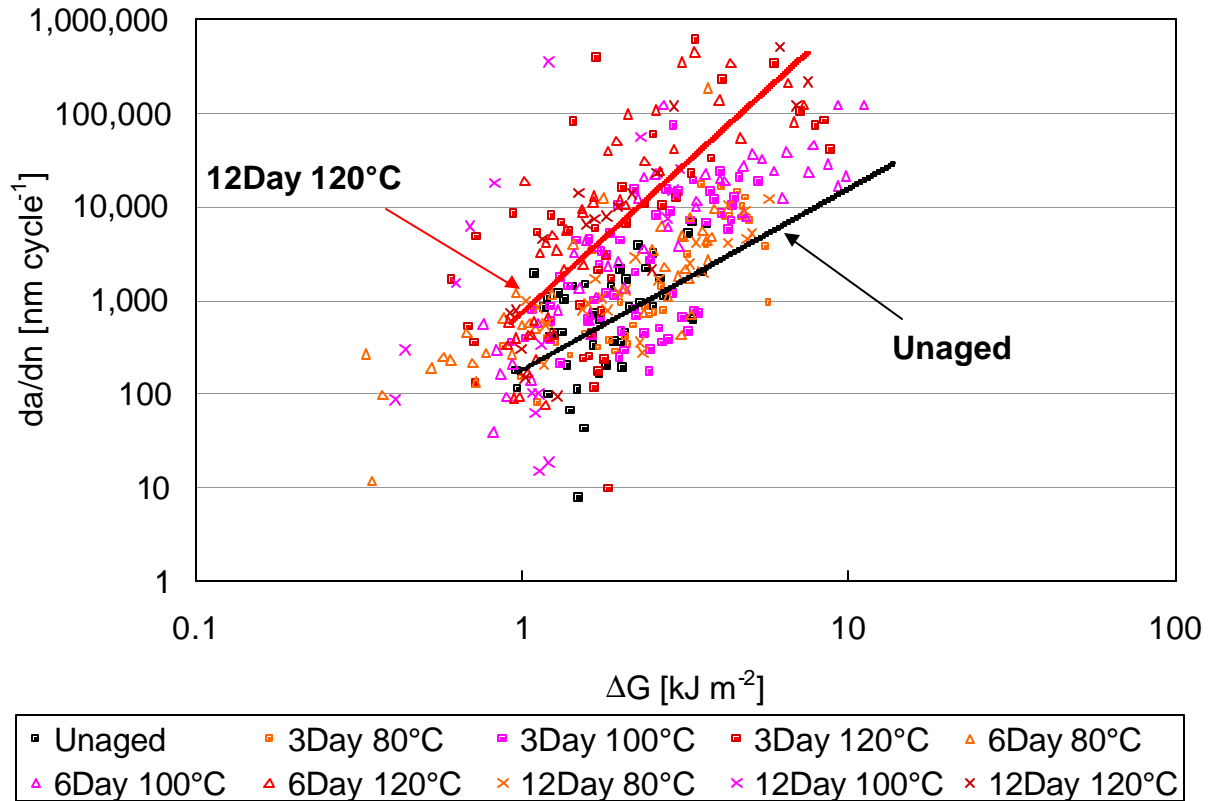
Figure 6-18   Effect of thermal aging upon the crack growth characteristics obtained from aged DCB specimens.
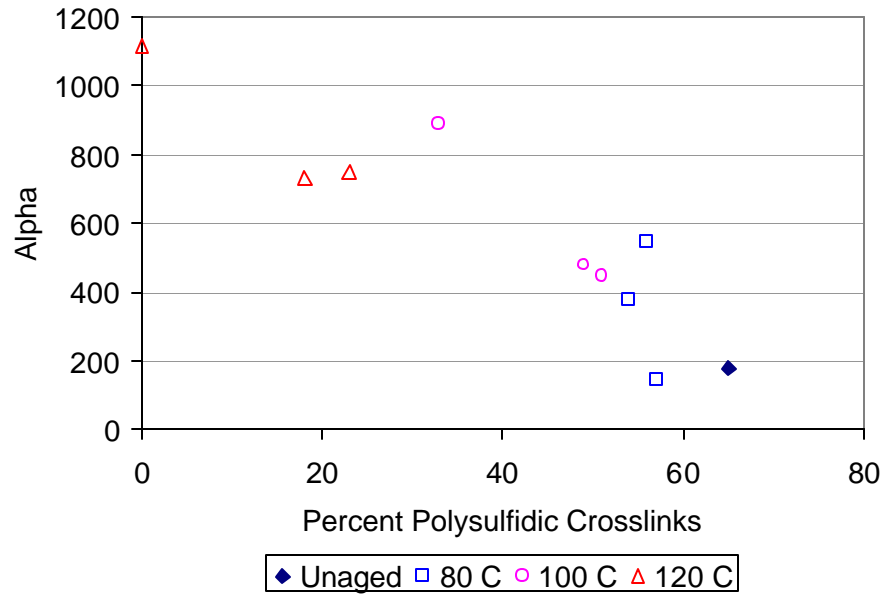
Figure 6-19   Dependence of alpha with the percentage of polysulfidic crosslinks.
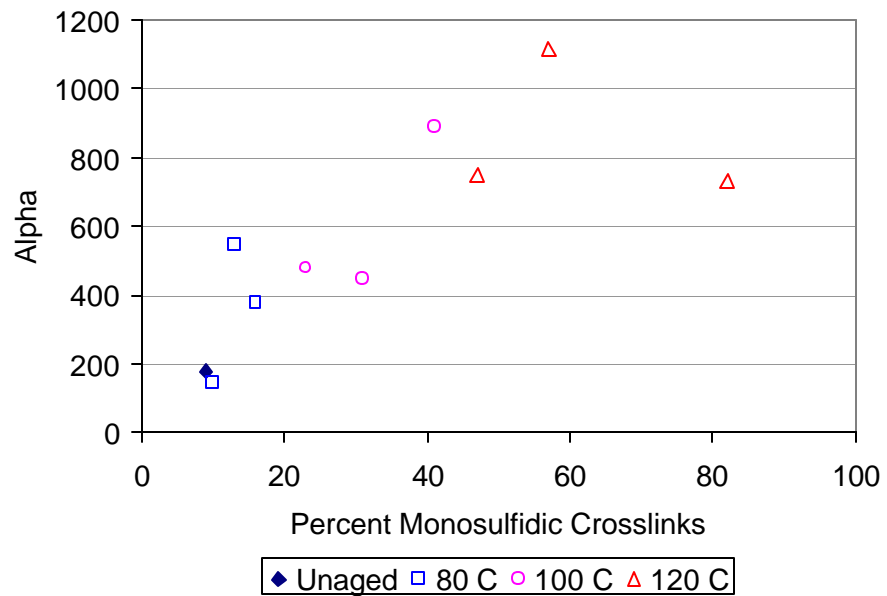
Figure 6-20   Dependence of alpha with the percentage of monosulfidic crosslinks.
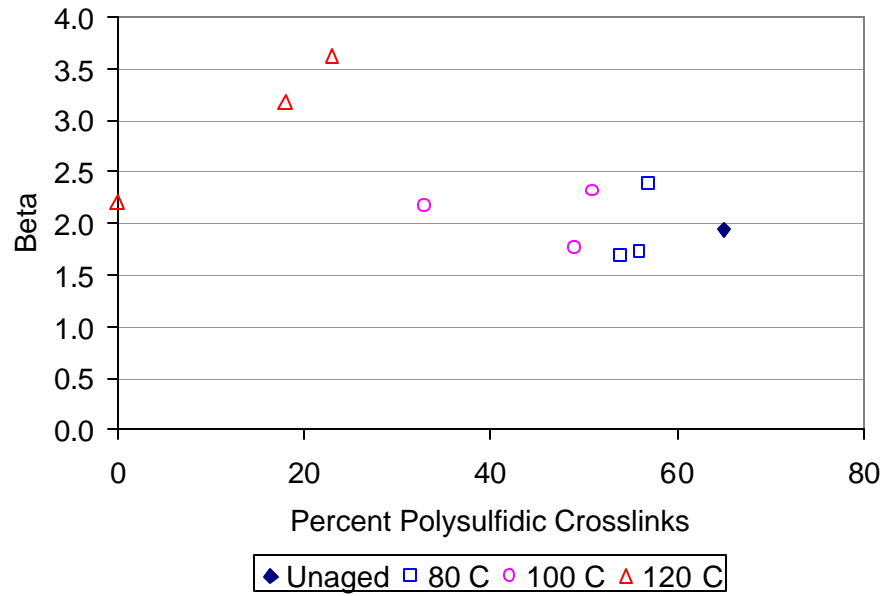
Figure 6-21   Dependence of beta with the percentage of polysulfidic crosslinks.
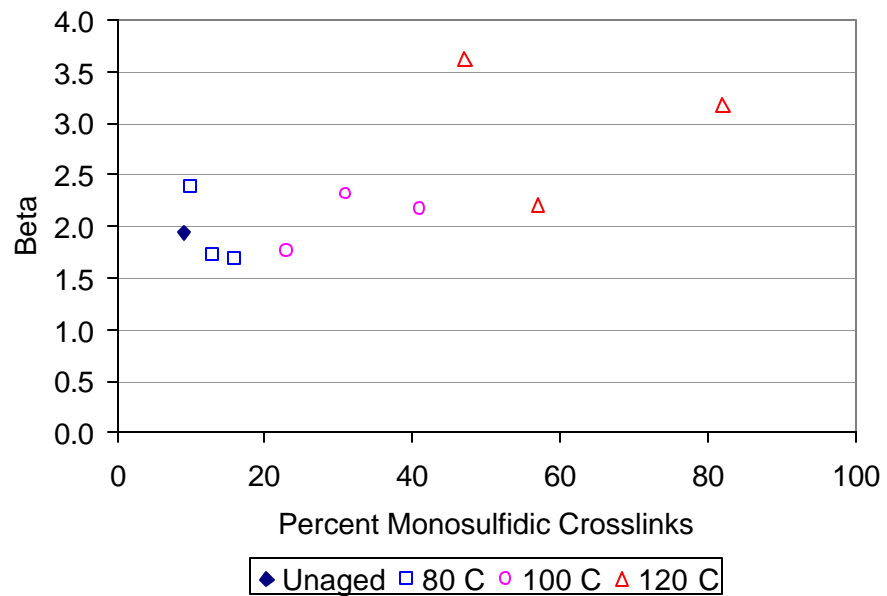
Figure 6-22   Dependence of beta with the percentage of monosulfidic crosslinks.

6.6   Summary

With the generation of the data for the aged crack growth rates as function of the crosslink distribution the loop has been closed on the degradation of material properties as functions of time at elevated temperature.   Application of the master curve and the degraded properties of chapters 4 through 6 into finite element models will allow for the prediction of the fatigue lifetimes of the 2-ply laminate.   In order to validate the finite element models and compare the results to experimental data, two-ply cord-rubber laminates have been fatigued until failure and analyzed using a delamination analysis, chapter 7.

7.   TWO-PLY LAMINATE FATIGUE

Study of the fatigue crack growth of the 2-ply laminate allowed for both verification of the finite element model as well as provided experimental data on the crack growth characteristics of the laminate. In order to validate the finite element model two different crossply laminates were examined, ±18° and ±45°. The laminates were tested in both an unaged and thermally aged condition. The fatigue crack growth of the ±18° laminates was tracked using the delamination analysis technique of T.K. O'Brien[81-85].

7.1 Fatigue Crack Growth of 2-Ply Laminate.

The failure process of the 2-ply laminate occurs by a two-step process. First edge cracks initiate at the cord rubber interface along the free edge. The appearance of these crack is due to the high shear strains that occur at the free edge. The edge cracks coalesce to form a line crack that is parallel to the direction of loading. These line cracks extend along the length of the sample and growth inward as an interply crack in a half penny shape fashion. The interply crack grows within the compound between the two plies. This mechanism can occur simultaneously on both sides of the sample. Failure occurs when the two cracks meet or a critical energy value is achieved within the remaining compound between the two interply cracks. Figure 7-1 shows the aforementioned failure mechanism for an ±18° 2-ply laminate. This is the same mechanism described in the literature[59,67].

To quantitatively capture these failure mechanisms at work in crack initiation and crack propagation, the delamination technique of T.K. O'Brien has been applied. This approach allowed for the calculation of the modulus, crack growth rate and the strain energy release rate in the presence of delamination. The approach is described in detail in the following section.
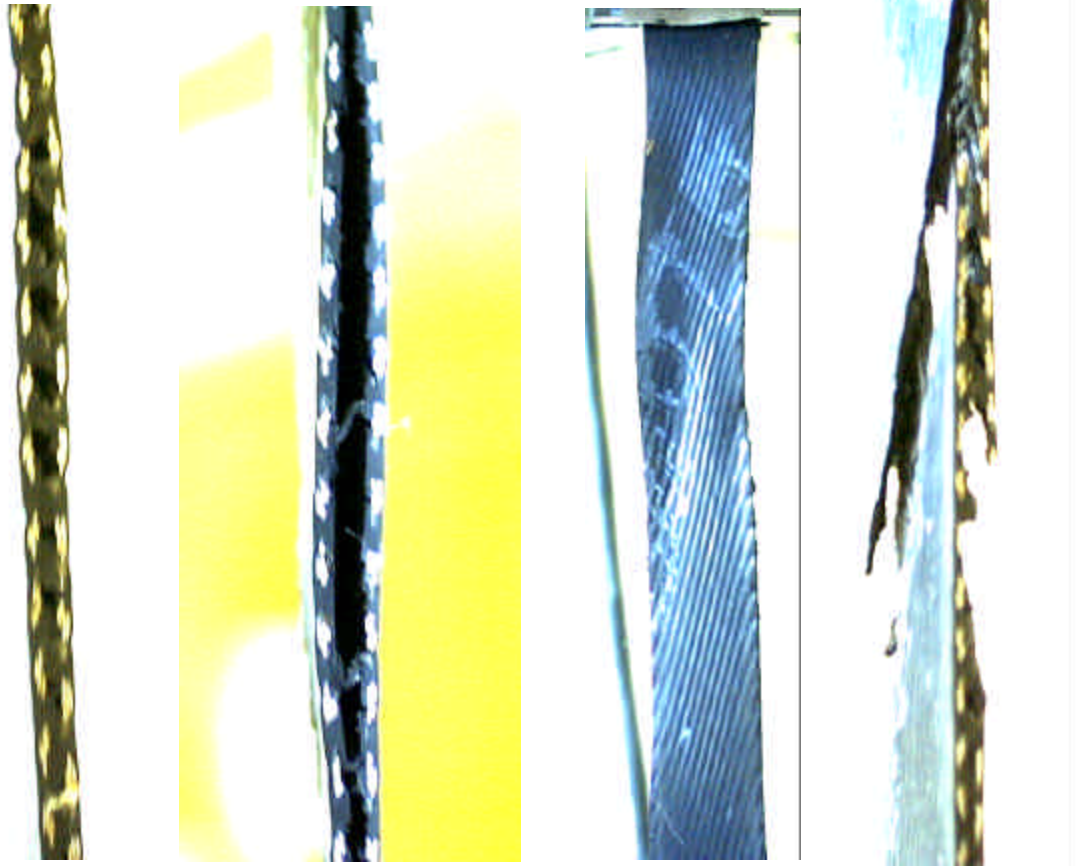
Figure 7-1   Crack growth failure mechanism along the free edge of an ±18° 2-ply laminate.

7.2   O'Brien Approach: Delamination Growth Analysis Technique

O'Brien viewed delamination as the creation of individual sublaminates. For delamination occurring at one or more interfaces a rule of mixtures assumption can be applied, such that each sublaminate formed undergoes the same axial strain, but not the same transverse strain. The resulting modulus is then given by:

$$E^* = \frac{\sum\limits_{i=1}^{m} E_i t_i}{t} \qquad [7.1]$$

where: m is the number of sub laminates formed by delamination,

E^* is the completely delaminated modulus of the laminate,

E_i is the modulus of the ith sublaminate formed by delamination and

t_i is the thickness of the ith sublaminate.

The value of the completely delaminated modulus, E^*, is dependent upon which interfaces delaminate. This occurs because the sublaminate stiffness, E_i, depends upon the through-the-thickness location of the delamination. If the laminate is only partially delaminated so that equally sized strips of delamination exist on either side of the centerline, then the modulus is given by the rule of mixture formula:

$$E = \left(E^* - E_{Lam} \right)\frac{a}{b} + E_{Lam} \qquad [7.2]$$

where: a is the width of the delamination and

b is the half width of the laminate.

Thus for a given delaminated set of plies under fatigue the delamination can grow with an increasing number of cycles until the point that is has completely traversed the width of the laminate. At the point of impingement of the two cracks the modulus of the laminate is equal to E^*. Using the strain energy release rate, G, O'Brien estimated delamination growth rates. In doing so, he assumed that the delamination growth rate as a function of G obeyed a Paris-law relationship of the form given in equation 6.2. The strain energy release rate is then given by:

$$G = \frac{e^2 t}{2m}\left(E_{Lam} - E^* \right) \qquad [7.3]$$

The strain energy release rate is the work done in propagating the delamination minus the rate at which energy is stored by the system due to delamination growth. Substitution of the relations for delamination growth into the equation for the laminate modulus after the initiation of delamination, allows for the calculation of the reduction in the delaminated laminate modulus versus cycles.

It is also possible to estimate the crack growth by the relation:

$$\frac{da}{dN} = \left(\frac{b}{E^* - E_{Lam}} \right)\frac{dE}{dN} \qquad [7.4]$$

The term $\dfrac{dE}{dN}$ is the rate of change of the laminate stiffness with respect to cycles. This form of the equation does not depend upon experimental data for the measured crack size, but rather is a relation for the reduction in stiffness versus cycles.

7.3 ± 18° Fatigue Crack Growth

Fatigue tests were performed on $\pm18^o$, 2-ply cord rubber laminates. The cord consisted of 5 brass-plated steel wires helically wound together. The elastomer was compound B. The laminates were laid up in a crossply configuration with a cord spacing of 14 ends per inch and then vulcanized under pressure in a hot press for 27 minutes at 150°C. The final dimensions of the samples were 26.67 x 2.54 x 0.4 cm. To obtain the modulus of the completely delaminated 2-ply laminate, E*, a single 18° cord rubber lamina was fabricated. The single ply laminate was fabricated using the same constituent material properties and cure conditions as the $\pm18°$ 2-ply laminate.

The samples were tested in an Instron servo-hydraulic test frame fitted with a MTS 407 controller and gripped with MTS hydraulic grips. The length of the grip wedges was 6.03 cm. The samples were inserted in the grips to the full length of the grip wedges and were tabbed with 180 grit sand paper to reduce the potential of grip slip. The gage length of the samples was 18.89 cm. For this gage length and the cord angle each sample possessed a safe region, unaffected by clamping, for mechanical characterization of 5 cm[86].

7.3.1 ±18° S-N Curve Generation

Prior to the delamination analysis the fatigue life of the laminates was determined for the generation of a S-N curve. The samples were tested in load control at room temperature under an R-ratio of zero at a frequency of one hertz. The number of cycles to failure were recorded and plotted against the nominal engineering stress level. This testing was conducted for both the unaged condition and an aged condition of 6 days at 100°C. The experimentally determined S-N curves are presented in Figure 7-2. The two curves were essentially the same. These curves will used in the verification of the finite element models by comparing the experimental number of cycles to those predicted by the models.

117
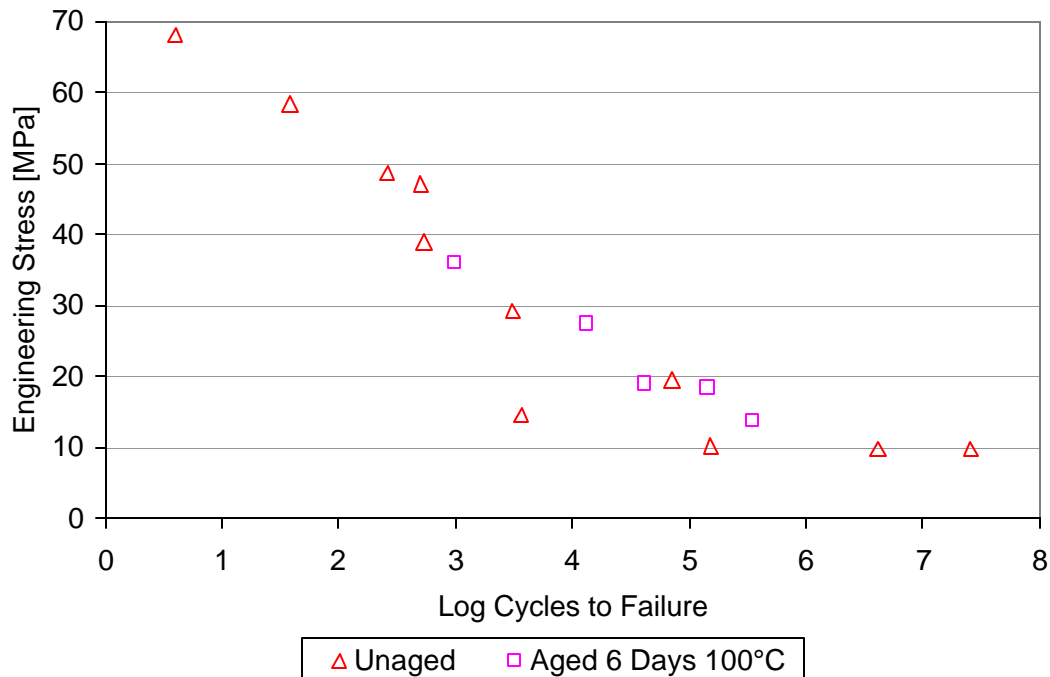
Figure 7-2   ±18° 2-ply laminate S-N curve.

7.3.2   Unaged ±18° 2-Ply Laminate Delamination Analysis

In order to perform the O'Brien analysis, a "linear region" of the ±18° 2-ply sample needed to be probed by the fatigue tests. A linear region of engineering stress versus strain was necessary so that the modulus could be calculated. Figure 7-3 is the load versus displacement curve for a ±18° 2-ply specimen. Based upon the figure and the desire to reduce viscoelastic effects the following testing conditions were applied for the fatigue crack growth.

- Testing performed at room temperature under load control,
- $P_{max} = 1780$ N,
- R-ratio = 0
- Testing frequency = 1 Hz
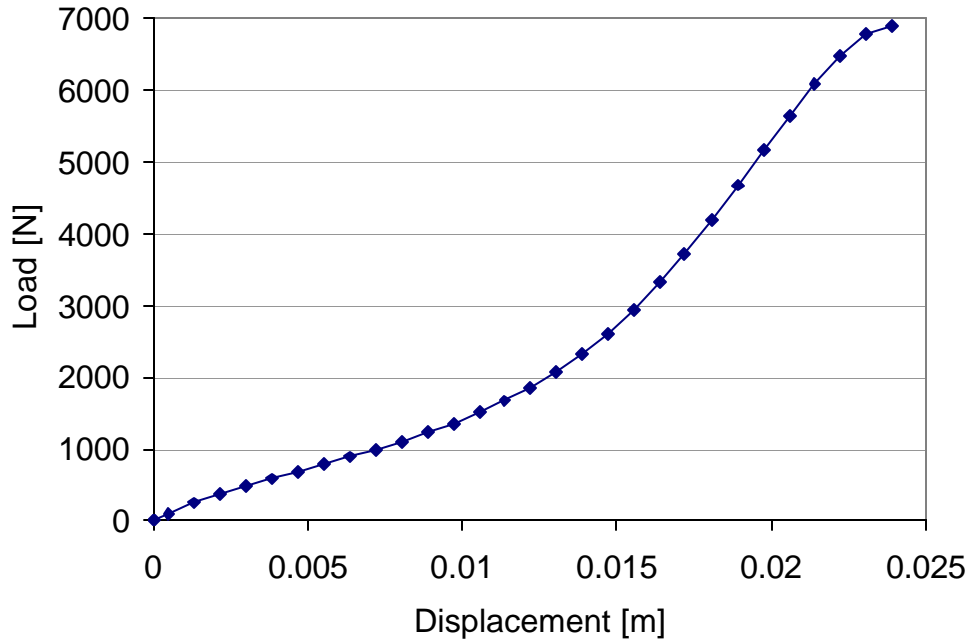
Figure 7-3   Load versus displacement curve for the 2-ply laminate.

During the course of the fatigue test the sample was removed and scanned by ultrasonic C-Scan. The C-Scan was performed in a water bath at room temperature using a 15 MHz transducer. For the purposes of damage analysis the sample was discretized into thirteen layers during the scan. Figure 7-4 is an ultrasonic C-Scan image of a sample, which shows significant delamination the damage appearing as the white region. Following the scan the images were processed using Adobe® Photoshop® to determine a threshold between damaged, white, and undamaged, black, regions. The damaged areas were erased from the image so as to yield a clear calculation of the percent damage area. Finally the percentage of the damaged area was determined using an image analysis program.

Figure 7-4   **Ultrasonic C-Scan image of an ±18° 2-ply laminate showing significant delamination damage. The white regions are the delamination. The steel cords can be seen as well.**

Three individual ±18° 2-ply laminate samples were subjected to this fatigue process. Figure 7-5 contains a plot of the modulus versus cycles for the three samples as well as a reference sample that was fatigued until failure without interruption. The three samples and the reference are in good agreement. There appears to have been no effect on the laminate modulus due to starting and stopping the test in order to perform the ultrasonic C-Scans.
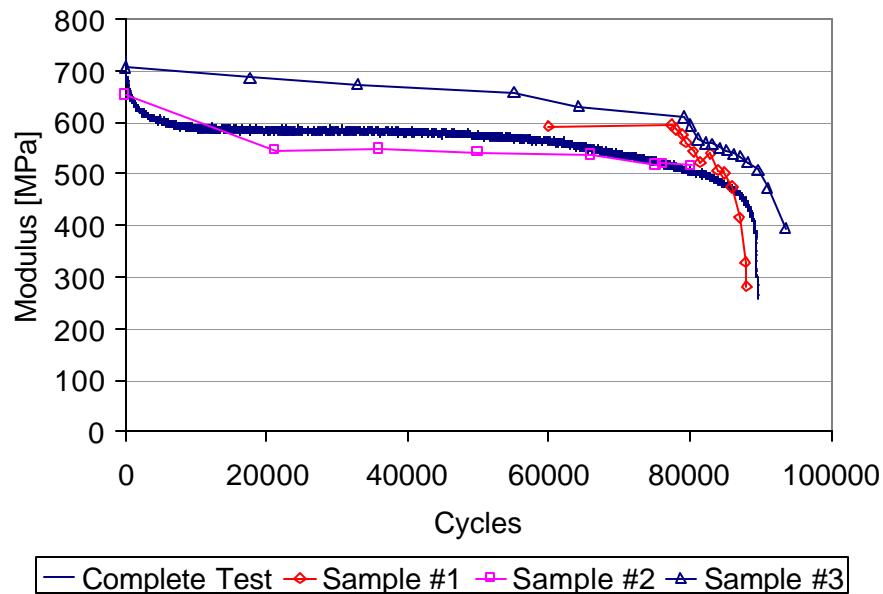
Figure 7-5   **Experimental modulus versus cycles.**

For each step in fatigue cycles the modulus of the laminate was taken as the average of the measured modulus values after 100 fatigue cycles. This value was chosen so that the cyclic softening

effect, Mullins effect[10], and the appropriate testing conditions could achieve a steady state value. The minimum fatigue step used in the delamination analysis was one thousand cycles.

One general aspect of the O'Brien delamination analysis was that the modulus should be a linear function of the delamination area. This linear decrease of the modulus with increasing delamination area for the ±18° 2-ply fatigue is presented in Figure 7-6. Using equation 7.2 the modulus of the sample was predicted and compared to the experimental data. In the case of the 2-ply laminate the completely delaminated modulus, $E*$, was simply the modulus of the ±18°degree single ply laminate. The single ply modulus was measured at the same maximum strain value that was seen by the undamaged 2-ply laminate after 100 cycles. This maximum value was 3.0 percent strain. The 18° single ply laminate modulus value at this level of global strain was 48 MPa. This value was measured after the single ply laminate had been subjected to 100 cycles to that maximum strain level.
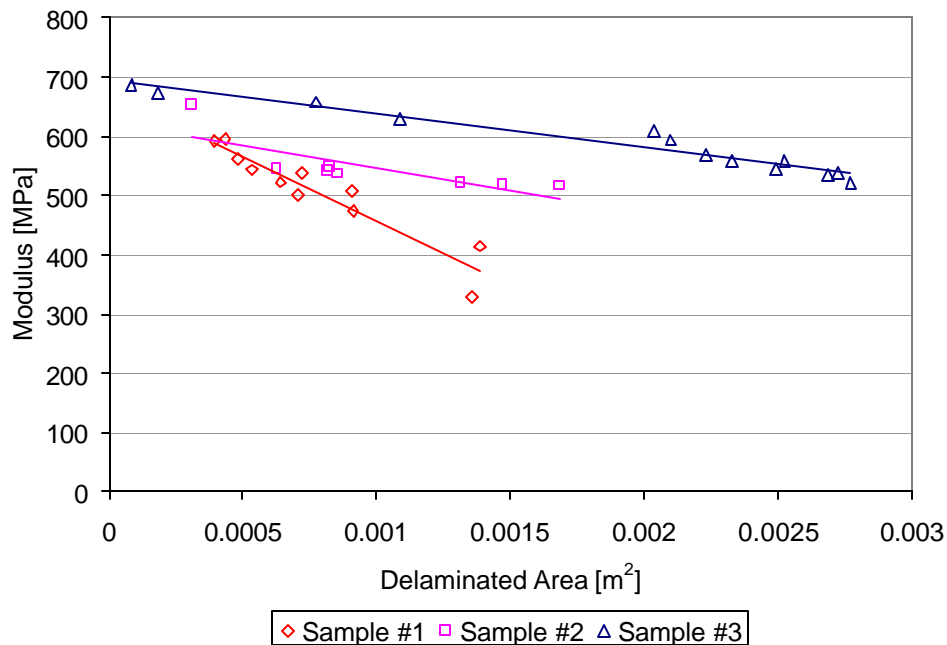
Figure 7-6   Modulus versus delamination area.

121

Figure 7-7 is a plot of the predicted versus experimentally obtained modulus values for the 2-ply laminate. The predicted and the experimental values were in close agreement, with the predicted value being slightly less than that experimentally observed. The difference between the predicted and the experimental values may be due to additional damage that was not accounted for in the O'Brien delamination analysis.
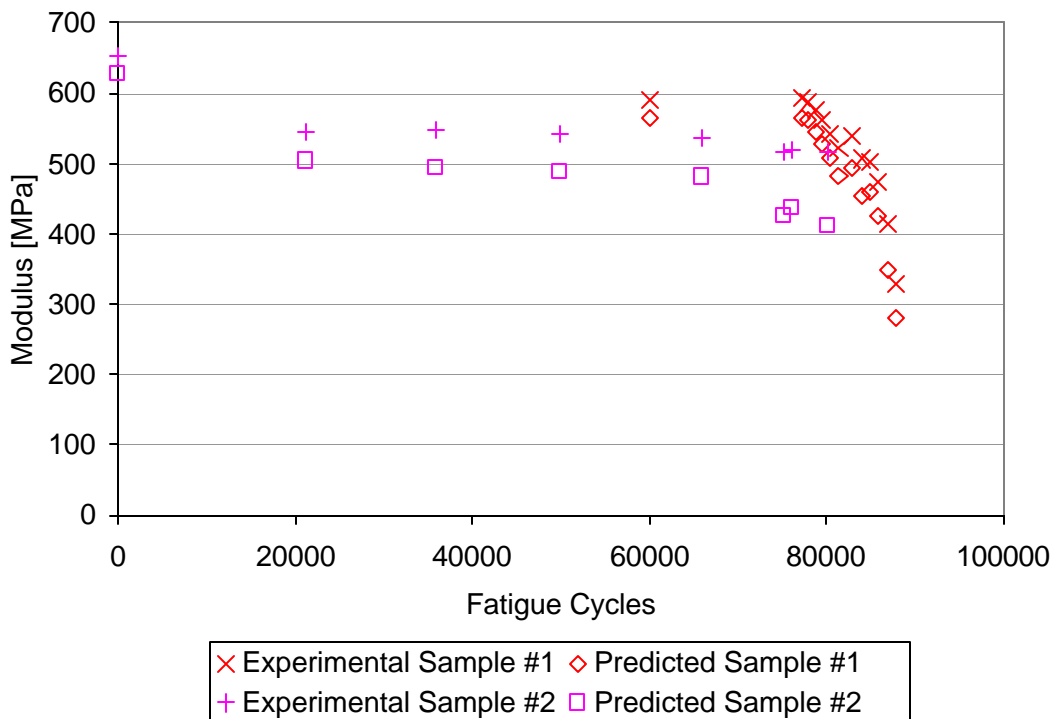
Figure 7-7   Predicted modulus, E, using equation 7.2 as a function cycles compared to the experimentally obtained values.

From examination of Figure 7-5 - Figure 7-7 it appeared that the delamination approach was successful. This is not a trivial statement, as this approach has never been applied to non-linear cord-rubber laminates. Using equation 7.3 the strain energy release rate was calculated. The change in the strain energy release rate was obtained from the difference between successive delamination increments. The crack growth rate for the edge delamination was then calculated using equation 7.4. The

calculated $\dfrac{da}{dN}$ versus ΔG plots are presented in Figure 7-8. The curves were reasonable and all had

the same slope. The observed crack growth rates were significantly faster than those from the Mode I

DCB testing. This faster crack growth was reasonable since the state of stress in the 2-ply laminate was

more complex than the purely Mode I fracture of the DCB. These data from the delamination analysis

will be used in the finite element models predictions of chapter 8.
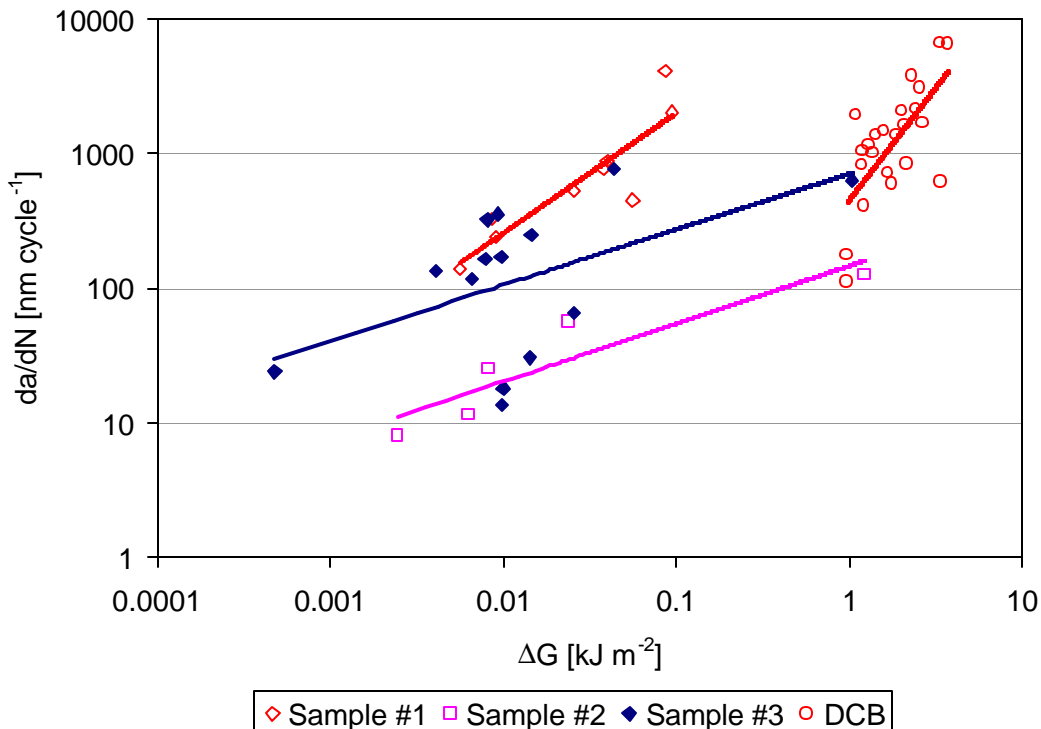
Figure 7-8   Calculated crack growth rates versus DG for the 2-ply laminate.

7.3.3   Aged ±18° 2-Ply Laminate Delamination Analysis

To determine the effect of aging on fatigue life as well as provide validation for the life prediction

and modeling, isothermal anaerobic aging has been performed on five ±18° 2-ply laminates. This testing

was possible because the failure of the laminates was due to crack initiation and propagation within the

compound. Two samples were used for the delamination analysis while the third was a control. The

123

two remaining samples were tested under quasi-static conditions. The aging was performed in the same manner as with the thermally aged DCB specimens. The ±18° laminates were vacuum-sealed in a mylar foil bag prior to aging to reduce the effects of oxidation. The samples were aged for 6 days at 100°C. This temperature, rather than 120°C, was chosen as it was found that during the aging of the DCB specimens at 120°C the mylar foil bag melted and adhered to the DCB adherends. The melted parts of the bag had to be removed prior to testing the samples. This was not a problem with the DCB samples, but in the case of the ±18° 2-ply laminates the bags would melt directly onto the laminates. Removal of the bag parts would have resulted in the destruction of the aged laminates. To prevent this from occurring the more modest aging condition of 6 days at 100°C was chosen.

After aging, two samples were tested under quasi-static conditions to determine the linear regions for the fatigue crack growth delamination approach. The quasi-static tests were run under displacement control at the constant rate of 95 mm min^{-1}. The average results of the quasi-static test are compared to the unaged stress-strain behavior in Figure 7-9. There was a significant effect on the mechanical behavior due to the thermal aging. The ultimate strain was reduced by 40% but the ultimate stress was approximately the same. The overall behavior of the laminate was the same, with an initial linear region up to 20 Mpa.
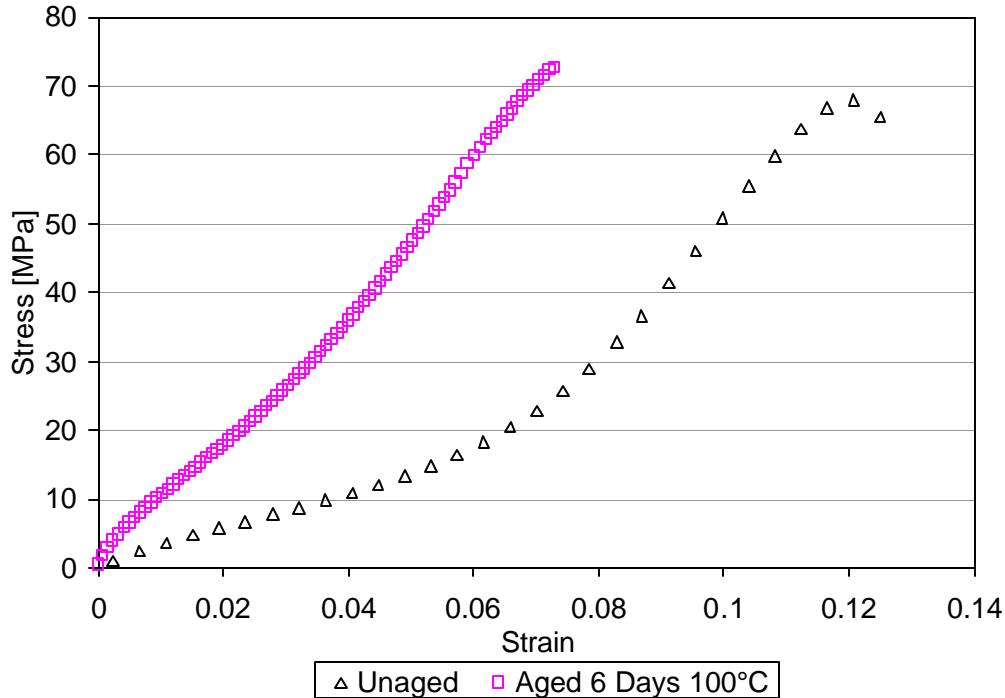
Figure 7-9   Stress-strain curve showing the effect of thermal aging on the mechanical behavior of an ±18° 2-ply laminate.

The increase in the stiffness of the ±18° 2-ply laminate due to aging was in accordance with the thermal aging data of chapter 4.   Aging for 6 days at 100°C served to increase the modulus of compound B, Figure 4-17.   Based upon this figure the same testing conditions that were applied to the fatigue of the unaged ±18° 2-ply laminates were applied to the aged ±18° 2-ply laminates.   The conditions were:

- Testing performed at room temperature under load control,
- P_{max} = 1780 N,
- R-ratio = 0,
- Testing frequency = 1 Hz.

In order to perform the analysis the modulus of an aged single ply laminate needed to be known. Unfortunately no single ply laminates remained to be aged. Classical laminate theory, CLT, was applied to predict the modulus of the laminate. The Halpin-Tsai equations were used for the determination of

the E_2 and G_{12} inputs, while the rule of mixtures, ROM, was applied for the calculation of E_1, v_{12} and v_{23}. Comparisons of the experimentally obtained modulus values with those obtained from single pull quasi-static tests on different crossply configurations were in close agreement, Figure 7-10. This agreement showed the applicability of CLT to the calculation of the aged single ply laminate modulus. Using the aged modulus data from chapter 4 and the Halpin-Tsai and ROM models the modulus was calculated to be 29 MPa. This value was applied to the delamination analysis of the aged 2-ply laminate.

The results of the delamination analysis were similar to those obtained from the unaged ±18° 2-ply laminate. The modulus of the laminate was a linear function with the delamination area, Figure 7-11. The effect of aging on the modulus can be seen in Figure 7-11 when compared to the modulus versus delamination area response of the unaged laminates. The modulus of the aged laminate was significantly less than the unaged laminate.
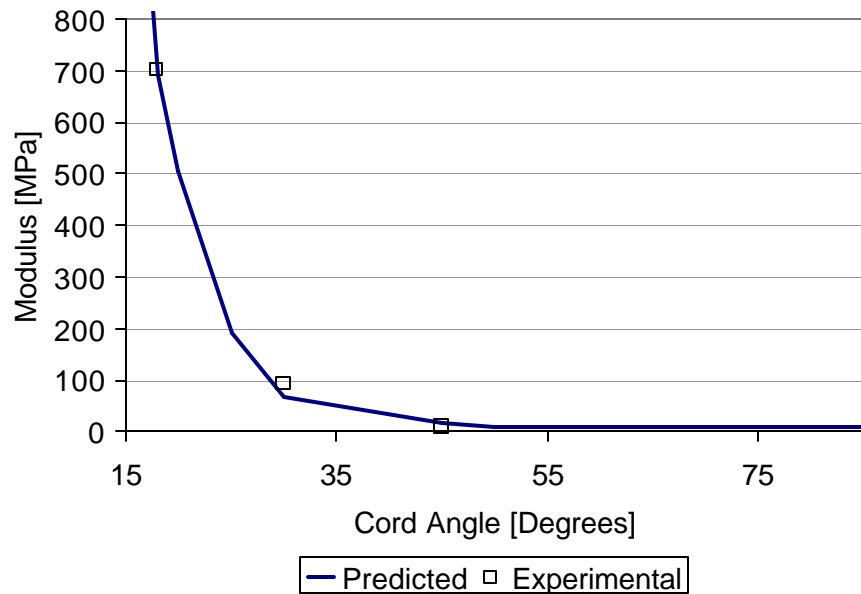
Figure 7-10   CLT predictions versus the experimentally obtained modulus for the unaged ±18° 2-ply laminate.

The predicted versus the experimentally obtained modulus values are presented in Figure 7-12. As in the case of the unaged ±18° 2-ply laminate the predicted and the experimental values were in close agreement, with the predicted value being slightly less than that experimentally observed. There was a large difference in the number of cycles to failure between the two samples. In the first sample, failure occurred after 41000 cycles, for the second sample failure occurred after 175457 cycles. The reason for the discrepancy was unclear; however, the second sample was manufactured nearly a year after the first. It was possible that during this time there was a change in the compound similar to that presented in Figure 2-11. To clarify this discrepancy a third sample was run as a control. This third sample failed after 202153 cycles.

The calculated $\dfrac{da}{dN}$ versus ΔG curve for the 6 day at 100°C thermally aged ±18° 2-ply laminates are presented in Figure 7-13. The effect of aging on the 2-ply laminate can be compared with the aging effect seen on DCB specimens. There was little to no change on the da/dn verus ΔG behavior of the laminate. This same trend occurred in the case of the 6 day at 100° C aged DCB. This data will be used in the finite element models to predict the fatigue life of thermally aged ±18° 2-ply laminate.
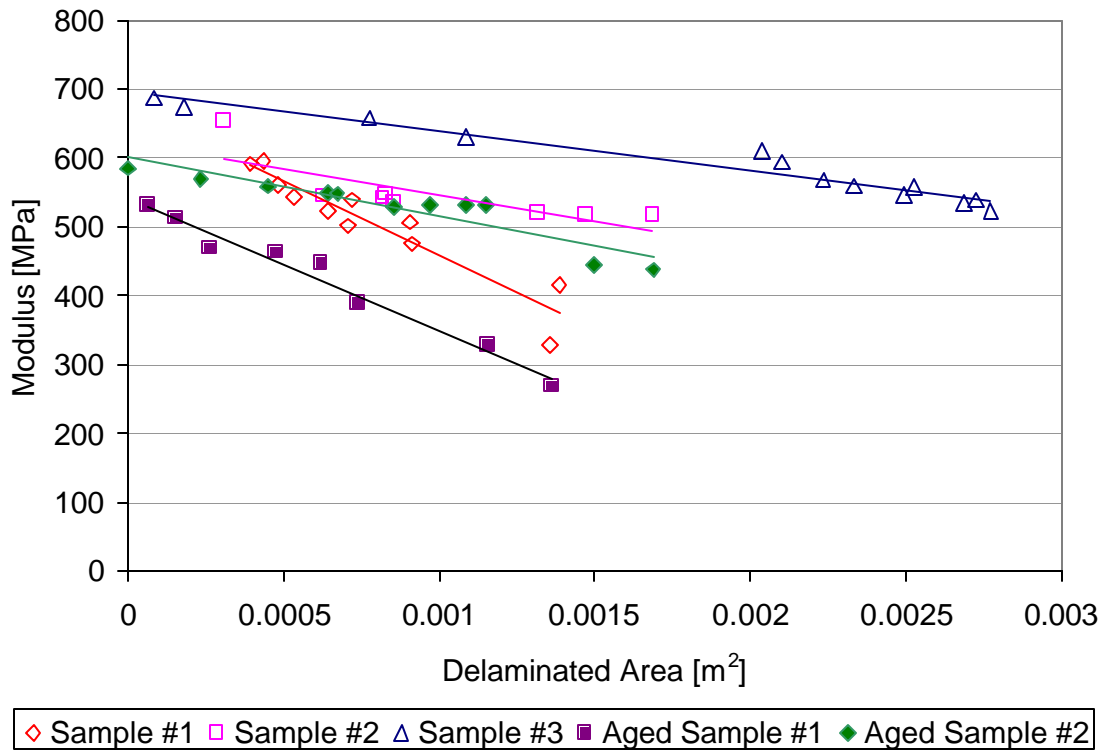
Figure 7-11   **Modulus versus the delamination area of the unaged and thermally aged ±18° 2-ply laminates.**
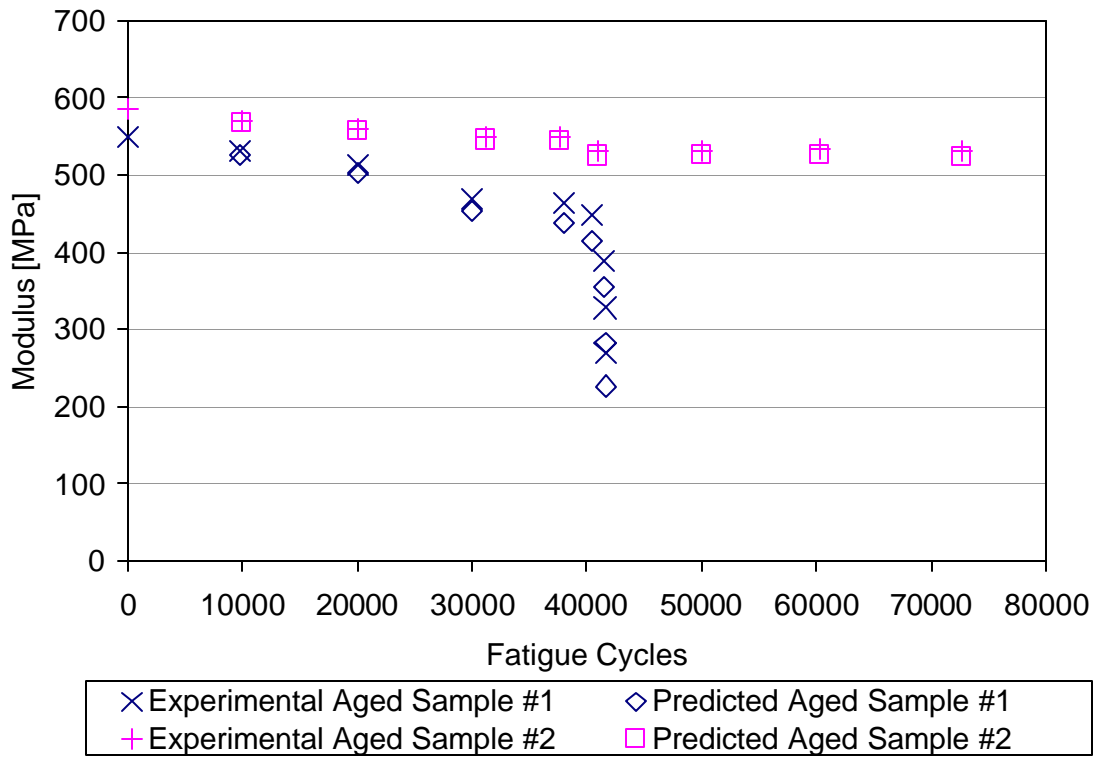
Figure 7-12   **Predicted modulus versus cycles of the two 6 day at 100°C thermally aged ±18° 2-ply laminates compared to their experimentally obtained modulus values.**
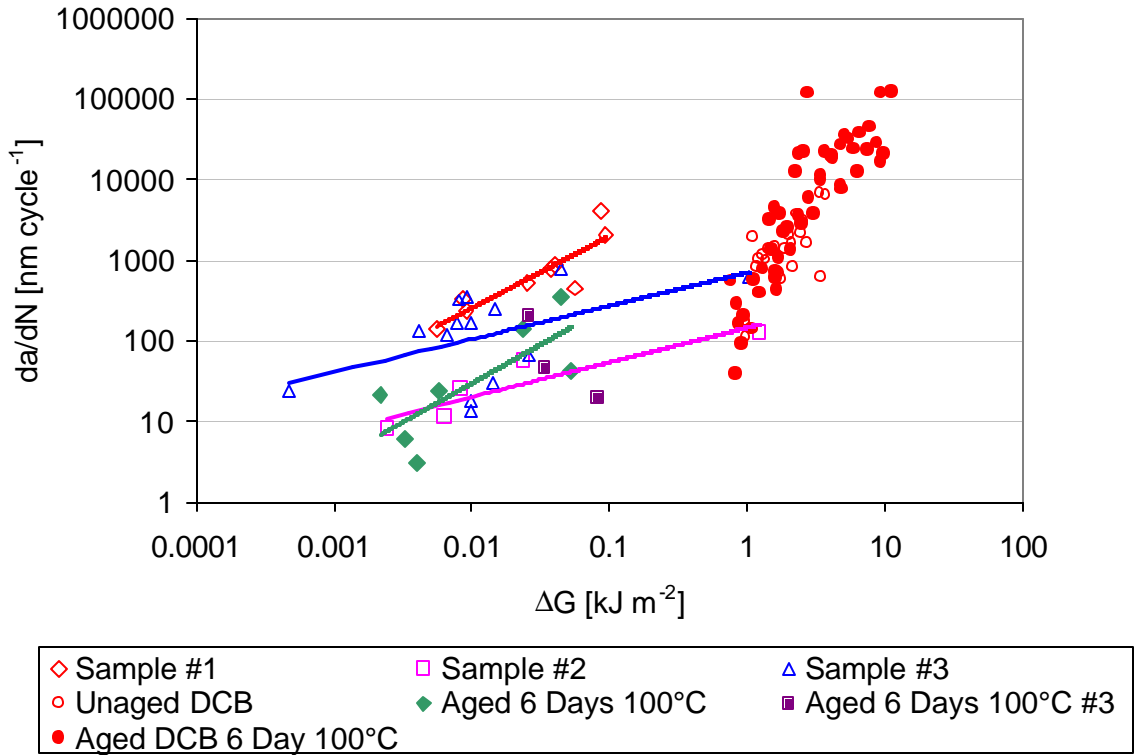
Figure 7-13   Calculated aged 2-ply laminate crack growth rates compared to those obtained from the unaged 18° 2-ply laminate, unaged DCB and 6 day 100°C aged DCB.

7.4   ±45 ° Fatigue Crack Growth

Quasi-static and fatigue tests were performed on ±45° 2-ply cord rubber laminates. As with the ±18° laminates, the cord consisted of 5 brass-plated steel wires helically wound together. The elastomer was compound B. The laminates were laid up in the crossply configuration with a cord spacing of 14 ends per inch and then vulcanized under pressure in a hot press for 27 minutes at 150°C. The final dimensions of the samples were 26.67 x 2.54 x 0.4 cm. To obtain the modulus of the completely delaminated 2-ply laminate, E*, a single 45° cord rubber lamina was fabricated. The single ply laminate was fabricated using the same constituent material properties and cure conditions as the ±45° 2-ply laminate.

The samples were tested in an Instron servo-hydraulic test frame fitted with a MTS 407 controller and gripped with MTS hydraulic grips. The length of the grip wedges was 6.03 cm. The samples were inserted in the grips to the full length of the grip wedges and were tabbed with 180 grit sand paper to reduce the potential of grip slip. The gage length of the samples was approximately 18.89 cm. For this gage length and the cord angle each sample possessed a safe region, unaffected by clamping, for mechanical characterization of 10 cm[86].

7.5.1 ±45° S-N Curve Generation

As in the case of the ±18° laminates, prior to the delamination analysis the fatigue life of the laminates was determined in order to generate a S-N curve. The samples were tested in load control at room temperature under an R-ratio of zero and frequency of 0.25 Hertz. The number of cycles to failure were recorded and plotted against the nominal engineering stress level. The experimentally obtained S-N curve is presented as Figure 7-14. This curve will be used in the verification of the finite element models by comparing the experimental number of cycles to those predicted by the models. A S-N curve for an aged condition was not generated due to a lack of samples.
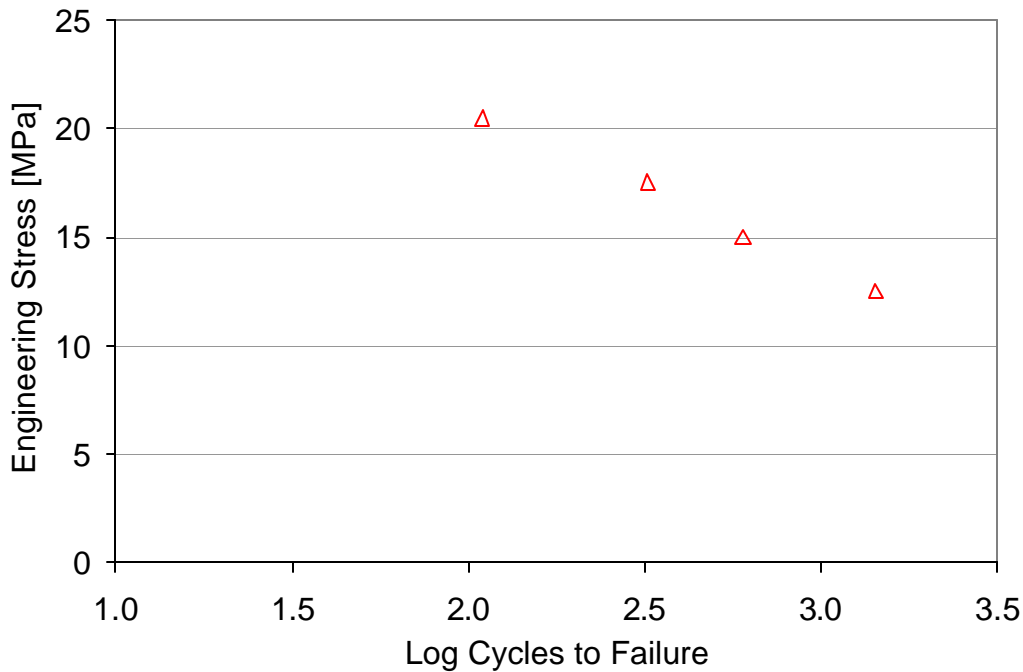
Figure 7-14　±45° 2-ply laminate S-N curve.

7.5.2　±45° 2-Ply Laminate Delamination Analysis

The delamination analysis was attempted on the ±45° 2-ply laminates; however, the attempt was unsuccessful. The ±45° 2-ply laminate failed in only a few thousand cycles. This reduced number of cycles to failure was directly related to the amount of delaminated area that was possible in the laminate. The maximum area that was available for delamination was limited by the cord angle. The lower cord angle of the ±18° 2-ply laminate yielded a higher area for delamination than the ±45° 2-ply laminates. This difference is shown in Figure 7-15. This lower delamination area before failure made it impossible to successfully obtain a substantial amount of data points to perform the analysis. The fatigue steps in the ±18° 2-ply laminate were a minimum of one thousand cycles. Keeping the same experimental procedure would have resulted in three fatigue steps. This would have not been enough data to perform the analysis.
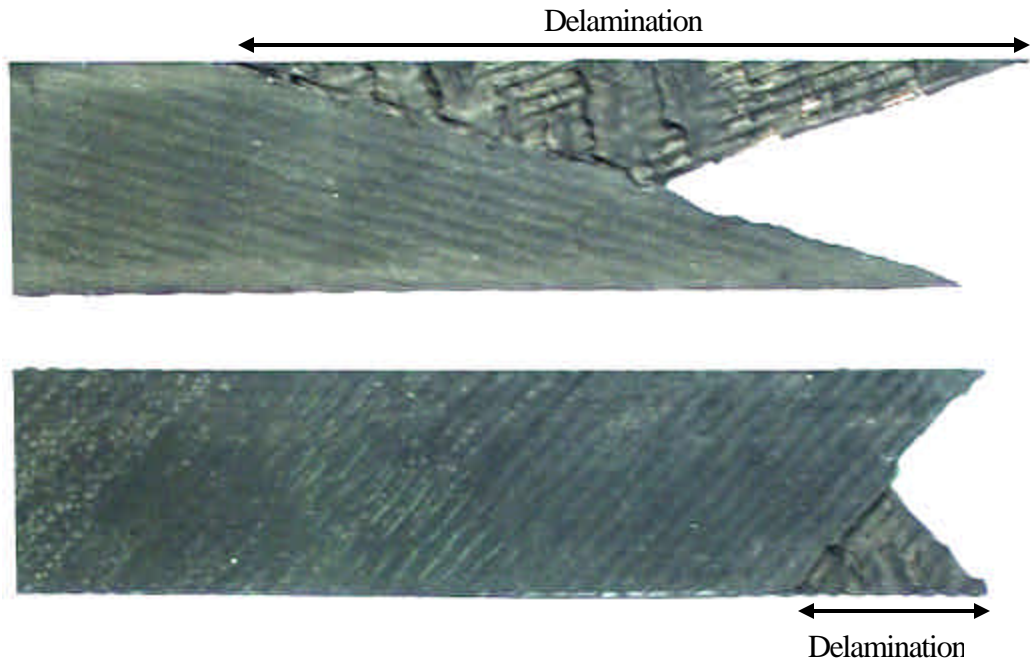
Figure 7-15   Comparison of the delamination area between the ±18° (upper) and ±45° (lower) 2-ply laminates.

Despite the inability to perform the analysis on either the aged on the unaged ±45° 2-ply laminates, quasi-static tests were performed on the laminates to see the effect of thermal aging. The tests were conducted using the same experimental procedure as for the aged and unaged ±18° 2-ply laminates. The average results are shown in Figure 7-16. The aging effect on the ±45° 2-ply laminate was the same as seen in the case of the ±18° 2-ply laminate, Figure 7-9. Thermal aging served to increase the modulus of the laminates. This was in agreement with the aged compound B data from chapter 4.
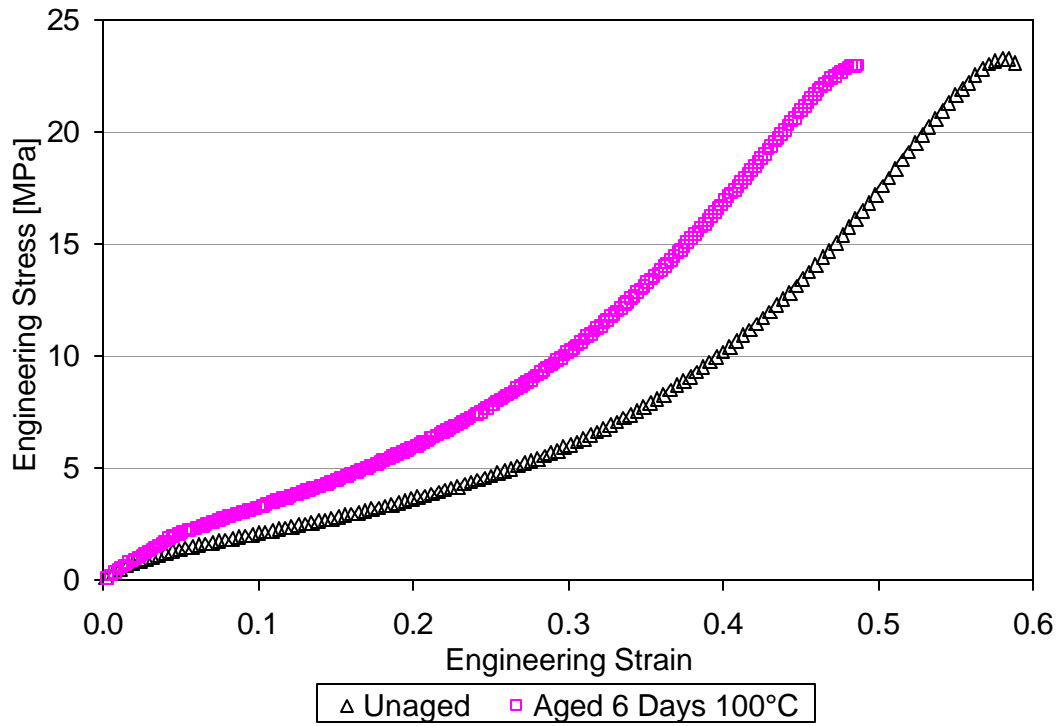
Figure 7-16   Stress-strain curve showing the effect of thermal aging on the mechanical behavior of an ±45° 2-ply laminate.

8.   LIFE PREDICTION

The life prediction incorporated application of the master curve and the degraded properties of chapter 4 and 6 and 7 into finite element models of the 2-ply laminate. The modeling was performed using the FEA software ABAQUS. The finite element models were rubber and reinforcing cord hybrid models. The models consist of 3-D brick elements to represent the rubber and membrane elements to represent the reinforcing cord. For the purposes of the analysis, the prediction has been discretized into two sections: crack initiation and crack propagation. The value of the life prediction was a sum of the number of cycles predicted for crack initiation and crack propagation. The modeling did not include the number of cycles spent while a series of socket cracks coalescence to form a line crack. This coalescence issue is of great importance and should not be ignored; however, due to the complexity of the issue the topic was not included in this analysis. The intent of the life prediction was to demonstrate the applicability of the thermally aged degraded material properties and the approaches to crack initiation and crack propagation. Expanded modeling to include crack coalescense is intended for future work.

In the model for both crack initiation and crack propagation a geometrically non-linear neo-hookean material behavior model was used. This is a common material type used for rubber in finite element modeling because of the large strains to failure and the non-linear behavior of the rubber. Neo-hookean behavior is defined by one material constant, C_{10}. For input into the finite element models, C_{10}, was determined from the quasi-static stress-strain behavior. An ABAQUS example problem[87] was utilized in which the C_{10} value was calculated from the user supplied stress-strain behavior of the material.

Application of this approach for C_{10} allowed for both the constant to be directly determined from experimental data as a function of crosslink type for use with the master curves. The dependence of C_{10} for compound B on the percentage of poly and monosulfidic crosslink is presented in Figure 8-1

and Figure 8-2. In the figures the same linear correlation with the percentage crosslinks as the modulus, Figure 4-17, can be seen.
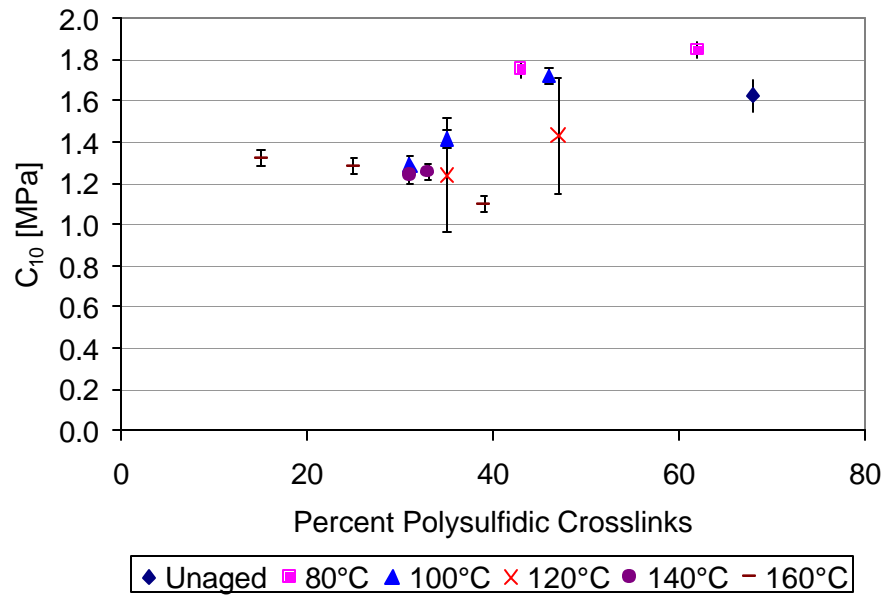
Figure 8-1 C_{10} **of compound B versus the percent polysulfidic crosslinks. The error bars represent one standard deviation.**
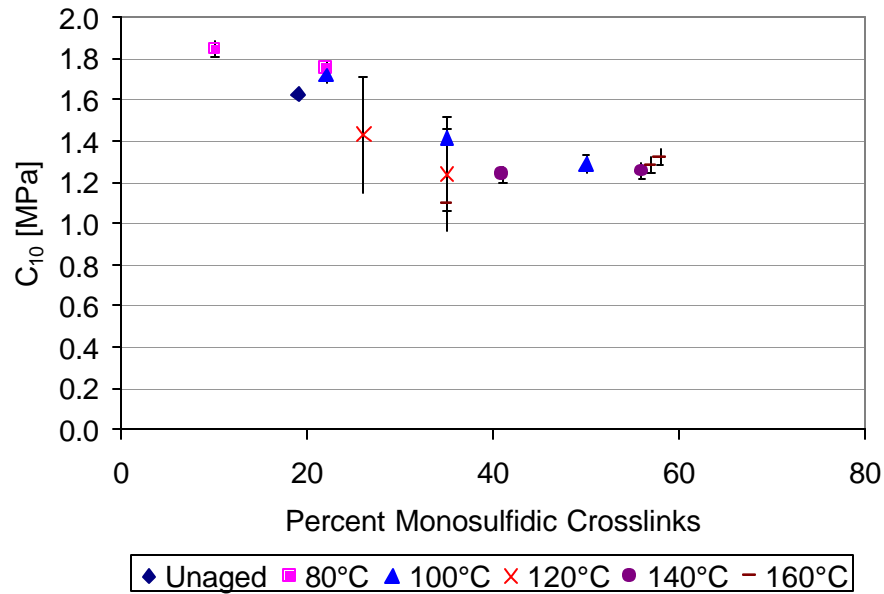
Figure 8-2 C_{10} of compound B versus the percent monosulfidic crosslinks. The error bars represent one standard deviation.

8.1 Crack Initiation

Initiation was defined as first element failure. Physically, this corresponds to the occurrence of a "socketing" crack. Socket cracks are cracks which form at the reinforcing cord-rubber interface. The existence of these cracks is driven by local stress and strains. In order to predict the initiation of these crack a refined local hybrid model was applied, Figure 8-3. In this model only a few steel cords in the center of the ply are explicitly represented and meshed with 3D brick elements while the other cords are represented using membranes elements. Use of this model yielded the local stress and strain values for incorporation into the residual strength failure function.
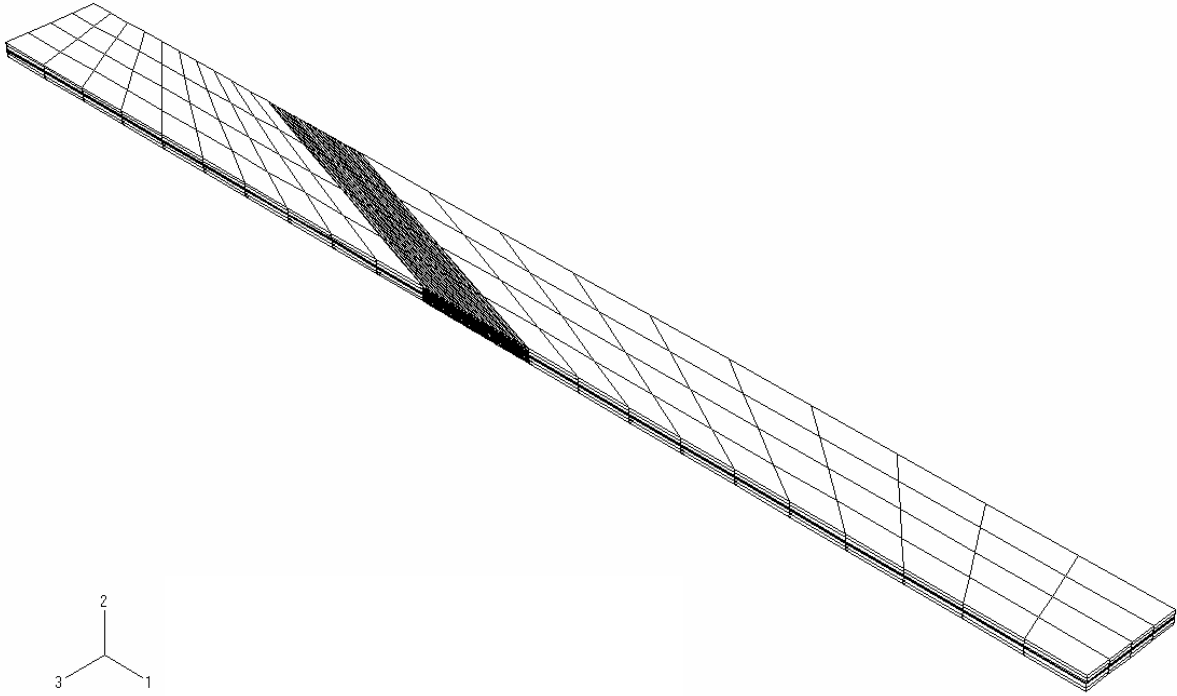
Figure 8-3   Hybrid model for crack initiation showing the explicitly designed cords.

8.1.1   Residual Strength Approach

The residual strength approach of Reifsnider and Stinchcomb[88] was applied to the prediction of the number of cycles for crack initiation. The goal of this approach was the calculation of the remaining strength:

$$Fr = 1 - \int_{0}^{t_i} (1 - Fa) j t^{j-1} dt \qquad [8.1]$$

where: Fr is the remaining strength,

Fa is the failure function,

t is a generalized time such as $\dfrac{n}{N}$ and

j is a curve fitting constant where $0 \le j \le \infty$.

For the case of $j = 1$ the equation for the remaining strength is the same as that examined by Broutman and Sahu[89], and as j approaches infinity the number of cycles to failure approaches the Miner's sum. Failure of the system occurs when the remaining strength is equal to the failure function.

For the calculation of the number of cycles for crack initiation the residual strength approach has been applied to an element set surrounding the steel cords, Figure 8-4. The element set was comprised of 3D brick elements with neo-hookean rubber properties. The values for Fa were output for the element set. The left edge of the local model was constrained in all directions. Load is applied to a node set on the right edge in the one direction. For a given value of applied load, the maximum value of Fa was then obtained from the element set.
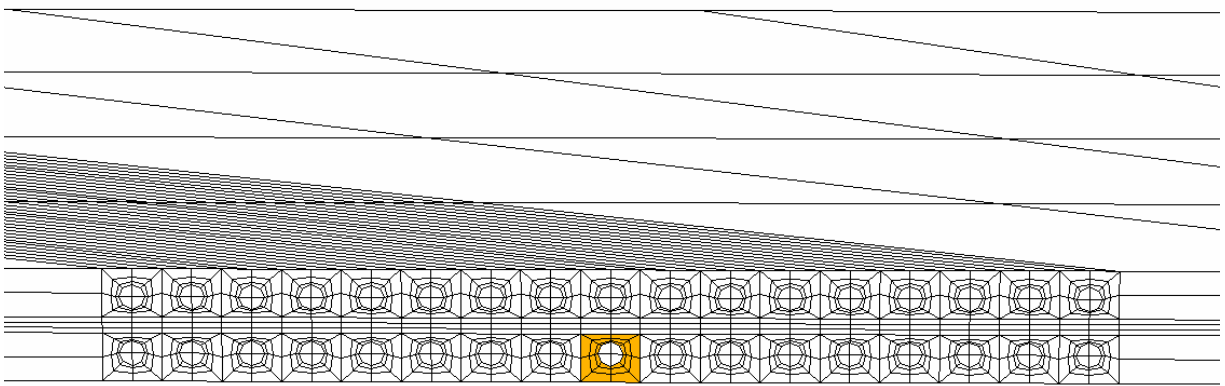
Figure 8-4   **Explicitly defined cords of the local model and the element set for the application of the crack initiation failure criterion.**

8.1.2   Failure function

Several forms of the failure function, Fa, were investigated[73]. They are listed as UVAR(n), where n varyies from 1 to 11, in the UVARM subroutine presented as APPENDIX B. Application of

the UVARM subroutine into the ABAQUS modeling allowed for the testing of different failure functions for the crack initiation criteria. These difference failure functions utilized both stress and strain components. The selection of Fa was based on the following requirements:

- The maximum value of Fa in the element set needed to be close to one, where Fa = 1 defines failure, when the experimental failure load was applied to the model. In order to validate this failure function the failure condition needed to be applicable for both the ±18° and ±45° local 2-ply hybrid models. The respective failure loads, obtained from testing, were 6903 N and 1815 N.

- The failure function had to be coordinate system independent.

The form of the failure function fulfilling the requirements was the maximum principal strain normalized by the experimental strain to failure of compound B:

$$Fa = \frac{\varepsilon_{principal}^{max}}{\varepsilon_{failure}} \qquad [8.2]$$

The values applied to the failure function were determined from the quasi-static testing presented in chapter 4. Since the stresses and strains were outputted as true values by ABAQUS, the strength and strain to failure values used to calculate the value of the failure functions were converted from engineering to second Piola-Kirchoff strains and logarithmic strains.

8.1.3 Calculation of the Number of Cycles for Initiation

The number of cycles for initiation was obtained using the following approach:

- The load was applied to the finite element model for which the number of cycles to initiation was to be predicted.

- The maximum value of *Fa* for the element set was retrieved, Figure 8-4.

The number of cycles for crack initiation was determined from a Fa–N curve of the compound. The Fa-N curve was obtained from the S-N curve for compound B, Figure 5-3. The stresses in the S-N

curve were converted to engineering strains using the modulus data from chapter 4. In doing this conversion the stress-strain curve of compound B was assumed to be linear. Those engineering strains were then converted to logarithmic strains and normalized by the logarithmic strain to failure of compound B to obtain Fa. In this approach it was assumed that during the fatigue of the ASTM D412-D dogbone samples the dominating mechanism was crack initiation, where failure immediately occurred after a crack had initiated. The room temperature unaged Fa-N curve for compound B is presented in Figure 8-5.
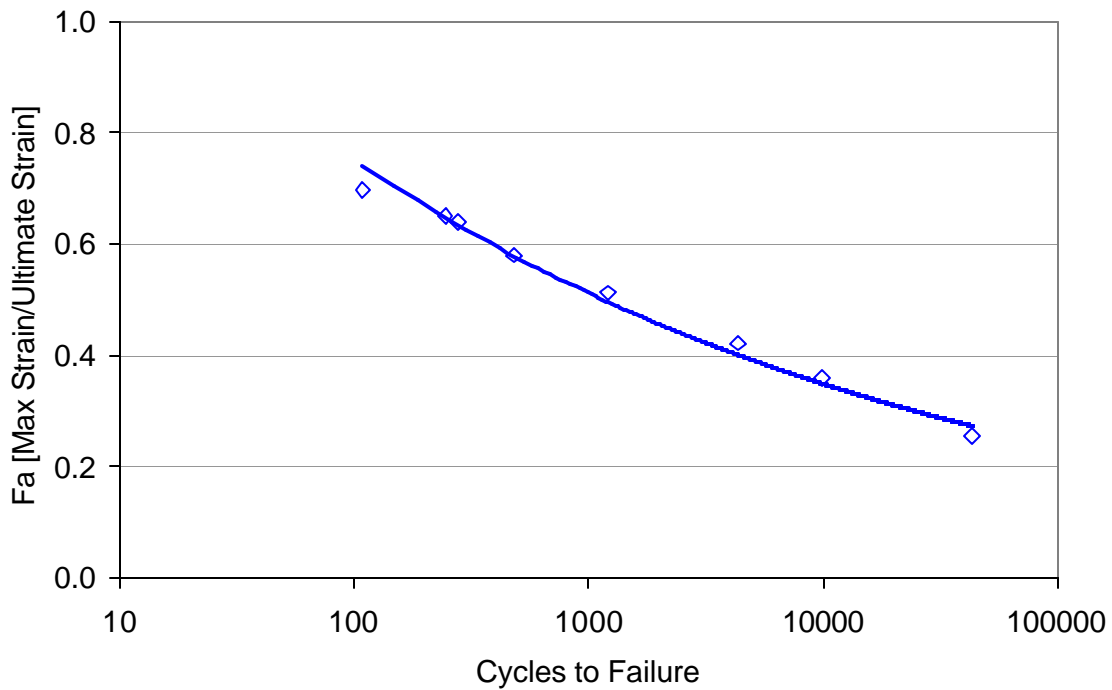
Figure 8-5   Room temperature unaged Fa-N curve for compound B.

For the case of a thermally aged model prediction, the same approach was applied to generate the Fa-N curve; however, the fatigue curves of Figure 5-4 were normalized. Linear interpolation was used to generate the S-N curves between the two limiting aging conditions: unaged and aged for 12

days at 120°C. The curves were then normalized by their respective moduli and strains to failure from the aged quasi-static testing of chapter 4.

8.2   Crack Propagation

The second part of the life prediction implementation was that of the crack propagation analysis. To perform this analysis a coarse mesh hybrid finite element was utilized, Figure 8-6. The model consisted of 3-D brick elements to represent the rubber and membrane elements to represent the reinforcing cord. There were five layers of brick elements to represent the rubber with the center layer being a sacrificial layer. This approach is described in detail in section 8.2.1. To realistically model the testing conditions performed on the 2-ply laminates, load was applied to one end of the model through use of a contact surface while the other end of the model is held rigid in all directions. Use of the contact surfaces at the ends of the model allowed for an accurate modeling of the gripping effect on the reinforcing cords. The total length of the model was the same was the experimental gage length of the 2-ply laminates, 18.89 cm.
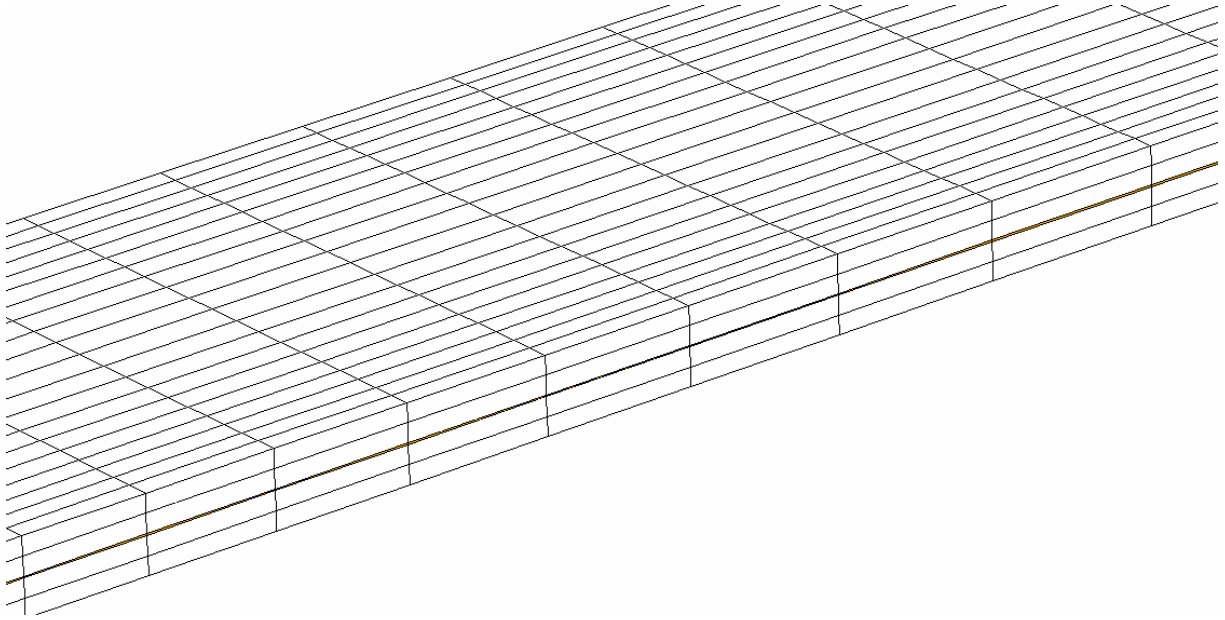
Figure 8-6   **Hybrid off-axis cord-rubber finite element model showing the five layers of rubber.**

8.2.1   2-Ply Laminate Crack Growth Modeling

Crack advancement in the 2-ply laminate model was achieved by removing elements in the sacrificial rubber layer. This approach was applied to realistically model the shape of the interply crack within the laminate. The total thickness of the additional layer was 1.01 x 10^{-4} m. The layer was inserted into a pre-existing finite element model for the 2-ply laminates, given in APPENDIX C. The overall dimensions of the model remained constant. The model was checked to see if the inclusion of the additional layer altered the load deflection behavior of the model. Figure 8-7 shows the comparison of the load deflection behavior between the model with and without the inclusion of the sacrificial layer. No significant effect on the model behavior can be seen. Given this lack of difference in the behavior, and the ability to realistically model the shape of the crack, the sacrificial layer approach was applied to model the crack propagation.
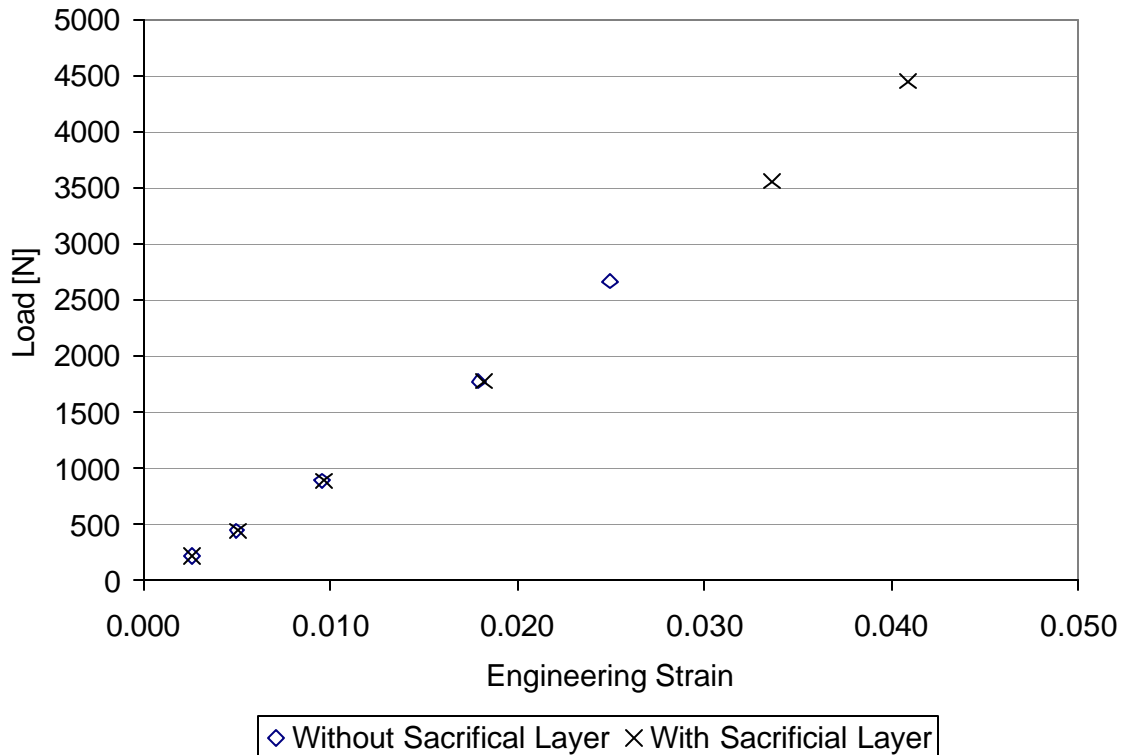
Figure 8-7 **Comparison of the finite element model with and without the inclusion of the sacrificial rubber layer.**

The shape of the crack for the ±18° is shown as the highlighted region in Figure 8-8 and that for the ±45° is shown in Figure 8-9. The shape and size of the modeled crack growth was representative to that revealed through ultrasonic C-Scan, Figure 7-4. The intent was to model the symmetrical interply cracks that dominate the failure of the 2-ply laminate. These regions were divided into 10 steps by which the crack was incrementally driven to coalescence. Failure was defined as the coalescence of the two halves of the crack.
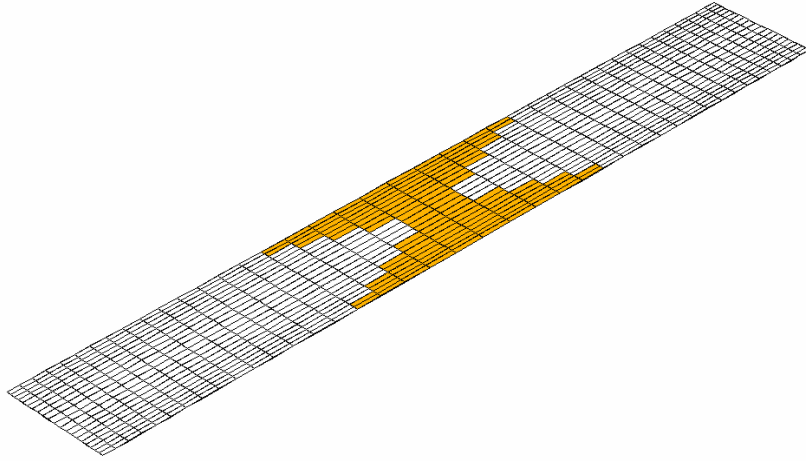
Figure 8-8   **Finite element crack propagation model for the ±18° laminate showing the two penny shaped halves of the crack.**
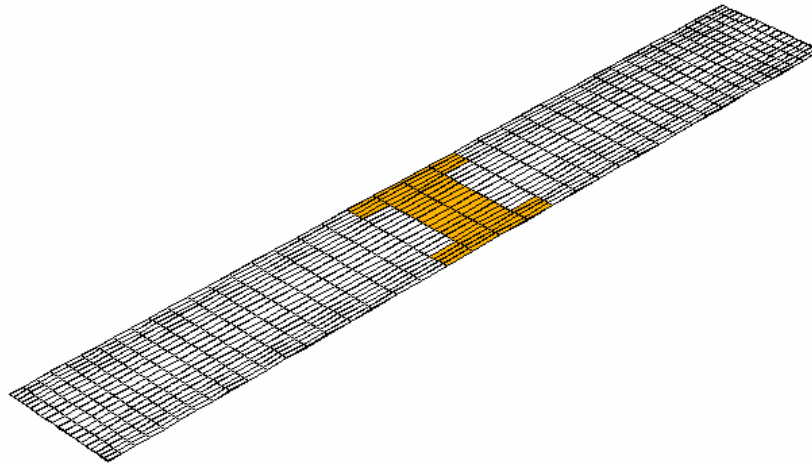
Figure 8-9   **Finite element crack propagation model for the ±45° laminate showing the two penny shaped halves of the crack.**

The approach for the prediction of the number of cycles to failure was accomplished using equation 6.1. Using the sacrificial layer and the ABAQUS, *model change* command, elements were removed to simulate crack growth. The elements were removed in the pattern shown in Figure 8-8 and Figure

8-9. This removal was done uniformly to both sides of the sample. The modified Griffith equation, equation 6.1, was then rewritten as

$$G = \frac{P}{2}\left(\frac{\partial d}{\partial A}\right)_l \qquad [8.3]$$

where δ is the change is the displacement of the rigid surface. For a constant applied load an increase in the damage resulted in the increased elongation of the laminate. The model was run ten times with an increasing level of damage. Thus the crack growth evolved due to the elements being removed. Once the values of ΔG were computed for the different damage states the number of cycles to failure was computed using Paris-Law fits from the DCB and the 2-ply laminate testing. The Paris Law equation was simply rewritten to solve for dN. The value of the number of cycles for crack propagation was the sum of the cycles necessary for the given increments of damage.

8.3   Laminate Predictions

Using the approaches outlined in sections 8.1 and 8.2 predictions have been made on the fatigue lifetime of both the unaged and aged $\pm18°$ and $\pm45°$ 2-ply laminates. The number of cycles for both initiation and propagation were summed to yield the prediction value. The predicted vales and the experimental values from Figure 7-2 and Figure 7-14 were presented and compared. For all the predictions the number of cycles spent in crack initiation was less than 1% of the number of cycles spent in crack propagation. The FEA models were run for the case of an R-ratio of zero.

8.3.1 $\pm18°$ 2-ply laminates

The predicted S-N behavior of the unaged $\pm18°$ 2-ply laminate is shown in Figure 8-10.   The figure shows the predicted behavior based upon the Paris-Law fits to the O'Brien delamination analysis of the 2-ply laminate and the DCB data. The predictions were not in complete agreement with the experimental data. The two predictions essentially bound the experimental data to the left and right. However, the results were in agreement with the expected trends. The DCB prediction substantially over predicted the fatigue life of the laminate. This result was expected from examination of Figure

146

7-13. The crack growth rates obtained from the DCB specimens were approximately an order of magnitude slower than those obtained from the 2-ply laminates, Figure 7-8.
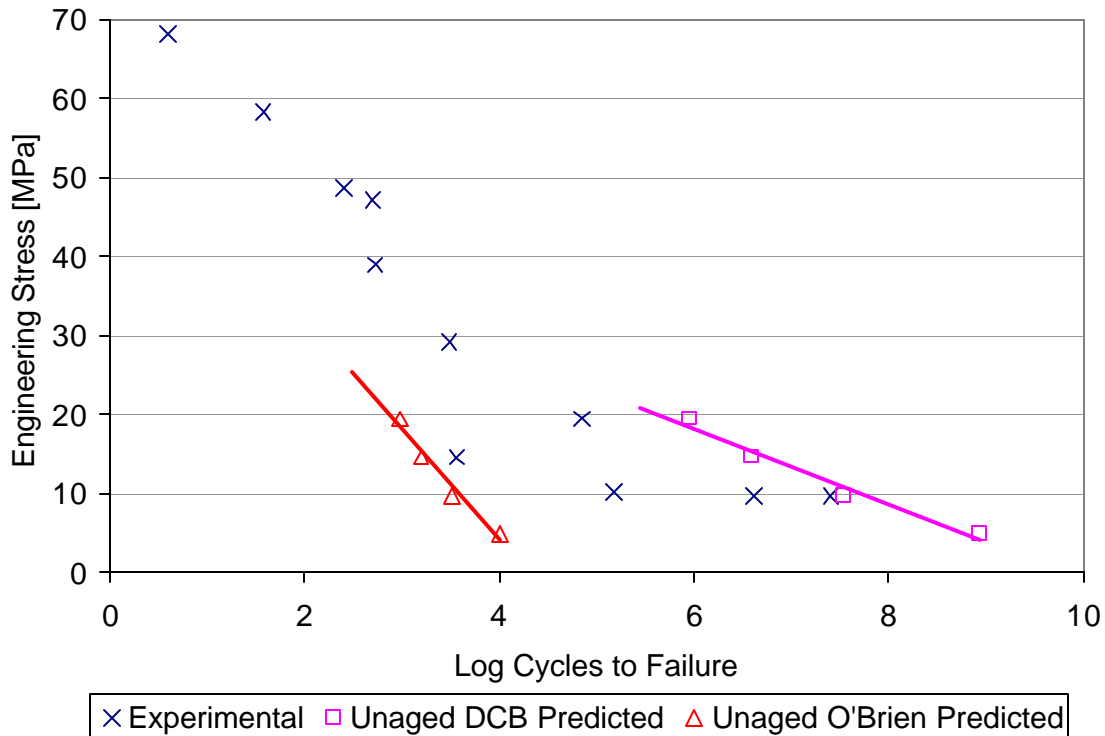
Figure 8-10   Predictions of the number of cycles to failure using a sacrificial layer in the unaged ±18° 2-ply laminate model.

Examination of the slopes of the predicted S-N curves showed that the slope of the O'Brien prediction was the same as that of the experimental data, while the slope of the DCB prediction was shallower than the experimental S-N curve. The difference in the slope can be traced back to the difference in the crack growth rates versus ΔG curves of Figure 7-13. The DCB data had a slightly steeper slope than the 2-ply laminate, and thus a higher value for the Paris-law exponent, β. The fitting parameters α and β applied in the generation of both the unaged and aged ±18° 2-ply laminate predictions are presented in Table 8-1. The difference in the β values between the DCB and the 2-ply

laminate was 2.8 times. When the Paris-Law expression was solved for the number of cycles, dN, the higher value of the exponent in the DCB data fit resulted in a predicted S-N curve with a shallower slope.

Table 8-1   Values of the Paris-Law fitting parameters a and b applied in the generation of both the unaged and aged ±18° 2-ply laminate predictions

	Unaged		Aged 6 Days 100°C	
	DCB	±18° 2-Ply Laminate	DCB	±18° 2-Ply Laminate
Alpha [m² cycles⁻¹]	1×10^{-8}	5×10^{-6}	3×10^{-8}	5×10^{-7}
Beta	2.8	1.055	2.7	1.0688

The predictions for the 6 day 100°C aged 2-ply laminate are presented in Figure 8-11. Similar to the unaged case the DCB data over predicted the fatigue life while the O'Brien prediction under predicted the life. The slope of the O'Brien prediction closely matched that of the experimental data.
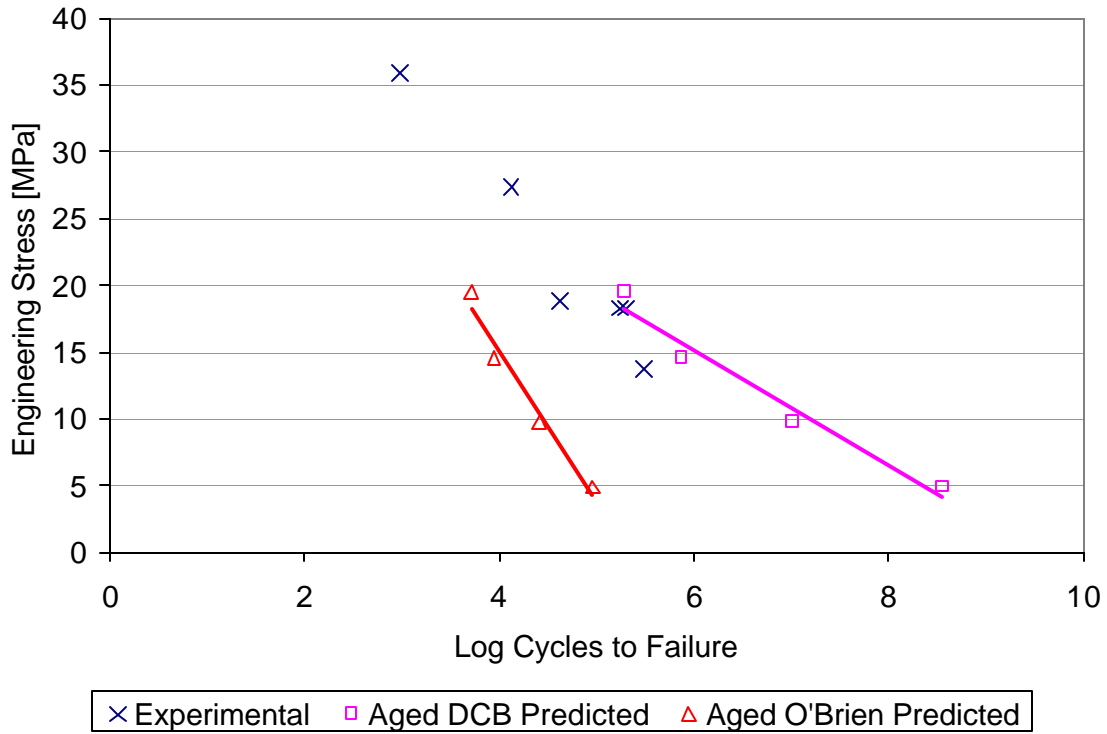
Figure 8-11   Predictions of the number of cycles to failure using a sacrificial layer for the 6 day 100°C ±18° aged 2-ply laminate model.

8.3.2   Sources of Error in the ±18° Predictions

For both the aged and the unaged predictions there was a substantial difference between the predicted and the experimentally observed behavior. The source of the error between the experimental and the predicted behavior lied in either the experimental data or the finite element modeling. Both sources will now be discussed.

8.3.2.1 FEA Model

To assess the validity of the FEA, the model results were compared with the experimental data. Figure 8-12 is the combination of Figure 7-3 and Figure 8-7 showing the predicted and the experimental load versus engineering strain behavior for the ±18° 2-ply laminate. As can be seen the finite element model was much stiffer than the experimental data. For loads below 1800 N the

predicted and the experimental data were not in agreement. At loads higher than 1800 N the predicted and the experimental data are in good agreement, by demonstrating the same slope. At these higher loads the behavior of the ±18° 2-ply laminate was dominated by the pantographing of the steel cords in the direction of the applied load. At lower loads the behavior of the laminate was dominated by the extension of the rubber. The onset of the domination of the pantographing led to the change of slope around 1800 N. This onset was the reason why the O'Brien delamination analysis was carried out for a maximum load of 1780 N. It appeared that the FEA model did not accurately discriminate between these two different regions. The agreement between the slopes of the FEA model and the experimental region dominated by pantographing suggested that the FEA models did not demonstrate the lower rubber dominated region and only captured the higher pantographing dominated region. This domination by the pantographing region accounts for the additional stiffness in the laminate FEA model.
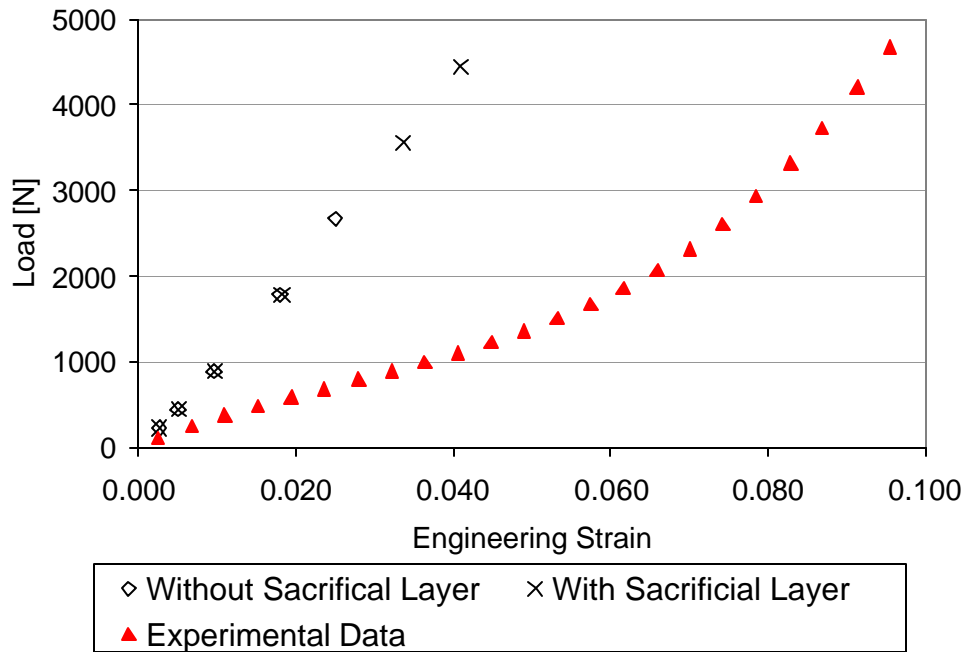
Figure 8-12   Predicted load versus strain behavior of the ±18° 2-ply laminate versus the experimental behavior.

The additional initial stiffness was carried through the delamination modeling for calculating the number of cycles to failure during crack propagation, Figure 8-13. The stiffness from the FEA model correlated to lower values of compliance. When these lower compliance values were inserted into the equation for the strain energy release rate, equation 6.1, the result was a lower value of G. Given that the FEA models are simulating an R-ratio of zero, the calculated value of G was actually the value for ΔG. Substitution of this lower value for ΔG into the Paris-Law resulted in a slower crack growth rate. When the Paris-Law fit was solved for the number of cycles the result was a lower number of cycles for a given value of ΔG. Consequently, the prediction was an under prediction of the experimental S-N curve.
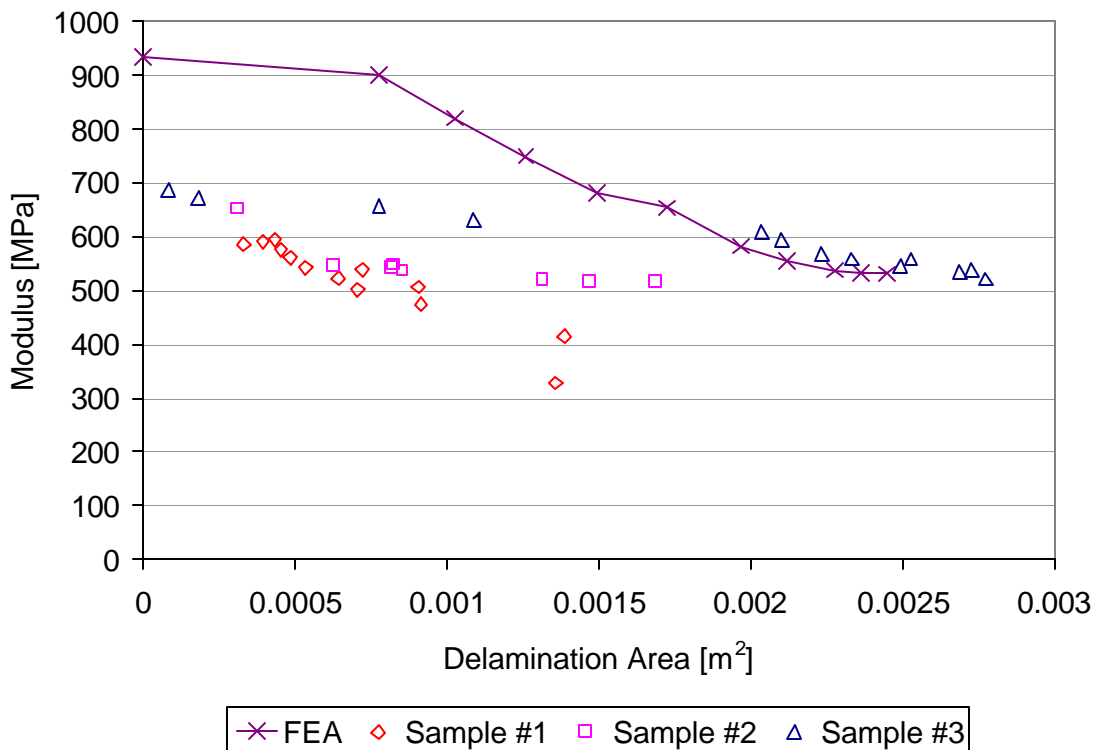
Figure 8-13   **Comparison of the calculated versus the experimental modulus versus delamination area.**

The influence of the effect of additional stiffness on the total prediction was examined. To determine this influence, the experimental modulus versus delamination area behavior of Figure 8-13 was imposed upon the finite element modeling results. Essentially the experimental modulus versus delamination area replaced those values calculated from the FEA. The result was a prediction that demonstrated the same modulus versus delamination area behavior as the experimental data. The application of this technique removed the influence of the additional stiffness in the model predictions. Figure 8-14 contains the new S-N prediction for the unaged ±18° 2-ply laminate based on the fit experimental modulus versus delamination area data.
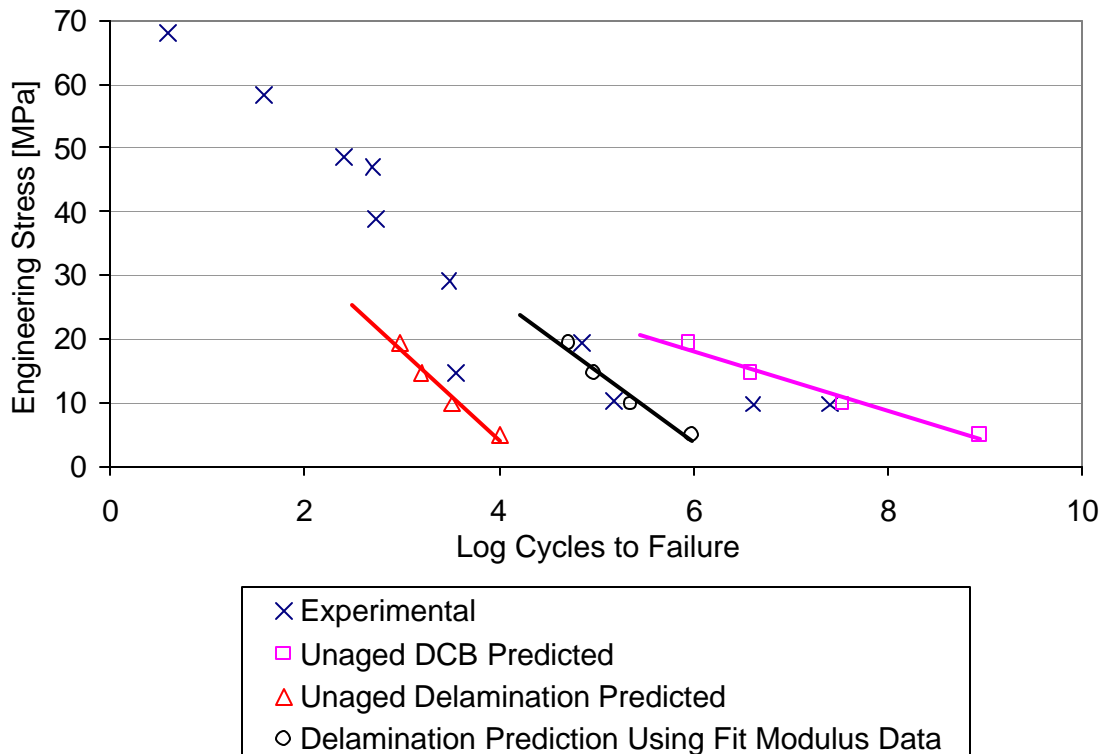
Figure 8-14 **Predictions of the number of cycles to failure of an unaged ±18° 2-ply laminate model with the new S-N prediction for the unaged ±18° 2-ply laminate based on the fit experimental modulus versus delamination area data**

It is seen in the figure that the additional stiffness of the FEA model significantly influenced the S-N prediction. The new prediction based on the fit modulus data is in complete agreement with the experimental S-N curve. The additional stiffness of the model served to reduce the number of cycles to failure for a given stress level by nearly two orders of magnitude. Unfortunately, this prediction based upon the 2-ply crack growth data should agree with the experimental data as the crack growth rate data from the O'Brien delamination analysis is a function of the change in the modulus with the number of cycles, $\frac{dE}{dn}$, as shown in equation 7.4. However, this prediction does serve to validate the results of the O'Brien delamination analysis. An additional source of error may lie in the experimental data of the ±18° 2-ply laminate.

8.3.2.2 Experimental Data

The error in the S-N predictions contributed from the experimental data arose from the crack propagation data. There were other sources of experimental data error such as the ultimate stress, or ultimate strain; however, those values contributed to the crack initiation portion of the prediction which was less than 1% of the number of cycles spent in crack propagation. Consequently, the error in the experimental data most likely arose from the Paris-Law fits of α and β.

The crack growth data of Figure 7-13 was fit to the Paris-Law, power law, expression using MS Excel. When the crack growth data was fit from the DCB testing there was good correlation between the Paris-Law expression and the experimental data. This good correlation was partly a result of there being a large number of data points, with twenty to thirty data points per test, and three tests per condition. However, when the 2-ply laminate crack growth data was fit there were less data points. For the three unaged ±18° 2-ply laminate delamination tests there was a total of sixteen data points that were used to generate the Paris-Law fits, Figure 8-15. The fit of the data with such a low sample size became very dependent upon outliers in the data. These outliers may have contributed to a poor fit of the data. Unfortunately, additional testing of the ±18° 2-ply laminates was not possible due to there being no remaining specimens.

A sensitivity analysis of the fit crack growth data revealed that the predicted number of cycles to failure was heavily dependent upon the values for alpha. An order of magnitude change in alpha resulted in an order of magnitude change in the predicted number of cycles for a given stress level. Changing the value of beta results in changing the slope of the prediction. For good agreement between the predicted and the experimental S-N curve alpha needs to be decreased by two hundred percent. No change in beta is required.
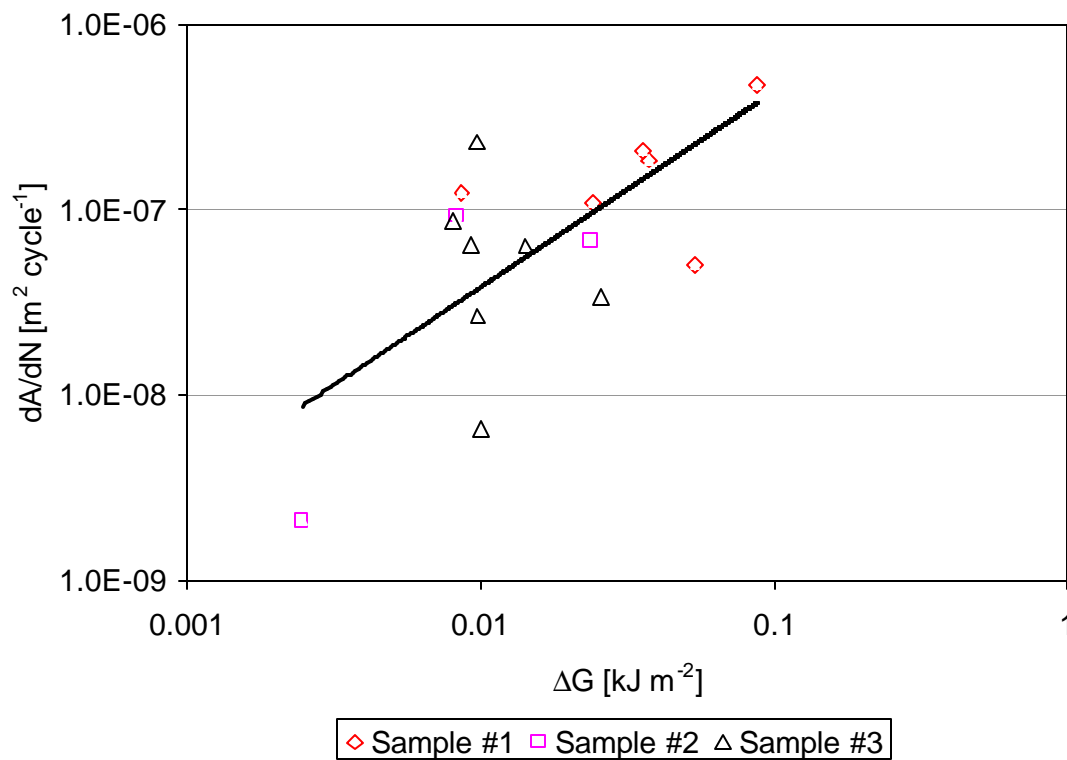
Figure 8-15   Paris-Law fit of the crack growth data for the unaged ±18° 2-ply laminates. The scatter in the data is shown.

8.3.2.3 Additional Source of Error

The first two sources of error were errors that were introduced due to the testing or modeling processes. These two errors arose from sources that could be either corrected or examined by

additional testing. There was one additional source of error that could not be corrected and was not investigated in this research. This source of error was crack coalescence. The predicted S-N curves were based solely upon the summation of the calculated cycles due to crack initiation and crack propagation. Crack coalescence was not investigated in this work due to the complexity of the topic. The inclusion of the number of cycles due to crack coalescence would serve to increase the number of cycles to failure and possibly yield better agreement between the predicted and the experimental S-N curves. This topic of crack coalescence is to be expanded upon in future research.

8.3.3 ±45° 2-Ply Laminates

The predicted S-N behavior of the unaged ±45° 2-ply laminate is shown in Figure 8-16. The figure presents only the predicted behavior based upon the Paris-Law fits to the DCB data. Predictions based upon the O'Brien delamination analysis are not presented because the delamination analysis was not successfully applied to the ±45° 2-ply laminates. The predictions were not in agreement with the experimental data and were much worse than the predictions for the ±18° 2-ply laminate. The result did follow the expected trends, with the DCB prediction substantially over predicting the fatigue life of the laminate and not possessing the same slope as the S-N curve.
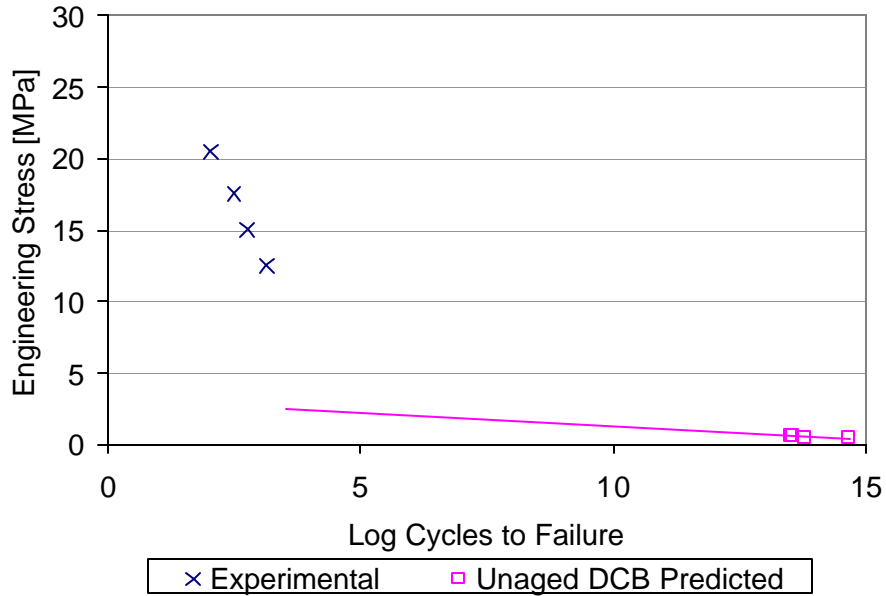
Figure 8-16 **Predictions of the number of cycles to failure using a sacrificial layer for the unaged ±45° 2-ply laminate model.**

8.3.4 Sources of Error in the ±45° Predictions

The errors in the prediction of the ±45° 2-ply laminate were the result of three factors. The first was the additional stiffness of the FEA model when compared to the experimental data, Figure 8-12. The second was the lack of the inclusion of the crack coalescence phenomena in the predicted number of cycles to failure. The third factor was the FEA model itself. Unlike in the case of the ±18° 2-ply laminate model, the ±45° 2-ply laminate model demonstrated significant convergence difficulties. The increased angle of the rebar elements in the model served to increase the overall compliance of the model. Upon an imposed load the increased compliance would result in elements turning themselves inside out in an effort to obtain convergence. The outcome of these convergence difficulties was the prediction being made from very low load levels, Figure 8-16. The model successfully converged in the case of significant delamination only at very low loads e.g. 35 to 58 N. These load values were essentially run-out in a fatigue experiment. Additional fatigue life predictions made at higher load levels

would serve to improve the predicted S-N behavior by representing more realistic testing cases.

9.   CONCLUSIONS

The focus of this research was to investigate the effect of thermal degradation on the mechanical properties of natural rubber compounds and apply those effects to the life prediction of 2-ply cord rubber laminates. The investigation focused on two different natural rubber compounds. Both compounds were 100 percent natural rubber with 65 pphr carbon black. The research into the mechanical properties was divided into two aspects quasi-static and dynamic. The quasi-static properties investigated were the ultimate stress, ultimate strain, shear strength and the modulus. The dynamic properties investigated were the R-ratio, fatigue life and crack growth rates.

9.1   Thermal Aging

A test matrix to track the extent of thermal degradation was developed based upon an industrial accelerated aging test. To track the extent of thermal degradation, the percentages of poly and monosulfidic crosslinks as well as the total crosslink density were determined as functions of time at elevated temperature. Using time temperature superposition with horizontal shifting, a master curve relationship between the chemical variables and the time at elevated temperature was developed to predict real world time scales from laboratory data. The master curve tracked the percentages of poly and monosulfidic crosslinks as functions of time at elevated temperature. It was found that only the percentages of the poly and the monosulfidic crosslinks shifted into a master curve. The total crosslink density did not shift into a master curve. The master curves possessed reasonable shapes with no discontinuities and the shift factor plots were linear functions. Thus is appeared that only one mechanism was occurring during the thermal aging, rubber reversion.

To verify the extent of rubber reversion the levels of soluble polymer were tracked during the thermal aging. It was found that the levels of soluble polymer increased with time at elevated temperature due to reversion of the crosslinked polymer back to the gum rubber state. These soluble

polymer levels shifted into a master curve that contained a reasonable shape with no discontinuities. The shift factor plot for the soluble polymer levels was a linear function. Thus the extent of rubber reversion due to thermal degradation was tracked using a master curve.

9.2   Mechanical Properties

A relationship between the chemical variables and the mechanical properties was developed to predict the properties as functions of the percent poly and monosulfidic crosslinks. It was found that in general polysulfidic crosslinks lead to better mechanical properties. Testing results for the both compounds showed a linear dependence of the ultimate stress, ultimate strain and modulus on the percentage of polysulfidic and monosulfidic crosslinks. The modulus of compound B displayed a linear trend with the percentage total crosslink distribution. Compound A did not exhibit this linear correlation. The difference between the two correlations was attributed to the differences in the area of the carbon black particles in the two compounds. It was suggested that the larger area carbon black particles in compound A may limit the response of the natural rubber due to a higher volume fraction of filler. There was no correlation between either the shear strength or the percent poly, monosulfidic crosslinks and total crosslink density. The use of the master curves with the correlations for the static properties allowed for the prediction of the static properties of the compounds due to any thermal history.

The first half of the dynamic behavior was based on fatigue testing of the compounds to determine the effects of R-ratio and thermal aging on the fatigue life. The tests were performed on die cut sheet stock. It was found that there was a significant R-ratio effect in natural rubber compounds. For R-ratios greater than 0.2 the fatigue life was essentially the same as the creep rupture, R=1.0, behavior. The fatigue tests showed that thermal aging serves to reduce the fatigue life of the compound. This result was the opposite of the observations of Blackman et al.[39], that fatigue life was not necessarily a function of the crosslink type distribution. Aging for 12 day at 120°C reduced the percentage of polysulfidic crosslinks from 70 to 28 percent. Thus it appeared that the crosslink distribution does contribute to the fatigue life of the vulcanizate.

The second half of the dynamic behavior was based on crack propagation experiments. These experiments utilized a double cantilever beam specimen to measure the crack growth rates in compound B. The DCB specimen was applied as it best resembled the structural belts of a tire and provided a constrained crack growth test. This research was the first time this type of specimen has been reported to measure the crack growth in natural rubber compounds. Both fatigue and quasi-static crack growth were examined in thermally aged as well as unaged specimens. It was found that all crack growth was a cohesive failure. The critical strain energy release rate values obtained from the quasi-static crack growth were in accord with values obtained from other techniques.

The dynamic crack growth experiments provided novel results. The crack growth rates were found to be two orders of magnitude faster than those obtained from the traditional testing geometry. This difference was attributed to the plane strain testing state of the DCB rather than the plane stress state of the traditional single edge notch test. An investigation into the possible cavitation of the rubber at the crack tip within the DCB specimen was performed. Using the analysis of Gent et al.[22], it was determined that cavitation should be occurring inside the rubber of the DCB prior to fracture. However, analysis of the failure surfaces did not reveal signs of cavitation. It was concluded that cavitation did not occur in the quasi-static testing of the DCB specimens.

Thermal aging of the DCB specimens was conducted in order to determine the effect of thermal degradation upon the crack growth rates. It was found that the crack growth rates increased with time at elevated temperature. Plots of the crack growth rate versus the change in the strain energy release rate were fit to a Paris-Law expression. The Paris-law fitting parameters, α and β, were correlated with the percentage of polysulfidic crosslinks. It was found that α and β increased as linear functions with the decrease in the percentage of polysulfidic crosslinks. This result was in accordance with the quasi-static testing which found that the better mechanical properties were correlated with higher levels of polysulfidic crosslinks.

With the generation of the data for the aged crack growth rates as function of the crosslink distribution the loop was closed on the degradation of material properties as function of time at elevated

temperature. Application of the master curve allowed for the determination of the percentage of crosslinks after any time and temperature history. With the percentage of the crosslink known, the value of the quasi-static and the dynamic mechanical properties could be determined from the correlated data. Insertion of these degraded mechanical properties into the finite element models allowed for the prediction fatigue lifetime of the 2-ply laminate.

In order to verify the prediction from the finite element models, off axis 2-ply cord-rubber laminates were fatigued until failure and their crack growth rates were determined. The delamination approach of O'Brien [81-85] was applied to determine the crack growth rates of the delamination within the 2-ply laminates. This research is the first time this delamination approach has been applied to non-linear cord-rubber composite laminates. The growth of the delamination area was tracked in accordance with the reduction of the composite modulus as a function of cycles. The delaminated area of the laminate was determined using ultrasonic C-scan and the modulus was determined from the load deflection behavior of the laminate. It was found that the delamination approach successfully predicted the modulus of the laminates in the presence of delamination as well as determining the crack growth rates of the delamination within the laminate. This approach was applied to both unaged and thermally aged 2-ply laminates. The effect of aging on the 2-ply laminates was found to be in accordance with those results obtained from the DCB specimens. The crack growth data was used in conjunction with the aged material data in the finite element life predictions.

9.3   Finite Element Analysis

Lifetime predictions of two off axis 2-ply cord-rubber laminates were performed using finite element analysis. Predictions were made in the case of an ±18° 2-ply laminate and a ±45° 2-ply laminate. For the purposes of the analysis, the lifetime prediction approach was discretized into two sections: crack initiation and crack propagation. In the crack initiation analysis a residual strength approach was applied to determine the number of cycles. This approach utilized a maximum strain failure function and was applied to a refined local hybrid finite element model. The local model was applied because crack initiation was driven by local stresses and strains.

161

The crack propagation analysis utilized a global finite element model of the 2-ply laminates with a fracture mechanics approach. An additional layer of rubber was inserted into the center of the model. Removing elements from this additional layer of rubber simulated the growth of the crack. The crack area was tracked in conjunction with the global strain of the model to calculate the strain energy release rate. The crack growth rates from both the DCB and the 2-ply delamination analysis were applied to generate the predicted S-N curves. Predictions were made for both the unaged and the thermally aged case.

The predicted S-N curved did not completely agree with the experimental data, but did demonstrate expected trends. The prediction from the 2-ply delamination analysis greatly under predicted the lifetime of the laminates but did possess the same slope as the experimental S-N curve. The DCB prediction over predicted the lifetimes and demonstrated a much shallower slope.

9.4   Summary

The focus of this research was to investigate the effect of thermal degradation upon the mechanical properties of natural rubber compounds and apply those effects to the life prediction of 2-ply cord rubber laminates. The extent of rubber reversion in a natural rubber compound was successfully tracked and correlated with the degraded mechanical properties of the compound. The degraded material properties were applied to finite element models and predictions were made. While there was not complete agreement between the predicted and the experimental data, this dissertation outlines a comprehensive approach to track the effects of thermal degradation and apply those effects to a real world application.

In performing this research there have been four significant contributions to the literature. The first is the tracking of the percentage of crosslinks with time at elevated temperature through the application of a master curve. The second is the correlation of those percentages of crosslinks with the degraded static and dynamic mechanical properties. Third is the use of a DCB to measure the crack growth in natural rubber. The fourth is the application of the O'Brien delamination approach to non-linear 2-ply cord-rubber composites.

9.1   Future Work

From this work there is the potential for future work from which this research can be built upon.

Future work should be performed which focuses on the error between the experimental modulus and the modulus from the global finite element model. The difference between the experimental and the FEA needs to be rectified.

Further quasi-static testing of the thermally aged compounds could be performed to refine the relationships between the percentage crosslinks and the mechanical properties. Such supplemental testing would serve to provide better finite element model inputs.

Given that there is a significant R-ratio effect in natural rubber, the crack growth testing can be performed under different R-ratios. Crack growth testing could also be performed at elevated temperatures to determine its effects.

Another area for future work is the generation of additional crack growth data from the 2-ply laminates. A larger sample size of data would serve to increase the correlation between the Paris-Law fits and the experimental crack growth data.

The modeling in this research only investigated one thermal aging condition for the 2-ply laminates. Since the master curves allow for determination of the percentage of crosslink for any thermal history, predictions should be made for different thermal histories. These thermal histories may include step effects.

The predictions show that the approach and techniques applied so far in this dissertation are reasonable. However, a feature that is missing from these predictions is the number of cycles spent during the progression of damage from initiation to the beginning of propagation e.g. crack coalescence. The inclusion of this feature would serve to better the predictions. This topic alone is a dissertation in itself.

10.   REFERENCES

1   Rivlin R.S., Thomas A.G. "Rupture of Rubber. I. Characteristic Energy for Tearing," *Journal of Polymer Science*, **10**, 3, 1953 pp. 291-318

2   Greensmith H.W. "Rupture of Rubber. X. The change in Stored Energy on Making a Small Cut in a Test Piece Held in Simple Extension," *Journal of Applied Polymer Science*, **7**, 1963, pp. 993-1002

3   Gent A.N., Lindley P.B., Thomas A.G. "Cut Growth and Fatigue of Rubbers. I. The Relationship Between Cut Growth and Fatigue," *Journal of Applied Polymer Science*, **8**, 1964 pp. 455-466

4   Lake G.J., Lindley P.B. "Cut Growth and Fatigue of Rubbers. II. Experiments on Noncyrstallizing Rubbers," *Journal of Applied Polymer Science*, **8**, 1964 pp. 707-721

5   Lake G.J., Lindley P.B. "The Mechanical Fatigue Limit for Rubber," *Journal of Applied Polymer Science*, **9**, 1965 pp. 1233-1251

6   Lake G.J. "Mechanical Fatigue of Rubber," *Division of Rubber Chemistry, American Chemical Society, Cleveland, Ohio, October 12-15*, 1971 pp. 309-328

7   Lake G.J. "Aspects of Fatigue and Fracture of Rubber," *Progress of Rubber Technology*, 1983 pp 89-143

8   Young D.G. "Fatigue Crack Propagation in Elastomer Compounds: Effects of Strain Rate, Temperature, Strain Level and Oxidation," *Rubber Division, American Chemical Society, New York, N.Y. April 8-11*, 1986 pp. 809-825

9   Bathias C., Legorju-Jago K. "Fatigue Initiation and Propagation in Natural and Synthetic Rubbers," Presented at the 2nd International Conference on Fatigue, Williamsburg, VA, June, 2000

10 Shen Y., Golnaraghi M.F., Plumtree A. "Compressive Cyclic Stress-Strain Behavior of Structural Foam," Submitted to the *International Journal of Fatigue*, NA 214, 2000

11 Lefebvre D.R., Dillard D.A., Brinson H.F. "The Development of a Modified Double-Cantilever-Beam Specimen for Measuring the Fracture Energy of Rubber to Metal Bonds," *Experimental Mechanics*, **28**, 1, 1988 pp. 38-44

12 Lake G.J., Thomas A.G. "," *Proceeding from the Royal Society*, **a300**, 1967 pp.108

13 Lake G.J., Clapson B.E. "Truck Tyre Groove Cracking Theory and Practice," *Rubber Journal*, December, 1970 pp. 36-49

14 Lindley P.B. "Energy for Crack Growth in Model Rubber Components," *Journal of Strain Analysis*, **7**, 2, 1972 pp. 132-140

15 Gent A.N., Marteny P. "Crack Velocities in Natural Rubber," *Journal of Materials Science*, **17**, 1982 pp. 2955-2960

16 Rivlin R.S., Thomas A.G. "The Effect of Stress Relaxation on the Tearing of Vulcanized Rubber," *Engineering Fracture Mechanics*, **18**, 2, 1983 pp. 389-401

17 Lee D.J., Donovan J.A. "Critical J-Integral and Tearing Energies for Fracture of Reinforced Natural Rubber," *Theoretical and Applied Fracture Mechanics*, **4**, 1985 pp. 137-147

18 Lee D.J., Donovan J.A. "Mixed Mode I and II Fracture of Carbon Black Filled Natural Rubber," *Journal of Fracture*, **34**, 1987 pp. 41-55

19 Dragoni E., Medri G. "Fracture Toughness Evaluation of Natural Rubber," *Theoretical and Applied Fracture Mechanics*, **10**, 1988 pp. 79-83

20 Sumner A.J.M., Kelbch S.A., Eisele U.G., AG Bayer "Crack Growth Performance of Tire Compounds," *Rubber World*, **213**, 2, 1995 pp. 38-45

21 Neumeister L.A., Koenig J.L. "Crack Analysis of Unfilled Natural Rubber Using Infrared Microspectroscopy," *PMSE: Polymeric Materials Science and Engineering*, **74**, 1996 pp. 266-267

22 Gent A.N., Razzaghi-Kashani M. "Energy Release Rate for a Crack in a Tilted Block," Submitted for publication in *Rubber Chemistry and Technology*, 2000

23 Treloar L.R.G The Physics of Rubber Elasticity, 2nd Ed., Oxford University Press, Oxford, 1958

24 Neogi C., Basu S.P., Bhowmick A.K. "Analysis of Rubber-Filler Interaction at High Temperature by Using Strain Amplification Factor," *Plastics and Rubber Processing and Applications*, **12**, 1989 pp. 147-151

25 Chung B., Funt J.M, Ouyang G.B. "Effects of Carbon Black on Elastomer Ultimate Properties – IR Compunds," *Rubber World*, **204**, 1991 pp. 46-51

26 Wang M.J. "Effect of Polymer-Filler and Filler-Filler Interactions on Dynamic Properties of Filled Vulcanizates" *Rubber Chemistry and Technology*, **71**, 1998 pp. 520-589

27 Lake G.J., Lindley P.B., "Ozone Cracking, Flex Cracking and Fatigue of Rubber," *Rubber Journal*, November, 1964 pp. 30-39

28 Thomas A.G., Whittle J.M. "Tensile Rupture of Rubber," *Division of Rubber Chemistry, Rubber Chemistry and Technology*, Buffalo, New York, October 14-17, 1969 pp.222-228

29 Goritz D., Kiss M. "On the Origin of Strain-Induced Crystallization," *Rubber Chemistry and Technology*, **59**, 1985, pp. 40-45

30 Allegra G., "Strain-Induced Crystallization in Rubbers," *Polymer Preprints*, **26**, 2, 1985 pp. 42

31 Allegra G., "Strain-Induced Crystallization in Rubber," *Rubbercon*, 1987 pp. 21A/1 – 21A/7

32 Flory P.J., *Journal of Chemical Physics*, **15**, 1947 pp.397

33 Braden M., Gent A.N., *Journal of Applied Polymer Science*, **3**, 1960 pp. 90-99

34 Braden M., Gent A.N., *Journal of Applied Polymer Science*, **3**, 1960 pp. 100

35 Lake G.J., Lindley P.B. "Role of Ozone in Dynamic Cut Growth of Rubber," J*ournal of Applied Polymer Science*, **9**, 1965 pp. 231-2054

36 Braden M., Gent A.N., *Journal of Applied Polymer Science*, **62**, 1962 pp. 449-455

37 Huang C., Fan R., Zhang Y., Zhang Y. "Effet of Aging on NR Vulcanizates," *He Cheng Xiang Jiao Gong Ye: China Synthetic Rubber Industry*, **23**, 5, 2000 pp. 288-290.

38 Lyubchanskaya L.I., Kuzminski A.S. "The Degradation of Main Chains and Crosslinks in the Aging of Vulcanizates," *Doklady Akad. Nauk SSSR*, **135**, 1960 pp. 1438-1438

39 Blackman E.J., McCall E.B. "Relationship Between the Structures of Natural Rubber Vulcanizates and Their Thermal and Oxidative Aging," *Division of Rubber Chemistry, Rubber Chemistry and Technology*, Buffalo, New York, October 14-17, 1969 pp.651-661

40 Nasir M., The G.K "The Effects of Various Types of Crosslinks on the Physical Properties of Natural Rubber," *European Polymer Journal*, **24**, 8, 1988 pp. 733-736

41 Bristow G.M., "Influence of Grade of Natural Rubber on Reversion Behavior," *Journal of Natural Rubber Research*, **6**, 3, 1991 pp. 137-151

42 Sloan J.M. "Reversion Studies of Natural and Guayule Rubbers," *U.S. Army Materials Technology Laboratory: Polymer Research Branch*, August, 1992 pp. 1-9

43 Padovan J., Padovan P., Kazempour A. "Spinup Wear in Aircraft Tires," *Tire Science and Technology*, **21**, 3, 1993 pp. 138-162

44 Rimondi G., Toth W.J., Kounavis J. "Predictive Model for Reversion-Type Cures," *Tire Science and Technology*, **24**, 1, 1996 pp. 77-91.

45 Ismail H., Anuar H., Tsukahara Y. "Effects of Palm Oil Fatty Acid on Curing Characteristics, Reversion and Fatigue Life of Various Natural Rubber Compounds," *Polymer International*, **48**, 1999 pp. 607-613

46 Mitchell G.R. "A Wide-Angle X-Ray Study of the Development of Molecular Orientation in Crosslinked Natural Rubber," *Polymer*, **25**, 11, 1984 pp. 1562-1572

47 Dubault A., Delocke B., Herz J. "Effect of Crosslinking Density on the Orientational Order Generated in Strained Networks: A Deuterium Magnetic Resonance Study," *Polymer*, **25**, 10, 1984 pp. 1405-1410

48 Windle, A. "Stress Induced Orientation in Polymers, Models for Stress-Orientation-Strain Relationships," pp. 161-162

49 Mitchell G.R., Brown D.J., Windle A.H. "The Interpretation of Orientation-Strain Relationships in Rubbers and Thermoplastic," *Polymer*, **36**,1985 pp1755-1762

50 Mitchell G.R. "Orientation-Strain Behavior of Crosslinked Rubbers," *British Polymer Journal*, **17**, 2, 1985 pp. 111-115

51 Ziabicki A., Walasek J. "Molecular Models of Polymer Networks and Constitutive Equations of Rubber Elasticity," *British Polymer Journal*, **17**, 2, 1985 pp.116-121

52 Amram B., Bokobza L., Queslel J.P., Monnerie L. "Fourier-Transform Infra-Red Dichroism Study of Molecular Orientation in Synthetic High cis-1,4-Polyisoprene and in Natural Rubber," *Polymer*, **27**, 1986 pp. 877-882

53 Abramchuk S.S., Nyrkova I.A., Khokhlov A.R. "An Elasticity Theory of Rubbers With Orientational Interactions," *Polymer Science U.S.S.R.*, **31**, 8, 1989 pp. 1936-1945

54 Udagawa Y., Ito M. "Detection of the Molecular Orientation in Nonvulcanized and Vulcanized Natural Rubber Compounds by the Low-Temperature X-Ray Method," *Rubber Chemistry and Technology*, **62**, 1989 pp. 179-195

55 Queslel J.P., Monnerie L., Erman B. "Characterization of Segmental Orientation in Stretched Rubbery Networks by the Stationary Fluorescence Polarization Technique," *Journal of Macromolecular Science and Chemistry A*, **26**, 1, 1989 pp 93-123

56 Roland C.M., Santangelo P.G., Choi I.S., Miller J.B. "Orientation and Mechanical Response of Elastomers Containing Double Networks," *Polymeric Materials Science and Engineering; American Chemical Society*, **68**, 1993 pp. 276-277

57 Xingfa M., Chongguang W. "Indirect Evidence on Molecular Orientation Behavior of Metal-to-Rubber Adhesive Bonding in Vulcanization," *PMSE: Polymeric Materials, Science & Engineering*, **10**, 5, 1994 pp. 132-135

58 Fleischman T., The Goodyear Tire and Rubber Company, personal communication, 2000

59 Breidenbach R.F., Lake G.J. "Mechanics of Fracture in Two-Ply Laminates," *Rubber Chemistry and Technology*, **52**, 1979, pp 96-109

60 Gent A.N., Fielding-Russell G.S., Livingston D.I., Nicholson D.W. "Failure of Cord-Rubber Composites by Pull-Out of Transverse Fracture," *Journal of Materials Science*, **16**, 1981 pp. 949-956

61 Parhizgar S., Weissman E.M., Chen C.S. "Determination of Stiffness Properties of Single-Ply Cord-Rubber Composites," *Tire Science and Technology*, **16**, 2, 1988 pp. 118-126

62 Huang Y.S., Yeoh O.H. "Crack Initiation and Propagation in Model Cord-Rubber Composites," *Rubber Division, American Chemical Society, Cincinatti, Ohio, October 18-21*, 1988 pp. 709-731

63 Lee B.L., Liu D.S. "Cumulative Damage of Fiber-Reinforced Elastomer Composites under Fatigue Loading," *Journal of Composite Materials*, **28**, 13, 1994 pp. 1261-1286

64 Pidaparti R.M.V., Liu Y. "Free Vibration of Cord-Rubber Composite Laminates," *Journal of Sound and Vibration*, **197**, 3, 1996, pp. 373-380

65 Pidaparti, R.M.V. "Analysis of Cord-Rubber Composite Laminates Under Combined Tension and Torsion Loading," pp. 433-438

66 Pidaparti R.M.V. "Torsional Analysis of a Steel Cord-Rubber Tire Belt Structure," *Tire Science and Technology*, **24**, 4, 1996 pp. 339-348

67 Martin R.H. "Incorporating Interlaminar Fracture Mechanics Into Design," *Proc. Instn. Mech. Engrs.*, **214**, L 2000 pp. 91-97

68 "The Vanderbilt Rubber Handbook 13th Edition," Robert F. Ohm Editor, R.T. Vanderbilt Company Inc., Norwalk, CT, 1990, pp 600-607.

69 "The Vanderbilt Rubber Handbook 13th Edition," Robert F. Ohm Editor, R.T. Vanderbilt Company Inc., Norwalk, CT, 1990, pp 416-417.

70 Natural Rubber Science and Technology, Ed by A D Roberts, Chapter 12 Sulphur Vulcanization Chemistry p. 526

71 Gundert F., Wolf B.A. "Polymer-Solvent Interaction Parameters," Polymer Handbook, VII, pp 173-182

72 Kraus G. "Degree of Cure in Filler-Reinforced Vulcanizates by the Swelling Method-I," *Rubber World*, October, 1956 pp. 67-73

73 Duthoit J., Virginia Tech, personal communication, 2000

74 Fleischman T., The Goodyear Tire and Rubber Company, personal communication, 2000

75 Kinlock A.J., Adhesion and Adhesives: Science and Technology, Chapman & Hall, New York, 1987

76 Dillard D.A., Lesko J.J., "Mechanics of Adhesive Bonding," <u>3M Short Course</u>, Virginia Tech March 2000

77 Gent A.N., Meinecke E.A., "Compression, Bending and Shear of Bonded Rubber Blocks," *Polymer Enginering and Science*, **10**, 1, Jan 1970

78 Gent A.N., Henry R.L., Roxburg M.L., "Interfacial Stresses for Bonded Rubber Blocks in Compression and Shear," *Journal of Applied Mechanics*, **855**, Dec 1974

79 Gent A.N., Lindley P.B., "Internal Rupture of Bonded Rubber Cylinders in Tension," *Proceedings of the Royal Sociey of London: Series A*," **A249**, No. 1257, 1959 pp.195-205.

80 Gent A.N, The Goodyear Tire and Rubber Company, personal communication, 2001

81 O'Brien T.K.; "Analysis of Local Delaminations and Their Influence on composite Laminate Behavior;" <u>Delamination and Debonding of Materials, ASTM STP 876</u>, 1985 pp. 282-297.

82 O'Brien T.K., Hooper S.J.; "Local Delamination in Laminates with Angle Ply Matrix Cracks, Part I: Tension Tests and Stress Analysis;" <u>Composite Materials: Fatigue and Fracture, ASTM STP 1156</u>, **4**, 1993 pp. 491-506.

83 O'Brien T.K.; "Local Delamination in Laminates with Angle Ply Matrix Cracks, Part II: Delamination Fracture Analysis and Fatigue Characterization;" <u>Composite Materials: Fatigue and Fracture, ASTM STP 1156</u>, **4**, 1993 pp. 507-538.

84 O'Brien T.K.; "Characterization of Delamination Onset and Growth in a Composite Laminate," <u>Damage in Composites: ASTM STP 775</u>, 1982, pp. 140-167.

85 O'Brien T.K.; "Generic Aspects of Delamination in Fatigue of Composite Materials," *Journal of the American Helicopter Society*, 1987 pp. 13-18.

86 Andonian, A. 1999 "Effect of Sample Geomerty on Mechanical Characteristics of Cord/Rubber Composites," *ASC 14th Annual Technical Conference, Blacksburg, VA, June 1999*.

87 Example 2020301.inp, <u>ABAQUS 5.8 Standard Example Problems Files</u>, Hibbitt, Karlsson & Sorensen, Inc., Pawtucket, RI, 1998

88 Reifsnider K.L., Stinchcomb W.W.; "A Critical Element Model of the Residual Strength and Life of Fatigue-Loaded Composite Coupons;" <u>Fatigue and Fracture, ASTM STP 907</u>, (1986) pp.298-303.

89 Broutman L.J., Sahu S.; "A New Damage Theory to Predict Cumulative Fatigue Damage in Fiberglass Reinforced Plastics;" Testing and Design 2nd Conference, ASTM STP 497, (1972) pp.170-188.

11. APPENDIX A

TABLES OF AGED COMPOUND A AND COMPOUND B CURVE FITS

Compound A

Mechanical Property	Polysulfidic Crosslinks		Monosulfidic Crosslinks		Total Crosslink Density	
	Slope	Intercept	Slope	Intercept	Slope	Intercept
Ultimate Stress [MPa]	0.0958	9.6581	0.0885	11.342	-1.1762	18.993
Ultimate Strain	0.0048	2.5647	0.0053	2.6235	-0.0752	3.1014
Modulus [MPa]	0.0293	3.4455	0.0276	3.9466	-0.2834	5.9708
Shear Strength [MPa]	-0.0037	46.725	0.0276	45.95	-0.4925	48.637

Compound B

Mechanical Property	Polysulfidic Crosslinks		Monosulfidic Crosslinks		Total Crosslink Density	
	Slope	Intercept	Slope	Intercept	Slope	Intercept
Ultimate Stress [MPa]	0.1585	7.6272	-0.1276	18.417	3.1686	3.1782
Ultimate Strain	0.0091	2.6322	-0.1994	3.6592	-0.0037	3.1208
Modulus [MPa]	0.0379	3.292	-0.0368	6.1006	1.3715	0.1634
Shear Strength [MPa]	-0.0045	40.108	-0.0033	39.933	-1.0675	43.854
C_{10} [MPa]	0.0113	0.9797	-0.0114	1.8303	0.4511	-0.0957

12.   APPENDIX B

ABAQUS UVARM

*USER SUBROUTINE
C
```
      SUBROUTINE UVARM(UVAR,DIRECT,T,TIME,DTIME,CMNAME,ORNAME,
     1 NUVARM,NOEL,NPT,LAYER,KSPT,KSTEP,KINC,NDI,NSHR)

      INCLUDE 'ABA_PARAM.INC'

C     PARAMETER(A=19d6*3.8)
C     PARAMETER(B=37d6*4.5)
      PARAMETER(PaPsi=1.450377377d-4)
      DIMENSION UVAR(NUVARM),DIRECT(3,3),T(3,3),TIME(2)
      DIMENSION ARRAY(15),JARRAY(15)
      CHARACTER*8 CMNAME,ORNAME,FLGRAY(15)
      REAL*8 eF,eFTrue,X,Xtrue,sF,sFTrue,S,STrue

C eps_tens_failure= 380% = 156.86% true
C X= 19MPa = 91.2MPa true = 13227.44psi true
C sigs_shear_failure= 450% (guess)= 170.47% true
C S= 37MPa = 203.5MPa true = 29515.18psi true

      eF=2.8
      eFTrue=LOG(eF+1)
      X=17d6
      XTrue=X*(1+eF)*PaPsi
      sF=4.0
      sFTrue=LOG(sF+1)
      S=37d6
      STrue=S*(1+sF)*PaPsi

C GET STRESSES
      CALL GETVRM('S',ARRAY,JARRAY,FLGRAY,JRCD)
      JERROR=JERROR+JRCD
      S11=ARRAY(1)
      S22=ARRAY(2)
      S33=ARRAY(3)
      S12=ARRAY(4)
      S23=ARRAY(5)
      S31=ARRAY(6)
```

```fortran
C GET STRAINS
      CALL GETVRM('E',ARRAY,JARRAY,FLGRAY,JRCD)
      JERROR=JERROR+JRCD
      E11=ARRAY(1)
      E22=ARRAY(2)
      E33=ARRAY(3)
      E12=ARRAY(4)
      E23=ARRAY(5)
      E31=ARRAY(6)

C GET PRINCIPLE STRAINS
      CALL GETVRM('EP',ARRAY,JARRAY,FLGRAY,JRCD)
      JERROR=JERROR+JRCD
      EMIN=ARRAY(1)
      EINT=ARRAY(2)

C GET ENERGY
      CALL GETVRM('ENER',ARRAY,JARRAY,FLGRAY,JRCD)
      JERROR=JERROR+JRCD
      SED=ARRAY(1)

      UVAR(1)=SED/3900
      UVAR(2)=EMAX/eFTrue

      RETURN

            END
```

13.   APPENDIX C

ABAQUS 2-PLY LAMINATE INPUT FILE

```
*Heading
2-Ply Cord Rubber Composite
**
** units in the model are in inches and pounds
**
*node, nset=start
1,  0.0, 0.0, 0.0
2,  0.0, 0.034683, 0.0
3,  0.0, 0.069366, 0.0
4,  0.0, 0.072366, 0.0
5,  0.0, 0.107049, 0.0
6,  0.0, 0.141732, 0.0
**
*node, nset=middle
61,  0.5, 0.0, 0.0
62,  0.5, 0.034683, 0.0
63,  0.5, 0.069366, 0.0
64,  0.5, 0.072366, 0.0
65,  0.5, 0.107049, 0.0
66,  0.5, 0.141732, 0.0
**
*node, nset=end
121,  1.0, 0.0, 0.0
122,  1.0, 0.034683, 0.0
123,  1.0, 0.069366, 0.0
124,  1.0, 0.072366, 0.0
125,  1.0, 0.107049, 0.0
126,  1.0, 0.141732, 0.0
**
*nfill, bias=0.95, nset=end1-1
start, middle, 10, 6
**
*nfill, bias=1.05, nset=end1-2
middle, end, 10, 6
**
**
*nset, nset=end1
end1-1, end1-2
**
```

** FILLING IN THE NODES INTO THE THIRD DIMENSION
**
*ncopy, change number=4000, shift, old set=end1, new set=end2-1
0., 0., 3.64173
0.,0.,0.,0.,0.,0.,0.
*nfill, nset=nall-1, bias=0.95
end1, end2-1, 20, 200
**
*ncopy, change number=4000, shift, old set=end2-1, new set=end2
0., 0., 3.64173
0.,0.,0.,0.,0.,0.,0.
*nfill, nset=nall-2, bias=1.05
end2-1, end2, 20, 200
**
*nset, nset=nall
nall-1, nall-2
**
*element, type=c3d8h
1, 1, 201, 207, 7, 2, 202, 208, 8
2, 2, 202, 208, 8, 3, 203, 209, 9
3, 3, 203, 209, 9, 4, 204, 210, 10
4, 4, 204, 210, 10, 5, 205, 211, 11
5, 5, 205, 211, 11, 6, 206, 212, 12
*element, type=m3d4, elset=ply1
4001, 2, 202, 208, 8
*element, type=m3d4, elset=ply2
5001, 5, 205, 211, 11
**
*elgen, elset=layer1r
1, 1, 1, 1, 20, 6, 5, 40, 200, 100
*elgen, elset=layer2r
2, 1, 1, 1, 20, 6, 5, 40, 200, 100
*elgen, elset=removal
3, 1, 1, 1, 20, 6, 5, 40, 200, 100
*elgen, elset=layer3r
4, 1, 1, 1, 20, 6, 5, 40, 200, 100
*elgen, elset=layer4r
5, 1, 1, 1, 20, 6, 5, 40, 200, 100
**
*elgen, elset=layer1c
4001, 1, 1, 1, 20, 6, 1, 40, 200, 20
*elgen, elset=layer2c
5001, 1, 1, 1, 20, 6, 1, 40, 200, 20
**
**===
** GENERATION OF REFERENCE NODES FOR THE RIGID SURFACES
**===

```
**
*node, nset=refnodes
10001, 0.5, 0.075, 0.
10002, 0.5, 0.075, 9.3700787
**
**==============================
** RUBBER COMPOUND PROPERTIES
**==============================
**
**LOCAL COORD. SYSTEM FOR SOLID ELEMENTS
*ORIENTATION,NAME=OR_SOLID,SYSTEM=USER
**
*SOLID SECTION,ELSET=layer1r      ,MATERIAL=mlayer1r,ORIENTATION=OR_SOLID
*MATERIAL,NAME=mlayer1r
*USER MATERIAL, CONSTANTS=11,TYPE=MECHANICAL
13227.44,29515.18,1.5686,13227.44,0.49,0.45,-1.75,1.43,1.,
319.4,2.013E-4
*DEPVAR
3
*USER OUTPUT VARIABLES
2
*USER DEFINED FIELD
*INITIAL CONDITIONS, TYPE=SOLUTION, USER
**
*SOLID SECTION,ELSET=layer2r      ,MATERIAL=mlayer2r,ORIENTATION=OR_SOLID
*MATERIAL,NAME=mlayer2r
*USER MATERIAL, CONSTANTS=11,TYPE=MECHANICAL
13227.44,29515.18,1.5686,13227.44,0.49,0.45,-1.75,1.43,1.,
319.4,2.013E-4
*DEPVAR
3
*USER OUTPUT VARIABLES
2
*USER DEFINED FIELD
*INITIAL CONDITIONS, TYPE=SOLUTION, USER
**
*SOLID SECTION,ELSET=removal      ,MATERIAL=mlayer3r,ORIENTATION=OR_SOLID
*MATERIAL,NAME=removal
*USER MATERIAL, CONSTANTS=11,TYPE=MECHANICAL
13227.44,29515.18,1.5686,13227.44,0.49,0.45,-1.75,1.43,1.,
319.4,2.013E-4
*DEPVAR
3
*USER OUTPUT VARIABLES
2
*USER DEFINED FIELD
*INITIAL CONDITIONS, TYPE=SOLUTION, USER
```

```
**
*SOLID SECTION,ELSET=layer3r      ,MATERIAL=mlayer2r,ORIENTATION=OR_SOLID
*MATERIAL,NAME=mlayer3r
*USER MATERIAL, CONSTANTS=11,TYPE=MECHANICAL
13227.44,29515.18,1.5686,13227.44,0.49,0.45,-1.75,1.43,1.,
319.4,2.013E-4
*DEPVAR
3
*USER OUTPUT VARIABLES
2
*USER DEFINED FIELD
*INITIAL CONDITIONS, TYPE=SOLUTION, USER
**
*SOLID SECTION,ELSET=layer4r      ,MATERIAL=mlayer3r,ORIENTATION=OR_SOLID
*MATERIAL,NAME=mlayer4r
*USER MATERIAL, CONSTANTS=11,TYPE=MECHANICAL
13227.44,29515.18,1.5686,13227.44,0.49,0.45,-1.75,1.43,1.,
319.4,2.013E-4
*DEPVAR
3
*USER OUTPUT VARIABLES
2
*USER DEFINED FIELD
*INITIAL CONDITIONS, TYPE=SOLUTION, USER
**
**==========================================
** LAYER PROPERTIES FOR MEMBRANE ELEMENTS
**==========================================
**
*ORIENTATION,NAME=OR_SHELL,SYSTEM=USER
**
**LAYER    1   EPI   14   CORD ANGLE    +18.00
** ADDITIONAL DENSITY DUE TO THE CORDS:
*membrane SECTION, ELSET=layer1c    ,MATERIAL=mlayer1c ,ORIENTATION=OR_SHELL
   .03080
*MATERIAL,NAME=mlayer1c
*elastic
790., 0.49
**
**LAYER    2   EPI   14   CORD ANGLE    -18.00
** ADDITIONAL DENSITY DUE TO THE CORDS:
*membrane SECTION, ELSET=layer2c    ,MATERIAL=mlayer2c ,ORIENTATION=OR_SHELL
   .03080
*MATERIAL,NAME=mlayer2c
*ELASTIC
790., 0.49
**
```

```
**=============================================
** REBARS DEFINITION FOR MEMBRANE ELEMENTS
**=============================================
**
** REBAR DEFINITION FOR THE LAYER #   1
**
*REBAR,ELEMENT=membrane,MATERIAL=CORD1,GEOMETRY=SKEW,NAME=REBAR1
**
** REFERENCE ELEMENT :  EPI :  14  GY ANGLE : +18.00
layer1c   ,  .000745,  .0463,  72.00
**
** REBAR DEFINITION FOR THE LAYER #   2
**
*REBAR,ELEMENT=membrane,MATERIAL=CORD2,GEOMETRY=SKEW,NAME=REBAR2
**
** REFERENCE ELEMENT :  EPI :  14  GY ANGLE : -18.00
layer2c   ,  .000745,  .0463,  -72.00
**
** BILINEAR CORD PROPERTIES USED FOR THE REBARS
**
** NOTE :  CORD COMPRESSION MODULUS =  1/10 OF TRACTION MODULUS
**
** MATERIAL CORD1 FOR THE REBAR CORD UM      OF LAYER #   1 :
*MATERIAL,NAME=cord1
*ELASTIC
 .22000E+08, 0.35, 0.0, 0.0    ,  0.0
**
** MATERIAL CORD2 FOR THE REBAR CORD UM      OF LAYER #   2 :
*MATERIAL,NAME=cord2
*ELASTIC
 .22000E+08, 0.35, 0.0, 0.0    ,  0.0
**
**  Definition of the rigid surfaces at the ends of the plies
**
*rigid surface, type=cylinder, name=rsend1, ref node=10001
0., 0.141732, 0., 1., 0.141732, 0.
0., 0., 0.,
start, 1., 0.
line, 0., 0.
**
** =========================
** RIGID SURFACE GENERATION
** =========================
**
*surface definition, name=surface1, trim=yes
ALLS1
*contact pair, interaction=surend1, adjust=0., tied
```

surface1, rsend1
**
*surface interaction, name=surend1
**
*rigid surface, type=cylinder, name=rsend2, ref node=10002
0., 0.141732, 7.28346, 1., 0.141732, 7.28346
0., 0., 7.28346
start, 0., 0.
line, 1., 0.
**
*surface definition, name=surface2, trim=yes
ALLS2
*contact pair, interaction=surend2, adjust=0., tied
surface2, rsend2
**
*surface interaction, name=surend2
**
*ELSET,ELSET=ALLSOLID
layer1r, layer2r, removal, layer3r, layer4r
**
*ELSET,ELSET=ALLLAYER
layer1c, layer2c
**
*ELSET,ELSET=ALLS1, GENERATE
1,100
*ELSET,ELSET=ALLS2, GENERATE
3901,4000
**
*RESTART,WRITE,OVERLAY
**
** DEFINITION OF ELEMENTS TO BE REMOVED
**
*ELSET,ELSET=LEFT, GENERATE
** First
1503, 2403, 100
** Second
1508, 2408, 100
** Third
1613, 2313, 100
** Fourth
1618, 2318, 100
** Fifth
1723, 2223, 100
** Sixth
1728, 2228, 100
** Seventh
1833, 2133, 100

** Eighth
1838, 2138, 100
** Ninth
1943, 2043, 100
** Tenth
1948, 2048, 100
*ELSET,ELSET=RIGHT, GENERATE
** First
1598, 2498, 100
** Second
1593, 2493, 100
** Third
1688, 2388, 100
**Fourth
1683, 2383, 100
** Fifth
1778, 2278, 100
** Sixth
1773, 2273, 100
** Seventh
1868, 2168, 100
** Eighth
1863, 2163, 100
** Ninth
1958, 2058, 100
** Tenth
1953, 2053, 100
*ELSET, ELSET=GO
LEFT
RIGHT
**
*User Subroutine
**
```
      SUBROUTINE UMAT(STRESS,STATEV,DDSDDE,SSE,SPD,SCD,RPL,DDSDDT,
     &        DRPLDE,DRPLDT,STRAN,DSTRAN,TIME,DTIME,TEMP,
     &        DTEMP,PREDEF,DPRED,CMNAME,NDI,NSHR,NTENS,NSTATV,
     &        PROPS,NPROPS,COORDS,DROT,PNEWDT,CELENT,DFGRD0,DFGRD1,
     &        NOEL,NPT,LAYER,KSPT,KSTEP,KINC)
C
C
      INCLUDE 'ABA_PARAM.INC'
C
      CHARACTER*8 CMNAME
C
C++++++++GLOBAL ARRAYS
C
      DIMENSION STRESS(NTENS),STATEV(NSTATV),DDSDDE(NTENS,NTENS),
```

```
     &   DDSDDT(NTENS),DRPLDE(NTENS),STRAN(NTENS),DSTRAN(NTENS),
     &   TIME(2),PREDEF(1),DPRED(1),PROPS(NPROPS),COORD(3),
     &   DROT(3,3),DFGRD0(3,3),DFGRD1(3,3)
C
C+++++++LOCAL ARRAYS
C
C-----------------------------------------------------------------------
C    BBAR   - DEVIATORIC RIGHT CUACHY-GREEN TENSOR           -
C    BBARP  - PRINCIPAL VALUES OF BBAR                       -
C    BBARN  - PRINCIPAL DIRECTION OF BBAR (AND EELAS)        -
C    DISTGR - DEVIATORIC DEFORMATION GRADIENT (DISTORSION TENSOR)   -
C                                                            -
C-----------------------------------------------------------------------
C
     DIMENSION EELAS(6),EELASP(3),BBAR(6),BBARP(3),BBARN(3,3),
     &       DISTGR(3,3),ARRAY(1)
C
C
     PARAMETER(ZERO=0.D0,ONE=1.D0,TWO=2.D0,THREE=3.D0,FOUR=4.D0)
     PARAMETER(TEN=10.D0,HALF=0.5D0,BIG=1.D8)
C
C
     C10=267.454D0
C
C----THIS VALUE IS FROM ABAQUS EXAMPLE MANUAL
C
     D1=2.013E-4
C
C
C======================================================================
C+++++JACOBIAN AND DISTORSION TENSOR
C
     DET=DFGRD1(1,1)*DFGRD1(2,2)*DFGRD1(3,3)
     &  -DFGRD1(1,2)*DFGRD1(2,1)*DFGRD1(3,3)
C
C
      IF(NSHR.EQ.3) THEN
       DET=DET+DFGRD1(1,2)*DFGRD1(2,3)*DFGRD1(3,1)
     &     +DFGRD1(1,3)*DFGRD1(3,2)*DFGRD1(2,1)
     &     -DFGRD1(1,3)*DFGRD1(3,1)*DFGRD1(2,2)
     &     -DFGRD1(2,3)*DFGRD1(3,2)*DFGRD1(1,1)
      ENDIF
C
C
     SCALE=DET**(-ONE/THREE)
C
     DO 10 K1=1,3
```

```fortran
        DO 5 K2=1,3
          DISTGR(K2,K1)=SCALE*DFGRD1(K2,K1)
 5      CONTINUE
 10   CONTINUE
C
C
C++++++CALCULATE LEFT CAUCHY-GREEN TENSOR
C
      BBAR(1)=DISTGR(1,1)**2+DISTGR(1,2)**2+DISTGR(1,3)**2
      BBAR(2)=DISTGR(2,1)**2+DISTGR(2,2)**2+DISTGR(2,3)**2
      BBAR(3)=DISTGR(3,3)**2+DISTGR(3,1)**2+DISTGR(3,2)**2
      BBAR(4)=DISTGR(1,1)*DISTGR(2,1)+DISTGR(1,2)*DISTGR(2,2)
     &      +DISTGR(1,3)*DISTGR(2,3)
C
C
      IF(NSHR.EQ.3) THEN
        BBAR(5)=DISTGR(1,1)*DISTGR(3,1)+DISTGR(1,2)*DISTGR(3,2)
     &        +DISTGR(1,3)*DISTGR(3,3)
        BBAR(6)=DISTGR(2,1)*DISTGR(3,1)+DISTGR(2,2)*DISTGR(3,2)
     &        +DISTGR(2,3)*DISTGR(3,3)
      ENDIF
C
C
C++++++++CALCULATE THE STRESS
C
      TRBBAR=(BBAR(1)+BBAR(2)+BBAR(3))/THREE
      EG=TWO*C10/DET
      EK=TWO/D1*(TWO*DET-ONE)
      DO 15 K1=1,NDI
        STRESS(K1)=EG*(BBAR(K1)-TRBBAR)+EK*(ONE-ONE/DET)
 15   CONTINUE
C
C
      DO 20 K1=NDI+1,NDI+NSHR
        STRESS(K1)=EG*BBAR(K1)
 20   CONTINUE
C
C++++++++STRAIN COMPUTATION
C
      DO 25 K1=1,NDI
        STRAN(K1)=STRAN(K1)+DSTRAN(K1)
 25   CONTINUE
C
C
      DO 30 K1=NDI+1,NDI+NSHR
        STRAN(K1)=STRAN(K1)+DSTRAN(K1)
 30   CONTINUE
```

```
C
C
      SIG1=STRESS(1)
      SIG2=STRESS(2)
      SIG3=STRESS(3)
      SIG4=STRESS(4)
      SIG5=STRESS(5)
      SIG6=STRESS(6)
C
      EPS1=STRAN(1)
      EPS2=STRAN(2)
      EPS3=STRAN(3)
      EPS4=STRAN(4)
      EPS5=STRAN(5)
      EPS6=STRAN(6)
C
C+++++++COMPUTATION OF THE MATRIX C
C
      EK1=(TWO/D1)*(DET**2)
      C11=EG*(BBAR(1)+BBAR(1))-EK1
      C22=EG*(BBAR(2)+BBAR(2))-EK1
      C33=EG*(BBAR(3)+BBAR(3))-EK1
      C12=EG*(BBAR(4)+BBAR(4))
      C13=EG*(BBAR(5)+BBAR(5))
      C23=EG*(BBAR(6)+BBAR(6))
      C44=EG*(BBAR(1)+BBAR(3))
      C55=EG*(BBAR(2)+BBAR(3))
      C66=EG*(BBAR(1)+BBAR(2))
C
C
C++++++COMPUTATION OF THE MATRIX S=1/C
C
      COEF0=C44*C55*C66
      COEF1=C44*C55
      COEF2=C44*C66
      COEF3=C55*C66
C
      DETER=COEF0*(C11*C22*C33-C11*C23*C23-C12*C12*C33)
      DETER=DETER+COEF0*(C12*C23*C13+C13*C12*C23-C13*C22*C13)
C
      EM11=COEF0*(C22*C33-C23*C23)
      EM22=COEF0*(C11*C33-C13*C13)
      EM33=COEF0*(C11*C22-C12*C12)
      EM12=COEF0*(C13*C23-C12*C33)
      EM13=COEF0*(C12*C23-C13*C22)
      EM44=COEF3*(C11*C22*C33-C11*C23*C23-C12*C12*C33)
      EM44=EM44+COEF3*(C12*C23*C13+C13*C12*C23-C13*C22*C13)
```

184

```
      EM55=COEF2*(C11*C22*C33-C11*C23*C23-C12*C12*C33)
      EM55=EM55+COEF2*(C12*C23*C13+C13*C12*C23-C13*C22*C13)
      EM66=COEF1*(C11*C22*C33-C11*C23*C23-C12*C12*C33)
      EM66=EM66+COEF1*(C12*C23*C13+C13*C12*C23-C13*C22*C13)
C
      S11=EM11/DETER
      S22=EM22/DETER
      S33=EM33/DETER
      S12=EM12/DETER
      S13=EM13/DETER
      S23=EM23/DETER
      S44=EM44/DETER
      S55=EM55/DETER
      S66=EM66/DETER
C
C
C+++++++CALCULATE THE STIFFNESS
C
C
      EG23=EG*TWO/THREE
C
      DDSDDE(1,1)=EG23*(BBAR(1)+TRBBAR)+EK
      DDSDDE(2,2)=EG23*(BBAR(2)+TRBBAR)+EK
      DDSDDE(3,3)=EG23*(BBAR(3)+TRBBAR)+EK
      DDSDDE(1,2)=-EG23*(BBAR(1)+BBAR(2)-TRBBAR)+EK
      DDSDDE(1,3)=-EG23*(BBAR(1)+BBAR(3)-TRBBAR)+EK
      DDSDDE(2,3)=-EG23*(BBAR(2)+BBAR(3)-TRBBAR)+EK
      DDSDDE(1,4)=EG23*BBAR(4)/TWO
      DDSDDE(2,4)=EG23*BBAR(4)/TWO
      DDSDDE(3,4)=-EG23*BBAR(4)
      DDSDDE(4,4)=EG*(BBAR(1)+BBAR(2))/TWO
      IF(NSHR.EQ.3) THEN
        DDSDDE(1,5)=EG23*BBAR(5)/TWO
        DDSDDE(2,5)=-EG23*BBAR(5)
        DDSDDE(3,5)=EG23*BBAR(5)/TWO
        DDSDDE(1,6)=-EG23*BBAR(5)
        DDSDDE(2,6)=EG23*BBAR(5)/TWO
        DDSDDE(3,6)=EG23*BBAR(5)/TWO
        DDSDDE(5,5)=EG*(BBAR(1)+BBAR(3))/TWO
        DDSDDE(6,6)=EG*(BBAR(2)+BBAR(3))/TWO
        DDSDDE(4,5)=EG*BBAR(6)/TWO
        DDSDDE(4,6)=EG*BBAR(5)/TWO
        DDSDDE(5,6)=EG*BBAR(4)/TWO
      ENDIF
C
C
      DO 35 K1=1,NTENS
```

```fortran
        DO 40 K2=1,K1-1
          DDSDDE(K1,K2)=DDSDDE(K2,K1)
 40     CONTINUE
 35   CONTINUE
C
      STATEV(1)=FA
      STATEV(2)=FR
      STATEV(3)=FLAG1
C
C
      RETURN
      END
C
*USER SUBROUTINE
      SUBROUTINE SDVINI(STATEV,COORDS,NSTATV,NCRDS,NOEL,NPT,
     &      LAYER,KSPT)
C===============================================================
C                                              -
C   USED TO INITIALIZE NON NULL SOLUTION-DEPENDENT STATE VARIABLES   -
C                                              -
C   STATEV(2) CORRESPONDS TO THE REMAINING STRENGTH AT T=0       -
C                                              -
C===============================================================
C
      INCLUDE 'ABA_PARAM.INC'
C
      DIMENSION STATEV(NSTATV),COORDS(NCRDS)
C
      PARAMETER(ZERO=0.D0,ONE=1.D0)
c
      STATEV(2)=ONE
C
      RETURN
      END
C
*USER SUBROUTINE
      SUBROUTINE USDFLD(FIELD,STATEV,PNEWDT,DIRECT,T,CELENT,TIME,
     &      DTIME,CMNAME,ORNAME,NFIELD,NSTATV,NOEL,NPT,LAYER,
     &      KSPT,KSTEP,KINC,NDI,NSHR)
C===============================================================
C        CAN USE AND UPDATE STATE VARIABLES
C===============================================================
C
      INCLUDE 'ABA_PARAM.INC'
C
C
      CHARACTER*8 CMNAME,ORNAME,FLGRAY(15)
```

```
C
      DIMENSION FIELD(NFIELD),STATEV(NSTATV),DIRECT(3,3),
     &      T(3,3),TIME(2)
C
      DIMENSION ARRAY(15),JARRAY(15)
C
      PARAMETER(ONE=1.D0)
c
      JERROR=0
C
C
      JERROR=JERROR+JRCD
C
      FIELD(1)=STATEV(1)
      FIELD(2)=STATEV(2)
      FIELD(3)=STATEV(3)
c
      IF(FIELD(2).LT.FIELD(1)) FIELD(3)=ONE
c
      STATEV(3)=FIELD(3)
C
      IF(JRCD.NE.0) THEN
       WRITE(6,*) 'REQUEST ERROR IN USDFLD FOR ELEMENT NUMBER ',
     &       NOEL,'INTEGRATION POINT NUMBER ', NPT
      ENDIF
      RETURN
      END

**
** STEP 1 DEFINITION
**_____
**
*STEP,NLGEOM,INC=100
STEP 1
*STATIC
  .0125,  1.,   0.000001
**STEP,NLGEOM,INC=100
**STEP 1
*controls, parameters=constraints
0.01
*controls, parameters=field
1.0, 1.0, 0.2, 0.2
**
*MODEL CHANGE, REMOVE
GO
**
*BOUNDARY,OP=MOD
```

```
10001  , 1, 6,  0.0
10002  , 1, 2,  0.0
10002  , 4, 6,  0.0
**20002  , 3, 3,  1.1
*CLOAD
10002  , 3, 50
**382.16
**
*FILE FORMAT,ASCII
**
**
*END STEP
**
** STEP 2 Run
**_____
**
**
*STEP,NLGEOM,INC=100
STEP 1
*STATIC
  .0125,   1.,   0.000001
**STEP,NLGEOM,INC=100
**STEP 1
**STATIC
**   .05,   1.00,   .000010
*controls, parameters=constraints
0.01
*controls, parameters=field
1.0, 1.0, 0.2, 0.2
**
**
*BOUNDARY,OP=MOD
10001  , 1, 6,  0.0
10002  , 1, 2,  0.0
10002  , 4, 6,  0.0
**20002  , 3, 3,  1.1
*CLOAD
10002  , 3, 400
**382.16
**
**
*OUTPUT, FIELD, FREQ=1, OP=ADD
*ELEMENT OUTPUT, ELSET=REMOVAL
UVARM
ENER
*OUTPUT, FIELD, FREQ=1, VARIABLE=PRESELECT, OP=ADD
**
```

*END STEP

14.   VITA

Joseph Thomas South

Joseph Thomas South, born to Larry and Jean South was raised in Pasadena, Maryland. In 1992 he graduated from Chesapeake Senior High School and continued his formal education at Loyola College in Maryland. While an undergraduate at Loyola he balanced his time between participated on the Division I Men's Cross Country Team and a Liberal Arts Engineering education. Joseph was active in the community and donated his Junior and Senior year Spring Breaks so that he could volunteer his time in outreach programs.   Following his graduation from Loyola in 1996 he began his graduate studies at the University of Delaware in the Materials Science and Engineering Program. At Delaware he performed research on semiconducting quatanary materials systems for thermophotovoltaic applications.   For his research he was awarded the Bill N Baron Fellowship for outstanding photovoltaic research. In 1998 he completed his Masters Degree and transitioned to composites research at Virginia Tech. While at Virginia Tech, Joseph, performed research related to the High Speed Civil Transport, truck tires and polymer fuel cells. His doctoral research was aimed at quantifying the effects of thermal degradation on natural rubber compounds and applying those effects to the durability and life prediction of cord-rubber composites.